Fall 2013

Theoretical analysis of the reaction of peroxymethyl radical with atomic hydrogen and of dibenzofuran with atomic chlorine

Mikhail Zhukovskiy
University of New Hampshire, Durham

THEORETICAL ANALYSIS OF THE REACTION OF PEROXYMETHYL RADICAL WITH ATOMIC HYDROGEN AND OF DIBENZOFURAN WITH ATOMIC CHLORINE

BY

MIKHAIL ZHUKOVSKIY
B.A. Chemistry, Cornell University, 2005

THESIS

Submitted to the University of New Hampshire

in Partial Fulfillment of

the Requirements for the Degree of

Master of Science

in

Chemistry

September, 2013

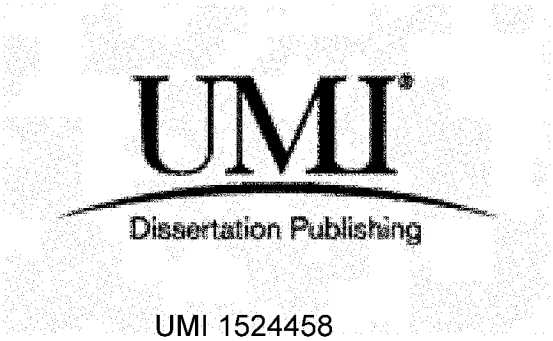

ProQuest LLC
789 East Eisenhower Parkway
P.O. Box 1346
Ann Arbor, MI 48106-1346

This thesis has been examined and approved.

Dr. Howard R. Mayne,
Professor of Chemistry

Dr. Arthur Greenberg,
Professor of Chemistry

Dr. Sterling Tomellini,
Professor of Chemistry

7/2/2013
Date

DEDICATION

To Khadija

To Mom, Dad, and my older sister Jenny

ACKNOWLEDGEMENTS

I would like to express sincere gratitude to the members of my committee. My thesis advisor, Dr. Howard Mayne, taught me everything that I know about chemical kinetics and reaction dynamics. He was an extremely knowledgeable and patient mentor. Dr. Arthur Greenberg and Dr. Sterling Tomellini made valuable critiques during the preparation of this thesis.

I would also like to thank Dr. Donald Truhlar for providing the POLYRATE program and Drs. Jingjing Zheng and Yao-Yuan Chuang for helpful suggestions.

During the preparation of this work, I could always count on the professionalism and kindness of Chemistry Department staff, especially Cindi Rohwer, Peg Torch, and Bob Constantine.

Financial support for this work was provided through the Chemistry Department's teaching assistantship and through the Graduate School's Summer TA fellowship.

TABLE OF CONTENTS

LIST OF FIGURES

LIST OF TABLES

ABSTRACT

by

Mikhail Zhukovskiy

University of New Hampshire, May 2013

Experimental determination of rate constants for gas phase radical reactions is challenging. When rate constants necessary for modeling complex processes in atmospheric and combustion science are unknown, theoretical predictions are useful. We used Variational Transition State Theory with Multidimensional Tunneling (VTST/MT) with Density Functional Theory (DFT) to calculate the rate constant and isotope effects for reaction between the peroxymethyl radical and the hydrogen atom.

Polychlorinated dibenzofurans (PCDFs) are a group of extremely toxic compounds formed during waste incineration. Currently, their chemical degradation in the atmosphere is poorly understood. While some experimental and theoretical results regarding the reaction of PCDFs with the hydroxyl radical are available, to our knowledge, no group has studied their reaction with another important atmospheric oxidant, the chlorine atom (Cl). As a first step in this direction, we have characterized the potential energy surface for reaction between the parent compound of PCDFs, dibenzofuran, and Cl using DFT.

LIST OF COMMONLY USED ABBREVIATIONS

AO	Atomic Orbital
CVT	Canonical Variational Theory
CVT/MT	Canonical Variational Theory with Multidimensional Tunneling
CVT/SCT	Canonical Variational Theory with Small Curvature Tunneling
CVT/ZCT	Canonical Variational Theory with Zero Curvature Tunneling
DBF	Dibenzofuran
DFT	Density Functional Theory
GTS	Generalized Transition State
HO	Harmonic Oscillator
HR	Hindered Rotor
IVTST-M	Interpolated Variational Transition State Theory with Mapping
KIE	Kinetic Isotope Effect
LCT	Large Curvature Tunneling
MEP	Minimum Energy Path
MO	Molecular Orbital
μOMT	Microcanonically Optimized Multidimensional Tunneling
MT	Multidimensional Tunneling
PCDD	Polychlorinated Dibenzodioxin
PCDF	Polychlorinated Dibenzofuran
PES	Potential Energy Surface
SCT	Small Curvature Tunneling
SRPG	Segmented Reference Pitzer-Gwinn
TS	Transition State
TST	Transition State Theory
VTST	Variational Transition State Theory
VTST/MT	Variational Transition State Theory with Multidimensional Tunneling
VOC	Volatile Organic Compound
WFT	Wave Function Theory
ZCT	Zero Curvature Tunneling
ZPE	Zero Point Energy

CHAPTER 1

DETERMINATION OF THE RATE CONSTANT AND ISOTOPE EFFECTS FOR THE $CH_3O_2 + H \rightarrow CH_2O_2 + H_2$ REACTION USING VARIATIONAL TRANSITION STATE THEORY WITH MULTIDIMENSIONAL TUNNELING IN COMBINATION WITH DENSITY FUNCTIONAL THEORY

1.1 Motivation

Volatile Organic Compounds (VOCs) are emitted into the troposphere from a variety of anthropogenic and biogenic sources. The atmosphere is an oxidizing environment, and VOC oxidation leads to increased production of tropospheric ozone (O_3) and aerosols.[1-7] This is a concern, because both have adverse effects on human health, [8-9] global climate,[10-11] and agricultural productivity.[12]

In the last two decades, numerous experimental and theoretical studies have focused on the gas phase chemistry of a class of reactive products of VOC oxidation called carbonyl oxides, or Criegee intermediates, ($R_1R_2CO_2$).[13-24] Criegee intermediates play a role in controlling the oxidative capacity of the troposphere, because they decompose to produce the hydroxyl radical (OH).[14-19, 23] Oxidation by OH is the main removal process for many atmospheric pollutants.[1-6] Although OH is usually thought of as a product of ozone photolysis,[2-6] reactions of Criegee intermediates have been shown to be an important source of OH, especially during nighttime[25-26] and winter[27] and in

urban environments.[25-29] Criegee intermediates are also known to play a role in organic aerosol chemistry[7] and combustion[30].

The most well studied atmospheric source of Criegee intermediates is the ozonolysis reaction of alkenes.[1-6, 13-18]

$$R_1R_2C=CR_3R_4\,(g)+O_3(g)\rightarrow R_1R_2CO_2\,(g)+R_3R_4C=O\,(g) \qquad (1)$$

In 1949, Criegee proposed these intermediates for reaction (1) in solution,[31] and in the 1970s it was demonstrated that the gas phase reaction proceeds by the same mechanism.[32] However, because of their short lifetime, direct observation of Criegee intermediates has been a challenge. It was finally accomplished for the simplest example (formaldehyde oxide, CH_2O_2) in 2008, using a synchrotron light source.[33-35] (In 2012, it was repeated using a more conventional laser light source in combination with a pulsed beam technique.[24]) This, for the first time, made possible direct measurement of Criegee intermediate kinetics, which turned out to be much faster than previously estimated for reaction towards NO_2 and SO_2.[34] Possible channels for these reactions include

$$R_1R_2CO_2\,(g)+SO_2(g)\rightarrow R_1R_2CO(g)+SO_3(g) \qquad (2)$$

$$R_1R_2CO_2(g)+NO_2(g)\rightarrow R_1R_2CO\,(g)+NO_3(g) \qquad (3)$$

SO_3 reacts with water to make sulfuric acid, a major component of inorganic aerosols.[3-6] The recently determined rate coefficient for (2), recent indirect determinations,[20] and field studies[36-37] suggest that (2) is an important source of sulfuric acid. Reaction (3) has implications for ozone production and the oxidative capacity of the troposphere.

In contrast to the case of the alkene source, the possibility of an alkane source has not been sufficiently investigated. Alkane oxidation proceeds predominantly through

reaction with OH, followed by addition of O_2 to yield a peroxy radical.[1-6] From here on, methane (CH_4) is used as the prototypical alkane.

$$CH_4\,(g) + OH\,(g) \rightarrow CH_3(g) + H_2O\,(g) \quad (4)$$

$$CH_3\,(g) + O_2\,(g) \rightarrow CH_3O_2\,(g) \quad (5)$$

Peroxy radicals (RO_2) are the starting point of numerous chemistries leading to the formation of ozone, organic nitrates, organic acids, and other secondary pollutants.[38-43]

Abstraction of another hydrogen from CH_3O_2 gives a Criegee intermediate,

$$CH_3O_2\,(g) + X\,(g) \rightarrow CH_2O_2\,(g) + HX\,(g) \quad (6)$$

where X is one of a number of reactive radicals. In the troposphere, the most important reactions are expected to be

$$CH_3O_2\,(g) + OH\,(g) \rightarrow CH_2O_2\,(g) + H_2O\,(g) \quad (6a)$$

$$CH_3O_2\,(g) + Cl\,(g) \rightarrow CH_2O_2\,(g) + HCl\,(g) \quad (6b)$$

As stated previously, OH is the main tropospheric oxidant, yet, to our knowledge, there have been no experimental or theoretical studies of reaction (6a). Sensitivity analysis of an atmospheric model found a material difference between calculations employing different values for the rate constant of this reaction.[44]

The role of atomic chlorine is less well established.[45] Because Cl is a much stronger oxidant than OH[46-47]and photolabile Cl precursors are known products of reactions on sea-salt aerosols,[48-49] it was proposed that Cl is an oxidant in the marine troposphere.[50] This conjecture was lent credence by high Cl concentrations found at coastal[51-52] and inland[53] measurement sites.

Experimental rate coefficients for (6b) vary by a factor of 10, and no temperature dependence has been established.[54-56] There have also been several theoretical studies.[54, 57-59]

Other important variations of reaction (6) include

$$CH_3O_{2\,(g)} + H_{(g)} \rightarrow CH_2O_{2\,(g)} + H_{2\,(g)} \quad (6c)$$

$$CH_3O_{2\,(g)} + F_{(g)} \rightarrow CH_2O_{2\,(g)} + HF_{(g)} \quad (6d)$$

$$CH_3O_{2\,(g)} + Br_{(g)} \rightarrow CH_2O_{2\,(g)} + HBr_{(g)} \quad (6e)$$

Reaction (6c) is the prototype reaction and may be important in combustion systems, where there are significant H atom concentrations.[60] To our knowledge, there are no theoretical or experimental studies of (6c). Rate constants for two other pathways of this reaction, leading to different sets of products, have been reported. One is[61]

$$CH_3O_2\,(g) + H\,(g) \rightarrow CH_3O\,(g) + OH\,(g) \quad (7)$$

The other is[62]

$$CH_3O_2\,(g) + H\,(g) \rightarrow CH_3\,(g) + O_2\,(g) \quad (8)$$

Reaction (6d) is an interference in experiments where F atoms are used to generate peroxy radicals.

$$CH_4\,(g) + F\,(g) \rightarrow CH_3\,(g) + HF\,(g) \quad (9)$$

$$CH_3(g) + O_2\,(g) \rightarrow CH_3O_2\,(g) \quad (10)$$

There is no experimental rate coefficient for (6d), so workers have been forced to estimate it.[63]

Reaction (6e) could be important in ozone depletion in the stratosphere and Arctic troposphere.[64] Experimental studies have tended to discount this pathway[65-66], but more recent theoretical work suggests that the reaction is feasible.[64, 67]

The generalized reaction (6) sits at the intersection of important reaction cycles, and clearly, more information about its kinetic parameters is necessary. Unfortunately, this is a common problem with radical reactions, because they are difficult to study experimentally.[4] In this situation, a theoretical approach is called for. Below, we use theory to calculate the rate constant for one of the channels of reaction (6c).

1.2 The Reaction Rate Constant

1.2.1 The Reaction Rate Constant and the Arrhenius Model

The rate constant for a bimolecular chemical reaction

$$A + B \rightarrow \text{Products} \tag{11}$$

is defined through the differential rate law,

$$-\frac{d[A][B]}{dt} = k(T)[A][B] \tag{12}$$

where T is the temperature and the dimensions of $k(T)$ are concentration^{-1} time^{-1}.

The temperature dependence of the rate constant frequently follows the Arrhenius model over small temperature ranges. This model has the temperature dependence:

$$k_M(T) = A\exp\left[-\frac{E_M}{RT}\right] \tag{13}$$

where M stands for "model", $k_M(T)$ is the Arrhenius rate constant, R is the universal gas constant, E_M is an energy barrier, and A is referred to as the pre-exponential factor.

The quantity E_a, given by

$$E_a = -R\frac{\partial \ln k(T)}{\partial(1/T)} \tag{14}$$

is referred to as the activation energy. It is roughly related to the energy barrier that the reactants must overcome to be converted to products. In the case of the Arrhenius model, $E_a = E_M$.

When relation (13) is obeyed, the plot of the natural logarithm of the rate constant, ln($k(T)$), against the inverse of the temperature, $1/T$, is a straight line with slope $-E_a / R$. This is referred to as an Arrhenius plot.

1.2.2 Different Ways of Obtaining Rate Constants

While it is preferable to have an experimental value for the rate constant, these experiments are frequently difficult, time-consuming, and expensive. This is especially true for radical-radical reactions, such as (6c).

When a desired rate constant has not been determined experimentally (as is the case for reaction (6c)), one may try to extrapolate it from existing data (see the work of Atkinson and co-workers for an example[68]). The other option, the one we have chosen, is to calculate the rate constant using theory.

The various theoretical approaches to calculating rate constants have been reviewed.[18, 69] The most accurate way of calculating rate constants is a fully quantum treatment, but this is prohibitively time intensive for a system of 7 atoms. A less time-consuming alternative is Variational Transition State Theory with Multidimensional Tunneling (VTST/MT)[70-71]. VTST/MT results have been validated against fully quantum results for several benchmark reactions,[71] including

$$CH_{4\,(g)} + H_{(g)} \rightarrow CH_{3\,(g)} + H_2\,(g) \qquad (15)$$

For reaction (15), rate constants calculated using the two methods coincide to within 15%.[72]

We chose to use VTST in combination with Density Functional Theory (DFT)[73] to calculate rate constants in this work. All rate constants were calculated using the POLYRATE program.[74-76]

1.3 The Potential Energy Surface (PES)

To calculate a rate constant theoretically, one usually starts by invoking the Born-Oppenheimer approximation, which states that the electron cloud reacts instantaneously to a change in the position of the nuclei. It is justified by noting that electrons are 1800 times lighter than nucleons and move much faster than the nuclei. It allows one to define a potential energy, $V(\mathbf{R})$, for every arrangement **R** of nuclei in space. Here, **R** is a vector containing the x, y, and z coordinates of every nucleus, 3N in total for a system of N atoms. $V(\mathbf{R})$ is thus a potential energy surface (PES) in 3N-6 dimensional space. (The -6 arises, because the potential energy is not affected by center of mass translations or rotations of the coordinate system). It is computed by summing the energy of nuclear repulsion, given by Coloumb's law, and the electronic energy, which is given by an electronic structure calculation.

For rate constant calculations, we must frequently calculate the gradient, ∇V, and the matrix of second derivatives $\{\partial V / \partial R_i \, \partial R_j\}$, known as the Hessian. Particularly important points on the PES are the stationary points, where ∇V vanishes. These are further characterized by the eigenvalues of the Hessian. Stationary points for which all Hessian eigenvalues are positive are local minima on the PES and correspond to the equilibrium geometries of the reactants and products. A stationary point with one negative Hessian eigenvalue is a saddle point (a minimum in all directions, except one). The eigenvectors corresponding to the Hessian eigenvalues are referred to as the normal mode coordinates of the system.

Small amplitude motions in the vicinity of stationary points can be approximated as uncoùpled motions along the normal mode coordinates. Motions along the normal

modes with positive Hessian eigenvalues (the bound modes) are usually approximated as harmonic vibrations, whose frequencies depend on the square root of the Hessian eigenvalues, the atomic masses, and the normal mode components. It is important to note that the quantum mechanical harmonic oscillator in the ground state has non-zero energy, which is referred to as the zero-point energy (ZPE). At the saddle point, the normal mode with the negative Hessian eigenvalue is the reaction coordinate.

The PES can be an analytic function of **R**, parameterized to reproduce some experimental quantity or a grid of points on the PES computed using an electronic structure method. We use a different approach, however, called direct dynamics, in which the energies, gradients, and Hessians are computed by an electronic structure calculation "on the fly", as we need them. Direct dynamics is particularly suited to VTST/MT calculations, because these calculations require only limited PES information.[70] Fully quantum treatments, on the other hand, require the global PES.

For the direct dynamics, we used the GAUSSRATE[77-78] program to interface POLYRATE with the electronic structure code (GAUSSIAN).

1.4 Electronic Structure Theory

1.4.1 Density Functional Theory (DFT)

The choice of electronic structure method involves balancing considerations of accuracy and efficiency. These methods are generally separated into wave function theory (WFT) and density functional theory (DFT).[73] The more advanced WFT methods are more accurate than DFT, but they are usually too computationally expensive for dynamics. For a level of accuracy attainable by both, DFT is more efficient. We chose DFT for this work.

In DFT, the electronic energy is given by a functional of the 3-dimensional electron density. A user of DFT must make two choices: the functional and a set of basis functions to represent the density. Together, these two specify a "model chemistry", or, synonymously, a "level of theory". A tremendous advance in DFT methodology was the development of hybrid functionals, which include a Hartree-Fock exchange component.[73] Hartree-Fock exchange is a WFT construct,[73] and thus, these functionals combine some of the concepts of WFT and DFT. Historically, the B3LYP functional[79-80] has been one of the most popular hybrid functionals. While it has proven extremely reliable over two decades,[81] B3LYP does have drawbacks, the most relevant for this work being that it underestimates reaction barriers and gives qualitatively incorrect results for non-covalent interactions.[82-88] A general discussion of some of the shortcomings of modern DFT is given in a recent review.[89]

Many alternative functionals are available.[73, 90] In dynamics studies, the usual strategy is to choose, for every reaction, the DFT model chemistry that best matches benchmark calculations performed using an advanced wavefunction method. All electronic structure calculations in this work were performed using the GAUSSIAN software package.[91-92]

1.4.2 Additional considerations for DFT

The DFT energy is not available in closed form. Instead, it is numerically integrated over volume using a quadrature grid. Dependence of calculation results, and especially vibrational frequencies, on grid size has been demonstrated.[93] The GAUSSIAN "ultrafine" grid was used for all calculations, unless otherwise stated.

To improve accuracy, it is standard practice to scale DFT vibrational frequencies by a factor specific to a model chemistry. We used published scaling factors.[94-95] When no scaling factor was available for a model chemistry, we used the scaling factor for the most similar model chemistry with a published value. In the case of the ωB97X-D functional, we found no scaling factors that we could use with our chosen basis sets.

For radicals, the unrestricted DFT formalism was used.[73] Species with open shell singlet character, such as the Criegee intermediate and the transition states for reaction (6), cannot be adequately represented in standard DFT due to the multi-reference character of their wavefunctions.[73] For these species, the unrestricted formalism was used with a broken symmetry initial guess wavefunction (GAUSSIAN "guess=mix" keyword). This accounts for some of the multi-reference character, but at the cost of spin contamination.[96] The reader is referred to reference (73) for further details on electronic structure calculations.

1.4.3 Basis Sets

In electronic structure theory, a basis set is a set of mathematical functions which are combined in a linear fashion to form one-electron molecular orbitals (MOs). The goal of an electronic structure calculation is to determine the coefficients with which these basis functions enter into the MOs. The MOs are combined according to specific rules to give the many-electron wavefunction. The square of the wavefunction gives the electron density.[73] In this section, we give a brief description of the basis sets used in this work. The discussion here has been adapted from several sources, to which the interested reader is directed.[73, 97-98]

We used the basis sets developed by Pople *et al.*[73, 97-99] The basic structure of the Pople basis sets used in this work is laid out below. The notation describing these basis sets is demonstrated on the example of two basis sets we used: 6-31+G(d,p) and 6-311+(2df,2p). Note that, since the 6-311+G(2df,2p) basis set is frequently referred to as MG3S, we also call it by that name in the rest of this work. MG3S has been shown to give good results in combination with DFT.[100]

A Pople basis function resembles an atomic orbital (AO) centered on one of the nuclei in the molecule. Basis functions have the form

$$\varphi = g_p(r) \times f_{q,i}(\theta,\phi) \times (a_1 e^{-\zeta_1 r^2} + a_2 e^{-\zeta_2 r^2} + \ldots + a_n e^{-\zeta_n r^2}) \qquad (16)$$

where (r, θ, ϕ) are spherical polar coordinates centered on the nucleus. $g_p(r)$ is a polynomial in r that determines the nodal structure of the basis function: $g_1(r)$ has no nodes, $g_2(r)$ has 1 node, and so on. The coefficients a_i and exponents ζ_i were determined by the basis sets' authors using calculations on single atoms.

$f_{q,i}(\theta,\phi)$ is the angular part of the basis function, where q and i are labels. Basis functions with $q = s, p, d,$ and f have the shape of s-type, p-type, d-type, and f-type AOs, respectively. Since p-type basis functions come in groups of three, d-type basis functions come in groups of 5, and f-type basis functions come in groups of 7, the label i denotes a specific member of a group.

The nature of a basis function is given by the notation pq_i. Thus, a basis function with $p = 2$, $q = p$, and $i = x$ is referred to as a $2p_x$ basis function.

A Pople basis set contains basis functions corresponding to all AOs in fully or partially occupied electron shells of the atoms constituting the molecule. In both the 6-31+G(d,p) and 6-311+(2df,2p) basis sets, inner AOs (carbon *1s* and oxygen *1s*) are

represented by one basis function with n=6 (hence the 6 in the basis set names). These basis functions are likely to appear with large coefficients in low energy MOs, which are closely centered on a specific nucleus and resemble an inner AO of that atom.

To give the basis set enough flexibility to represent higher energy MOs, which have significant amplitude both close and far from the nuclei, outer (valence) AOs (carbon *2s*, $2p_x$, $2p_y$, $2p_z$; oxygen *2s*, $2p_x$, $2p_y$, $2p_z$; hydrogen *1s*) are represented by multiple basis functions.

In 6-31+G(d,p), the valence AOs are represented by one basis function with n = 3 and one basis function with n = 1 (hence, the 3 and 1 in the basis set name). Since there are two basis functions corresponding to valence AOs, 6-31+G(d,p), is referred to as a double-ζ (double-zeta) quality basis set.

In the 6-311+G(2df,2p) basis set, valence AOs are represented by one basis function with n = 3 and two basis functions with n = 1 (hence the 3, 1, and 1 in the basis set name). Since there are three basis functions corresponding to valence AOs, 6-311++G(2df,2p) is referred to as a triple-ζ (triple-zeta) quality basis set.

By itself, the use of multiple basis functions for valence AOs does not provide enough flexibility to represent MO amplitude between the nuclei. To resolve this issue, polarization basis functions are used. Polarization basis functions (polarization functions) are additional basis functions with n = 1 whose $f_{q,i}(\theta,\phi)$ correspond to higher quantum numbers of angular momentum than the valence AOs. The number and types of polarization functions are encoded in the basis set name by the letters and numbers in parentheses, with those coming after the comma corresponding to H atoms and those coming before the comma corresponding to all other atoms.

The 6-31+G(d,p) basis set contains the following polarization functions :

1) one group of *d*-type polarization functions on C and O

2) one group of *p*-type polarization functions on H

The 6-311+G(2df, 2p) basis set contains the following polarization functions:

1) two groups of *d*-type polarization functions on C and O

2) one group of *f*-type polarization functions on C and O

3) two groups of *p*-type polarization functions on H

For MOs arising due to weak bonding (such as a van der Waals interaction), additional $n = 1$ basis functions with small exponents (ζ) are included in the basis set. These are called diffuse functions. The presence of diffuse functions on non-hydrogen atoms is denoted by one plus sign in the basis set name. The presence of diffuse functions on all atoms is denoted by two plus signs. The 6-31+G(d,p) and 6-311+G(2df,2p) basis sets both contain one *s*-type diffuse function and one group of *p*-type diffuse functions on non-H atoms. The 6-31++G(d,p) and 6-311 ++G(2df,2p) basis sets have an additional *s*-type diffuse function on the hydrogens. Note that 6-311++G(2df,2p) is referred to as MG3 in the rest of this work.

In addition to Pople basis sets, we used the maug-cc-pVTZ basis set of Truhlar and co-workers,[101] based on the aug-cc-pVTZ basis set of Dunning and co-workers[102], to calculate the CCSD(T) single point energies (see section 1.5.2). This is a triple-ζ basis set that contains both diffuse and polarization functions. The coefficients a_i and exponents ζ of Dunning type basis sets have been determined using more accurate calculations than those used in developing the Pople basis sets, and these basis sets are used when high accuracy is required.[73] The difference between aug-cc-pVTZ and maug-

cc-pVTZ is that the latter contains fewer diffuse functions. Calculations with it are more efficient, but accuracy is not sacrificed.[101]

1.5 Characterization of the Singlet Potential Energy Surface for Reaction (6c)

1.5.1 General Features of the PES

Recall reaction (6c)

$$CH_3O_2\ (g) + H\ (g) \rightarrow CH_2O_2\ (g) + H_2\ (g) \qquad (6c)$$

This reaction can occur on both the singlet and triplet PESs. Since the triplet PES has been studied previously,[62] we focused on the singlet PES in this work.

We explored the singlet PES using the B3LYP[79-80], M05, M05-2X[103], M06, M06-2X[104], M06-L[105], ωB97X-D[106], MPW1K[107], BMK[108], and BB1K[109] density functionals. We found that, on the B3LYP, M06-L, ωB97X-D, MPW1K, and BB1K potential energy surfaces, the reaction can proceed through two channels: a one step direct abstraction mechanism and a two step addition-elimination mechanism (see Figure 1-1). The addition-elimination pathway consists of a barrierless addition step and an elimination step, which has a saddle point that is lower in energy than the reactants.

$$CH_3O_2\ (g) + H\ (g) \rightarrow CH_3OOH\ (g) \rightarrow CH_2O_2\ (g) + H_2\ (g) \qquad (6c')$$

We were not able to locate a direct abstraction saddle point with the M05, M05-2X, M06, M06-2X, and BMK functionals.

Sufficient evidence exists for the addition-elimination channel of generalized reaction (6). Computational studies have reported a two-step mechanism analogous to (6c') for reactions (6b)[54, 57-59] and (6e)[64].

$$CH_3O_2\ (g) + Cl\ (g) \rightarrow CH_3OOCl\ (g) \rightarrow CH_2O_2\ (g) + HCl\ (g) \qquad (6b')$$

$$CH_3O_2\ (g) + Br\ (g) \rightarrow CH_3OOBr\ (g) \rightarrow CH_2O_2\ (g) + HBr\ (g) \qquad (6e')$$

Using B3LYP/6-311++G(3df,3pd), we also found a two-step mechanism for (6d)[110]

$$CH_3O_2\ (g) + F\ (g) \rightarrow CH_3OOF\ (g) \rightarrow CH_2O_2\ (g) + HF\ (g) \qquad (6d')$$

In comparison, the direct abstraction mechanism had been neglected, until workers at the University of New Hampshire found both one-step and two-step pathways for (6b) using both DFT (B3LYP) and WFT (MP4SDTQ and MP2) methods.[59] In addition, we have found a direct abstraction pathway for (6e) using B3LYP/6-31+G(d,p).[110]

There have been two computational studies of a reaction very similar to (6c).

$$CH_3O(g) + H(g) \rightarrow CH_2O(g) + H_2(g) \qquad (17)$$

Xu et al. found both a direct abstraction and an addition-elimination pathway at the CCSD(T)/6-311G(3df,2p)//CCSD/6-311G(3df,2p) level of theory.[111] Li et al. characterized the direct abstraction channel using QCISD(T)/aug-cc-pVTZ// QCISD(T)/cc-pVTZ.[112]

In light of the above, we judged the existence of both a direct abstraction channel and an addition-elimination channel on the singlet PES of reaction (6c) to be established.

1.5.2 Accurate Calculation of Stationary Point Properties

The geometries of the reactants, products, and saddle points for both channels on the singlet PES of reaction (6c) were optimized at the B3LYP/MG3S level of theory (see section 1.4). The nature of the stationary points was confirmed by calculating the vibrational frequencies, which are given in Table 1-1.

We calculated single point energies at these geometries using coupled cluster theory with single and double excitations and a quasi-perturbative treatment of connected triple excitations (CCSD(T))[113] with the maug-cc-pVTZ basis set[101] (see

section 1.4.3). The CCSDT(T) energies were adjusted with the vibrational zero point energies (ZPE), calculated using B3LYP/MG3S. The ZPE adjusted CCSD(T) energies of the stationary points for both channels are given in Figure 1-1 relative to the reactants.

In the rest of this work, we concern ourselves with calculating the rate constant for the direct abstraction using the VTST/MT[70] method, leaving the addition-elimination pathway for future study. A direct abstraction reaction comparable to (6c) been treated using VTST/MT.[114-115]

$$CH_3OH(g) + H(g) \rightarrow CH_2OH(g) + H_2(g) \qquad (18)$$

Table 1-1. B3LYP/MG3S vibrational frequencies (in cm^{-1}) of the stationary points on the singlet PES of reaction (6c). TS 1 is the direct abstraction saddle point. TS 2 is the addition-elimination saddle point. See Figure 1-1 below for the species' geometry.

Mode	CH_3O_2	TS 1	TS 2	CH_3OOH	CH_2O_2	H_2
1	132	997*i*	1070*i*	183	530	4423
2	492	117	543	249	675	
3	915	309	671	448	925	
4	1127	446	783	881	951	
5	1157	537	879	1035	1245	
6	1221	990	962	1171	1404	
7	1446	1138	1104	1205	1545	
8	1475	1162	1177	1376	3122	
9	1486	1222	1213	1453	3272	
10	3054	1364	1353	1465		
11	3142	1380	1386	1512		
12	3156	1451	1518	3013		
13		1663	2512	3078		
14		3089	3121	3112		
15		3179	3249	3775		

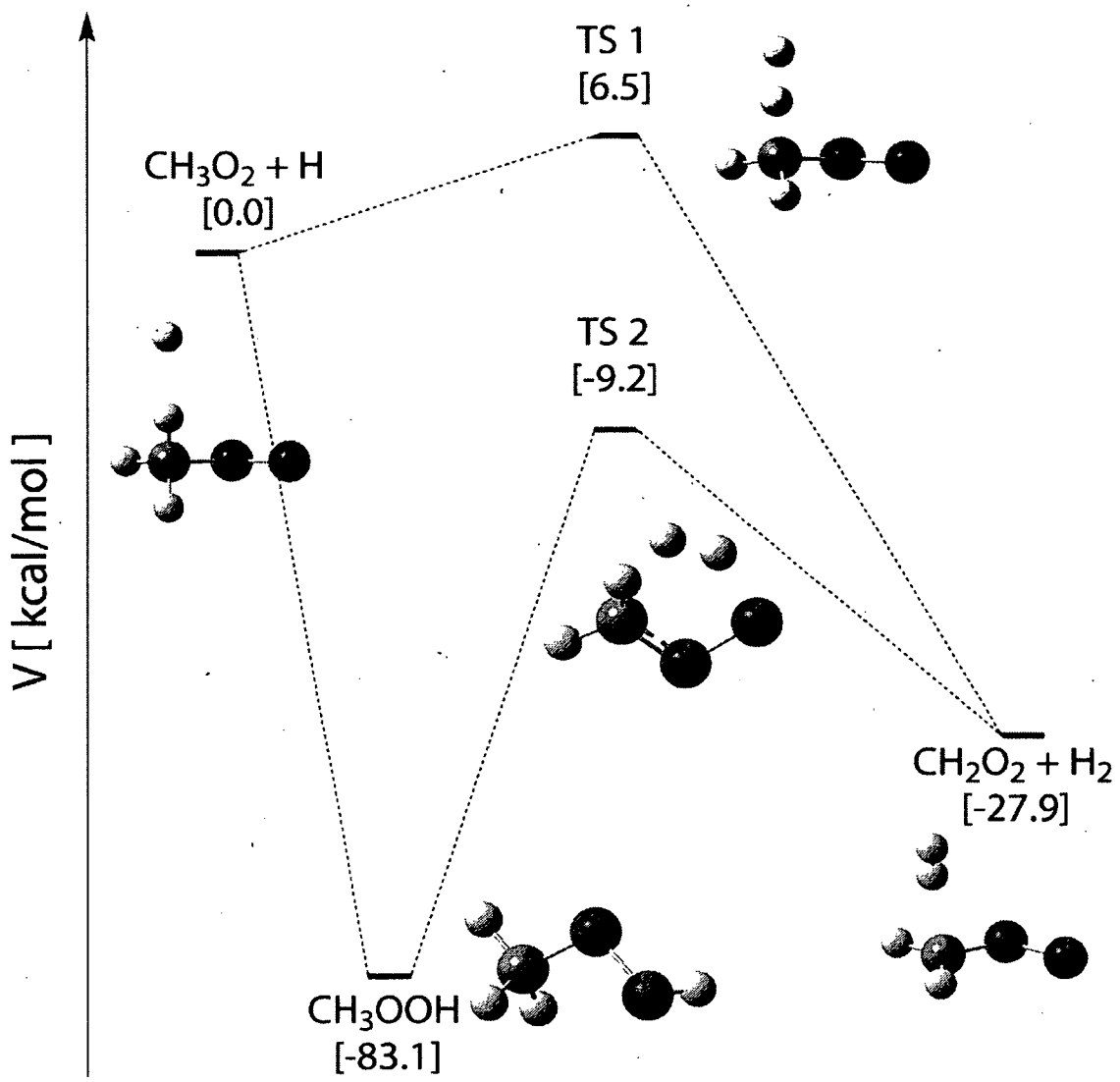

Figure 1-1. Energies of the stationary points on the PES of reaction $CH_3O_2 + H \rightarrow {}^1CH_2O_2 + H_2$ calculated using CCSD(T)/maug-cc-pVTZ single point energies at B3LYP/MG3S geometries. Both the direct abstraction and the addition-elimination channels are shown. The figure includes the ZPE correction calculated using B3LYP/MG3S with frequency scaling.

1.5.3 PES Features of Interest for the Direct Abstraction

The full PES for reaction (6c) is 15 dimensional and thus difficult to visualize. To gain insight into the features of this PES of interest for the direct abstraction, we graphed the potential energy, V, as a function of two coordinates:

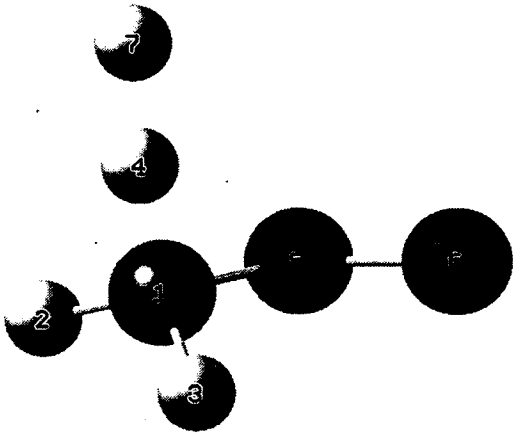

Figure 1-2 Atom numbering scheme used in the rest of this work.

the H(4)-H(7) distance (R_{HH}) and the C(1)-H(4) distance (R_{CH}). (Atom numbering is from Figure 1-2.) The other coordinates were varied to minimize the energy (except the C-H(4)-H(7) angle, which was fixed at 180° to prevent the minimization from yielding methyl hydroperoxide). For the purpose of illustration, the potential energy is shown for the B3LYP/3-21G level of theory in Figure 1-3, as a view from above and to the side of the surface, and in Figure 1-4, as a contour plot. On these plots, we can identify a reactant valley, a product valley, and an interaction region containing the saddle point.

The Minimum Energy Path (MEP) is the union of the paths of steepest descent from the saddle point towards the reactants and the products in mass weighted Cartesian coordinates. (Mass weighted coordinates are just the **R** coordinates (see section 1.3) multiplied by the square root of the atomic mass.) The MEP is the lowest energy path from reactants to products.[70-71] We found the MEP using the Page-McIver integrator[116] with a gradient step size of 0.005 Å and a Hessian step size of 0.045 Å. For the purpose of illustration, the 15 dimensional B3LYP/3-21G MEP, projected on the two-dimensional constrained PES, is shown by the red lines in Figures 1-3 and 1-4.

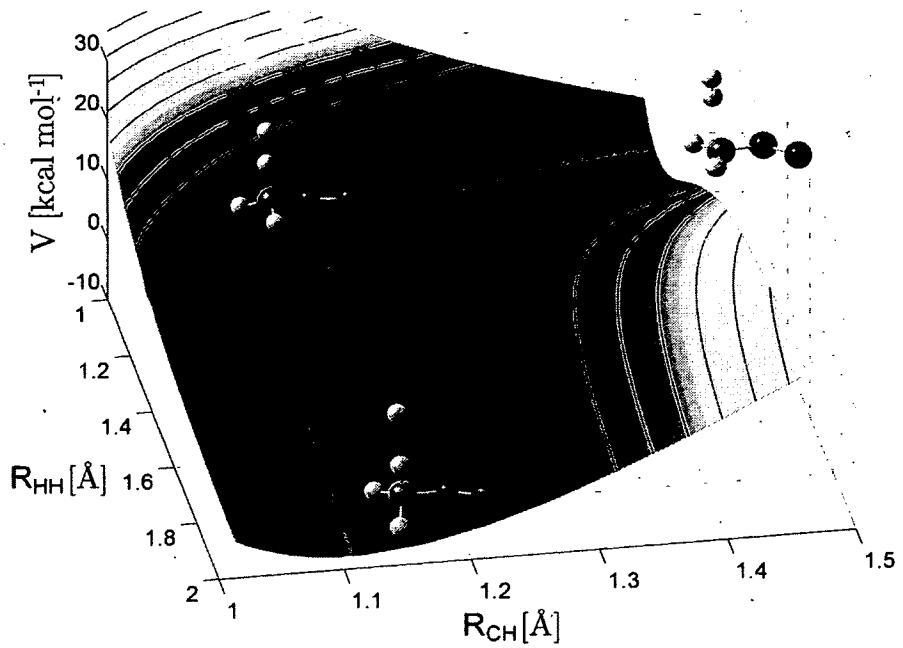

Figure 1-3. PES for direct abstraction at the B3LYP/3-21G level of theory. Red line is the MEP. R_{CH} is the C(1)-H(4) distance. R_{HH} is the H(4)-H(7) distance. (Atom numbering is from Figure 1-2).

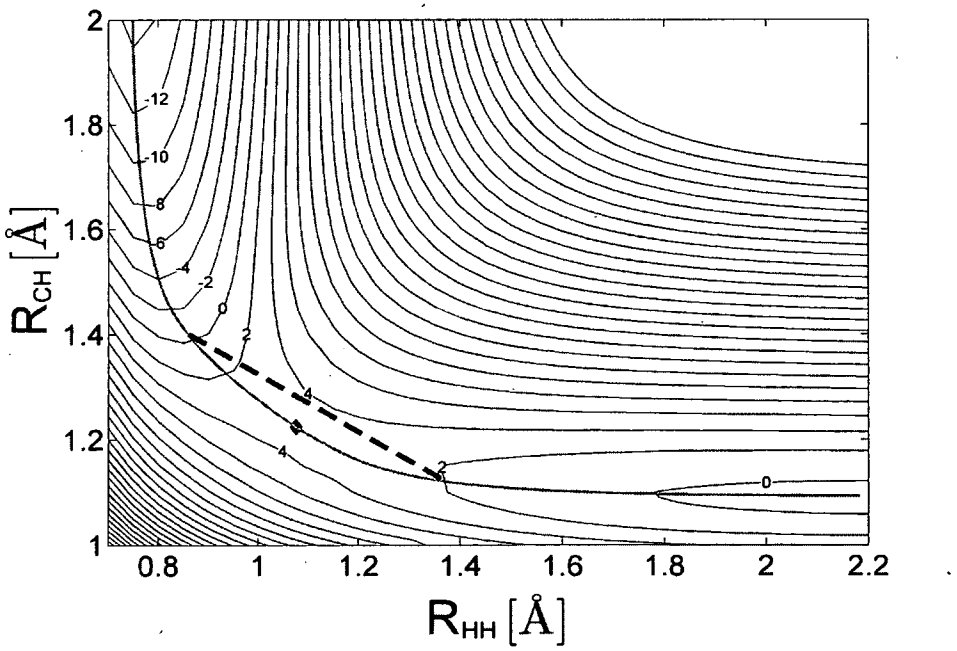

Figure 1-4. PES for direct abstraction at the B3LYP/3-21G level of theory, contour view. The diamond represents the saddle point. The red line is the MEP. The black line is a representative tunneling path (see section 1.10.1). R_{CH} is the C(1)-H(4) distance. R_{HH} is the H(4)-H(7) distance. (Atom numbering is from Figure 1-2). Contour labels are in kcal mol^{-1} relative to the reactants.

1.6 Choice of DFT Model Chemistry for Rate Constant Calculations

Though accurate, the CCSD(T) method is too time-consuming to use in VTST/MT calculations. DFT, on the other hand, is efficient enough for VTST/MT.

We evaluated the B3LYP[79-80], M06-L[105], ωB97X-D[103], MPW1K[107], and BB1K[109] density functionals in combination with different basis sets to find the model chemistry that best reproduces the CCSD(T) energies for the stationary points of the direct abstraction channel. For each model chemistry, we calculated the DFT energy of TS 1 relative to the reactants ($E_{DFT}(TS1)$), the DFT energy of the products relative to the reactants ($E_{DFT}(Prod)$), and the following quantities:

$$UE(TS1) = \left|E_{DFT}(TS1) - E_{CCSD(T)}(TS1)\right| \tag{19}$$

$$UE(Prod) = \left|E_{DFT}(Prod) - E_{CCSD(T)}(Prod)\right| \tag{20}$$

where $E_{CCSD(T)}(TS1)$ is the CCSD(T) energy of TS 1 relative to the reactants, $E_{CCSD(T)}(Prod)$ is the CCSD(T) energy of the products relative to the reactants, and *UE* stands for "unsigned error". *UE*(*TS 1*) and *UE*(*Prod*) are measures of how well a DFT model chemistry reproduces the CCSD(T) energies of TS 1 and the products, respectively. We also calculated the Mean Unsigned Error (*MUE*), given by

$$MUE = \left[UE(TS1) + UE(Prod)\right] / 2 \tag{21}$$

These results are given in Table 1-2. The method that has the lowest values of *UE*(*TS 1*), *UE*(*Prod*), and *MUE* would be the most suitable for use in VTST/MT calculations on the direct abstraction channel of reaction (6c).

Table 1-2. The DFT energies of TS 1 and the products relative to the reactants ($E_{DFT}(TS1)$ and $E_{DFT}(Prod)$), the unsigned errors in TS 1 and product energies ($UE(TS1)$ and $UE(Prod)$), and the Mean Unsigned Error (MUE), in kcal mol^{-1} relative to the reactants. The table includes the zero point energy (ZPE) correction with frequency scaling.

Method/Basis Set	$E_{DFT}(TS1)$	$E_{DFT}(Prod)$)	$UE(TS1)$	$UE(Prod)$	MUE
CCSD(T)/maug-cc-pVTZ[a,b]	6.53	-27.87			
B3LYP/MG3S	1.55	-27.83	4.99	0.04	2.51
B3LYP/6-31+G(d,p)	1.16	-27.53	5.38	0.34	2.86
B3LYP/6-31++G(d,p)	1.61	-26.98	4.92	0.89	2.90
ωB97X-D/MG3S	5.85	-23.09	0.69	4.79	2.74
ωB97X-D/6-31+G(d,p)	5.46	-22.88	1.07	4.99	3.03
ωB97X-D/6-31++G(d,p)	5.91	-22.21	0.62	5.66	3.14
M06-L/MG3S	4.39	-25.42	2.14	2.45	2.30
M06-L/MG3	4.37	-25.46	2.16	2.41	2.29
M06-L/6-31+G(d,p)	4.18	-25.07	2.36	2.80	2.58
M06-L/6-31++G(d,p)	4.30	-24.78	2.24	3.10	2.67
MPW1K/MG3S	5.93	-15.88	0.61	11.99	6.30
MPW1K/6-31+G(d,p)	5.92	-15.60	0.62	12.28	6.45
BB1K/MG3S	6.24	-20.83	0.30	7.05	3.67
BB1K/6-31+G(d,p)	6.05	-20.23	0.49	7.65	4.07

[a]ZPE correction at B3LYP/MG3S level of theory
[b]Given for comparison

We found that the DFT method that gives the lowest $UE(Prod)$ is B3LYP/MG3S but that it underestimates the CCSD(T) energy of TS 1 by ~5 kcal mol^{-1} (see Table 1-2). This was expected, because, as stated in section 1.4.1, B3LYP frequently underestimates reaction barriers. The DFT methods that gave the lowest $UE(TS1)$ are MPW1K and BB1K. However, they gave $UE(Prod)$ of ~12 kcal mol^{-1} and ~7 kcal mol^{-1}, respectively (see Table 1-2). This is also not surprising, given that both functionals contain a high percentage of Hartree-Fock exchange. This is known to improve a functional's performance for reaction barriers, at the expense of accuracy for reaction energies.[73] ωB97X-D gave $UE(TS1)$ values comparable to MPW1K and BB1K and

UE(*Prod*) ≈ 5 kcal mol^{-1} (see Table 1-2). The best balance of accuracy in TS 1 energy and product energy is given by the M06- L functional. However, we chose B3LYP, since it gives *MUE*s comparable to the M06-L *MUE*s (see Table 1-2), and it was available on our faster computer.

For each functional, we tested the difference between a double-ζ basis set with relatively few polarization functions (6-31+G(d,p)) and a triple-ζ basis set with more polarization functions (MG3S). (See section 1.4.3) Using MG3S led to better agreement with the CCSD(T) results, as seen in Table 1-2. For B3LYP, M06-L, and ωB97X-D, we tested the effect of adding diffuse functions on hydrogen atoms in the 6-31+G(d,p) basis set, which gives the 6-31++G(d,p) basis set (see section 1.4.3). This increased the *MUE* in all three cases (see Table 1-2).

For M06-L, we also tested the effect of adding diffuse functions on hydrogen to the MG3S basis set, giving MG3 (see section 1.4.3). As seen in Table 1-2, this had essentially no effect on the *MUE*.

For practical considerations, our final choice of method was B3LYP/MG3S.

1.7 Conventional Transition State Theory (TST)

1.7.1 Theoretical Background

Transition State Theory (TST) is a time-tested method for calculating rate constants.[70-71, 117-118] It is formulated by imagining the bimolecular reaction (11) as a two step process in which the reactants, A and B, are in equilibrium with a transient activated complex on the path from reactants to products, [A--B]‡. This activated complex is also

referred to as the transition state (TS).[1] The transition state is irreversibly converted to products. In conventional TST, the saddle point geometry is assumed to correspond to the transition state. We will refer to this species as the "conventional transition state".

The chemical equation for this process is[117-118]

$$A + B \underset{k_{-1}(T)}{\overset{k_1(T)}{\rightleftharpoons}} [A\text{--}B]^{\ddagger} \xrightarrow{k_2(T)} \text{Products} \qquad (22)$$

where $k_1(T)$ is the rate constant for conversion of reactants to the transition state, $k_{-1}(T)$ is the rate constant for the reverse reaction, and $k_2(T)$ is the rate constant for conversion of the transition state to products.

Assuming the steady state approximation, the conventional TST rate constant ($k^{\ddagger}(T)$) is given by[118]

$$k^{\ddagger}(T) = \frac{k_1(T)}{k_{-1}(T)} k_2(T) = K^{\ddagger}(T)\, k_2 \qquad (23)$$

where $K^{\ddagger}(T)$ is the equilibrium constant for the formation of the conventional transition state.

$k_2(T)$ is given by[118]

$$k_2(T) = \frac{k_B T}{h} \qquad (24)$$

where k_B is Boltzmann's constant, and h is Planck's constant. Combining equations (23) and (24) gives the following equation for $k^{\ddagger}(T)$[118]:

$$k^{\ddagger}(T) = \frac{k_B T}{h} K^{\ddagger}(T) \qquad (25)$$

In an analogy to thermodynamics, $K^{\ddagger}(T)$ is given by[70-71, 118]

[1] This is a commonly used, but inexact, definition of the transition state. The reader is referred to references 70-71 for a more rigorous discussion of the relationship between the transition state and the activated complex.

$$K^{\ddagger}(T) = K^{\ddagger,o} \exp\left(-\frac{\Delta G_a^{\ddagger,o}(T)}{k_B T}\right) \tag{26}$$

where $\Delta G_a^{\ddagger,o}(T)$ is the conventional standard free energy of activation and $K^{\ddagger,o}$ is the standard state reaction quotient. (For our choice of standard state, $K^{\ddagger,o}$ = 1 cm^3 molec^{-1} s^{-1}). The conventional TST rate constant is thus given by

$$k^{\ddagger}(T) = \frac{k_B T}{h} K^{\ddagger,o} \exp\left(-\frac{\Delta G_a^{\ddagger,o}(T)}{k_B T}\right) \tag{27}$$

From statistical mechanics,[118]

$$\Delta G_a^{\ddagger,o}(T) = V^{\ddagger} - k_B T \ln\left[\frac{Q'^{\ddagger}(T)}{K^{\ddagger,o} Q_A(T) Q_B(T)}\right] \tag{28}$$

where $V^{\ddagger}$ and $Q'^{\ddagger}(T)$ are the potential energy and partition function of the conventional transition state, respectively, and $Q_A(T)$ and $Q_B(T)$ are the partition functions of reactant A and reactant B, respectively.

"The partition function gives the number of energy states accessible to the system at a given temperature ($\sum_i e^{-\varepsilon_i / k_B T}$) and links the macroscopic properties of a system to averages of microscopic quantum states."[119] The overall partition function is the product of the vibrational, rotational, translational, and electronic partition functions.[120] The formulas for the partition functions can be found in many introductory physical chemistry texts.[120]

The vibrational partition function is a product of the partition functions for each vibrational mode. Typically, the modes are assumed to be harmonic in nature, in which case they are referred to as "normal modes". Each mode's partition function depends on the frequency of that mode and on the physical model used to represent it. Quantization

of the vibrations is typically included by using the quantum mechanical form of the harmonic oscillator partition function. Low frequency vibrational modes have many available energy states and thus high partition functions. Conversely, high frequency vibrational modes have low partition functions.

Note that the transition state is missing one vibrational degree of freedom compared to the reactants.[70-71, 118] In conventional TST, this degree of freedom corresponds to the imaginary frequency vibrational mode at the saddle point. The effect of this degree of freedom on the rate constant (which is quantum in nature) is discussed in section 1.10.

Also note that we have assumed that the reactants and transition state have a thermal distribution of energies (a canonical ensemble). A version of TST in which the reactants and transition state have a specific energy (a microcanonical ensemble) also exists,[70-71] but is not used in this work.

To match the notation of references 70-71, we rewrite equation (28) in the form

$$\Delta G_a^{\ddagger,o}(T) = V^{\ddagger} - k_B T \, \sigma \ln\left[\frac{Q^{\ddagger}(T)}{K^{\ddagger,o}\Phi^{R}(T)}\right] \tag{29}$$

where $Q^{\ddagger}(T)$ is very similar to the conventional transition state partition function $Q^{\ddagger}(T)$, except that the rotational symmetry numbers and stereochemical factors[121] are neglected, $\Phi^{R}(T)$ is the product of the reactant partition functions with the rotational symmetry numbers and stereochemical factors omitted, and σ is referred to as the symmetry factor.

σ accounts for the rotational symmetry and chirality of the reactants and the transition state. It is given by[121]

$$\sigma = \frac{\sigma_R \, n_{TS}}{\sigma_{TS} \, n_R} \tag{30}$$

where σ_R and σ_{TS} are the symmetry numbers of the rotational partition functions of the reactants and the transition state, respectively. For reaction (6c) $\sigma_R = \sigma_{TS} = 1$, because neither the peroxymethyl radical nor the transition state have indistinguishable configurations that are interconverted by a rotation. n_R and n_{TS} are the numbers of enantiomers for each species. The peroxymethyl radical has mirror symmetry ($n_R = 1$), while the transition state is chiral, with two enantiomers. ($n_{TS} = 2$). The overall symmetry number is thus $\sigma = 2$.

Combining equations (27) and (29) gives the following equation for the conventional TST rate constant:

$$k^{\ddagger}(T) = \sigma \frac{k_B T}{h} \frac{Q^{\ddagger}(T)}{\Phi^R(T)} \exp\left[-\frac{V^{\ddagger}}{k_B T}\right] \tag{31}$$

The reader is referred to several texts and review articles for further details and alternative derivations of conventional TST.[70-71, 118]

1.7.2 Conventional TST Rate Constant for Reaction (6c)

The rate constant for the direct abstraction pathway of reaction (6c), calculated using conventional TST, is shown in Figure 1-5 for the temperature range 100 K < T < 2000 K. Note that the rate constant obeys the Arrhenius relation (the plot of ln(k) vs $1/T$ is linear) for 100 K < T < 300 K (3.3 < $1/T$ < 10) but deviates from it at high temperatures.

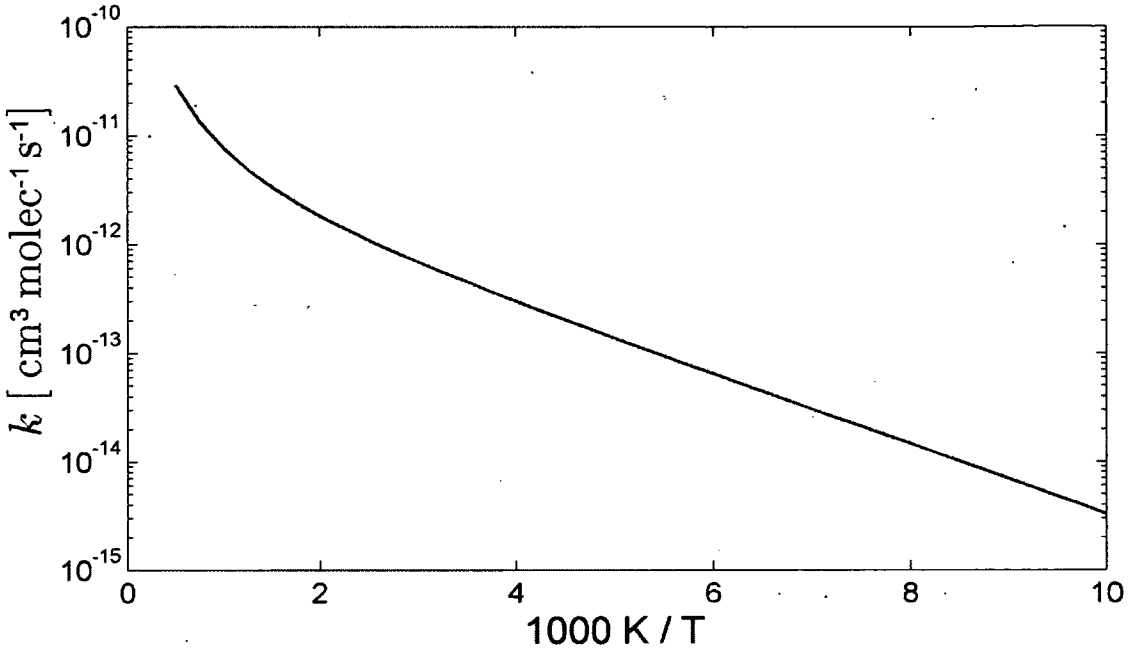

Figure 1-5. Conventional TST rate constant for the direct abstraction channel of the reaction $CH_3O_2 + H \rightarrow {}^1CH_2O_2 + H_2$ calculated using B3LYP/MG3S level of theory and the harmonic oscillator model for all vibrational modes.

1.8 Hindered Rotor Approximation

Both the direct abstraction transition state and the peroxymethyl radical have one vibrational mode with frequency lower than 150 cm^{-1} (see Table 1-1). Recall from section 1.7.1 that low frequency vibrational modes make large contributions to the partition function. It is thus particularly important that the partition functions for these modes be calculated accurately.

From examining the Hessian eigenvectors corresponding to these modes, it becomes apparent that they correspond to torsions about the C-O bond. Studies of the methanol-hydrogen reaction (reaction (18))[114-115] and related systems,[122] as well as studies of other peroxy radical reactions,[123] found that the harmonic oscillator (HO) model, which was used to calculate all vibrational partition functions in section 1.7.2, is

not appropriate for such torsional modes. It was determined that a hindered rotor (HR) model should be used to calculate the partition functions of these modes.

We used the segmented reference Pitzer-Gwinn (SRPG)[124] equation for the hindered rotor partition function, which is the recommended method in POLYRATE. The SRPG partition function tends to the harmonic oscillator partition function at low temperature. At higher temperatures, the anharmonicity becomes important, and the two diverge.[124]

The SRPG formula requires the torsion potential. The torsion potential for the direct abstraction transition state is shown in Figure 1-6. The potential was found by fixing the C-H(4) and H(4)-H(7) bond lengths, the H(4)-C-O(5), C-H(4)-H(7), C-O(5)-O(6) bond angles and scanning the O(6)-O(5)-C-H(4) dihedral angle at 5° intervals, while minimizing the energy with respect to the other coordinates. The potential has two

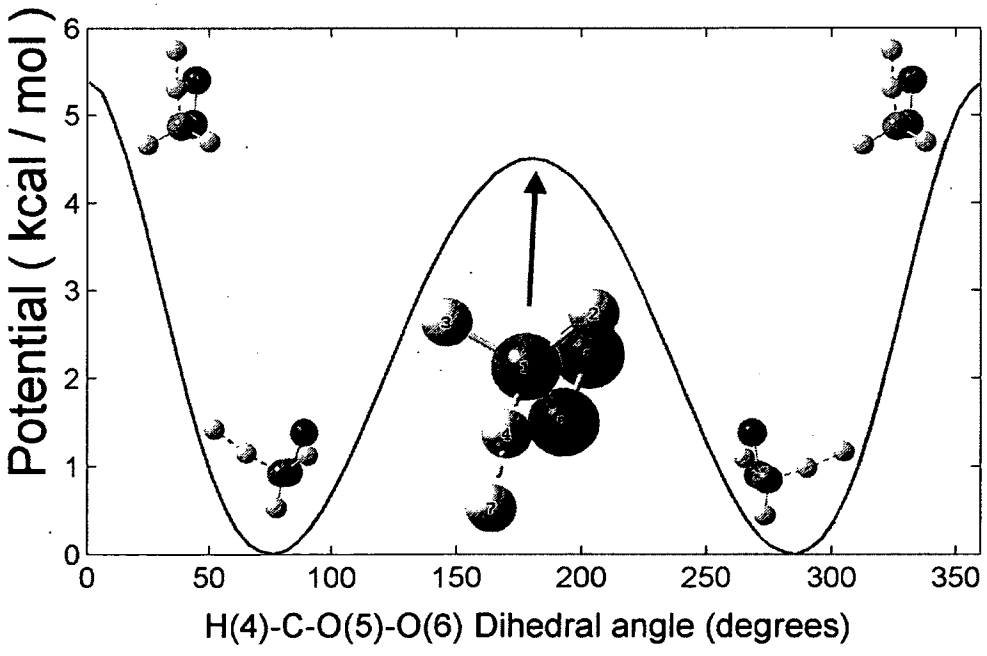

Figure 1-6. Torsion potential for the direct abstraction transition state calculated using the B3LYP/MG3S level of theory.

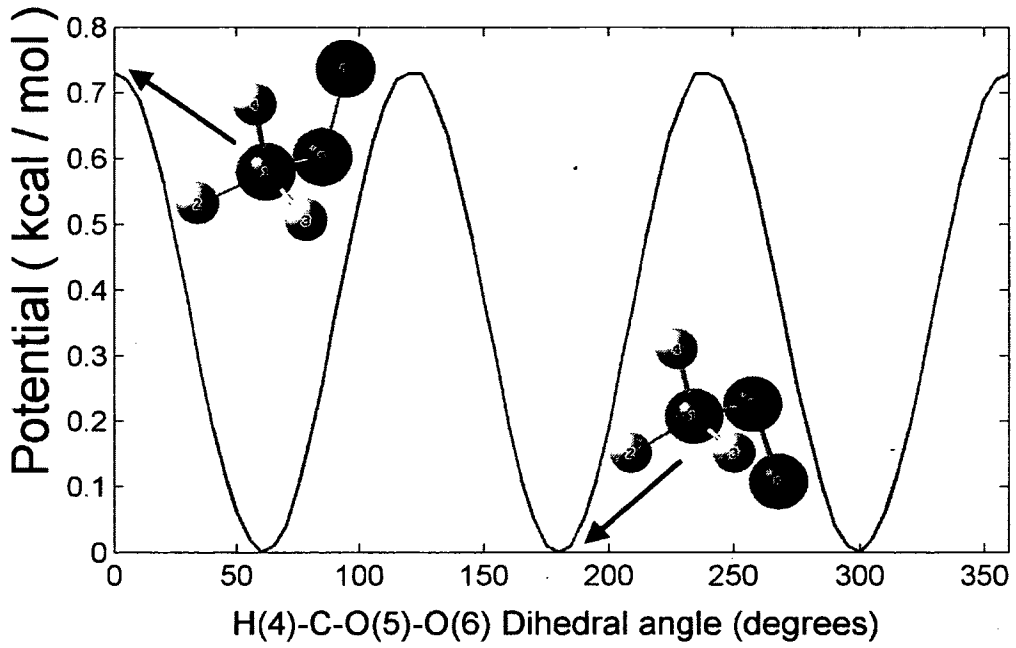

Figure 1-7. Torsion potential for the peroxymethyl radical calculated using the B3LYP/MG3S level of theory.

minima, corresponding to the two enantiomers of the transition state (dihedral = 72.7°), with maxima of unequal heights at the eclipsed (dihedral = 0°) and anti (dihedral = 180°) conformations. The barrier heights are 5.3 and 4.5 kcal mol^{-1}, respectively. This is very similar to the potential found for the equivalent torsional mode in $CH_3OH + H$.[114-115]

The torsion potential for CH_3O_2 is shown in Figure 1-7. The potential was found by scanning the O(6)-O(5)-C-H(4) dihedral angle without additional constraints. The potential has three equivalent minima, corresponding to the gauche conformation, and three equivalent maxima, corresponding to the eclipsed conformation. The barrier to rotation is 0.7 kcal mol^{-1}.

The importance of using the hindered rotor approximation is illustrated in Figure 1-8, which shows the ratio of the conventional TST rate constants calculated using the hindered rotor approximation (k_{HR}) and the harmonic oscillator approximation (k_{HO}). The

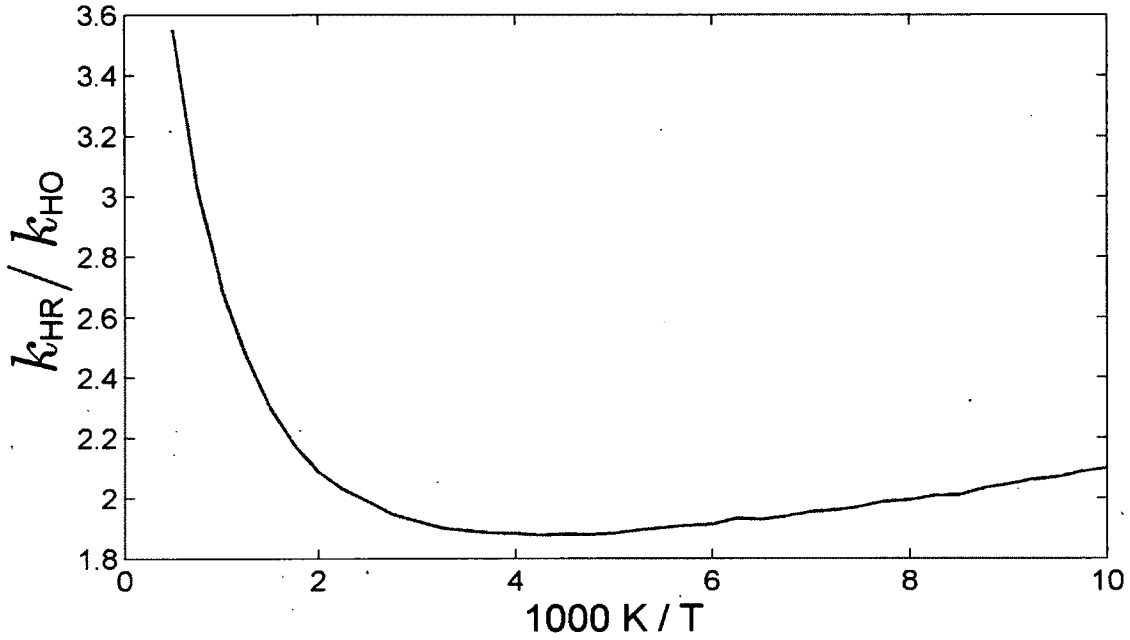

Figure 1-8. The ratio of the rate constant for the direct abstraction channel of the reaction $CH_3O_2 + H \rightarrow {}^1CH_2O_2 + H_2$ calculated using the hindered rotor approximation for torsion about the C-O bond (k_{HR}) to the rate constant calculated with the harmonic-oscillator approximation (k_{HO}). The calculations were carried out using conventional TST with the B3LYP/MG3S density functional approximation. The other vibrational modes in both calculations were treated as harmonic oscillators.

hindered rotor rate constant is higher by at least a factor of 1.9 at all temperatures. For this reason, all calculations reported from this point on use the hindered rotor approximation to calculate the partition function of the torsional mode in the transition state and the peroxymethyl radical.

1.9 Canonical Variational Theory (CVT)

1.9.1 Theoretical Background

Variational Transition State Theory (VTST)[70-71] is an improvement on conventional TST. It is based on two premises. The first is that geometries other than the one corresponding to the saddle point can be used as the transition state, as long as

they are located on a path connecting the reactants and products on the PES (the reaction path). Such transition states are referred to as generalized transition states (GTS).[70-71]

Typically, the Minimum Energy Path (MEP) is used as the reaction path. (See section 1.5.3 for the definition of the MEP). The location of a GTS on the MEP is given by s, where s is the arc path length along the MEP from the saddle point to the GTS (s=0 at the saddle point, $s < 0$ on the reactant side of the MEP, and $s > 0$ on the product side). s is referred to as the "reaction coordinate".

For every value of s, we can calculate a generalized standard free energy of activation, $\Delta G_a^{GT,o}(T,s)$, analogous to the conventional standard free energy of activation given by equation (29)

$$\Delta G_a^{GT,o}(T,s) = V^{GT}(s) - k_B T \sigma \ln\left[\frac{Q^{GT}(T,s)}{K^{\ddagger,o}\Phi^R(T)}\right] \qquad (32)$$

where $V^{GT}(s)$ and $Q^{GT}(T,s)$ are the potential energy and the partition function of the generalized transition state, respectively.

The translational and electronic partition functions do not depend on s, and the rotational partition function varies slowly with s. Most of the changes in $Q^{GT}(T,s)$ that occur as the MEP is traversed from reactants to products are due to changes in the vibrational partition function. One difference between the conventional TS and the GTS is that, in general, the GTS does not correspond to a stationary point on the PES. The vibrational part of $Q^{GT}(T,s)$ is calculated using vibrational modes orthogonal to the MEP at the GTS, which are known as generalized vibrational modes. To obtain the generalized vibrational modes and their frequencies, a special projection technique is applied to the Hessian matrix (see section 1.3) before it is diagonalized.[125]

From $\Delta G_a^{GT,o}(T,s)$, a generalized TST rate constant, $k^{GT}(T,s)$ can be calculated analogously to the conventional TST rate constant calculated using equation (27).

$$k^{GT}(T,s) = \frac{k_B T}{h} K^{\ddagger,o} \exp\left(-\frac{\Delta G^{GT,o}_a(T,s)}{k_B T}\right) \tag{33}$$

The crucial result that leads to VTST is that, for a strictly classical system, any TST rate constant overestimates the true rate constant.[70-71] This implies that, to obtain the best estimate for the rate constant, one should minimize $k^{GT}(T, s)$ with respect to s, or equivalently, maximize $\Delta G_a^{GT,o}(T,s)$. The canonical version of VTST, also referred to as Canonical Variational Theory (CVT), gives the rate constant as

$$k^{CVT}(T) = \frac{k_B T}{h} K^{\ddagger,o} \exp\left(-\frac{\Delta G^{CVT,o}_a(T)}{k_B T}\right) \tag{34}$$

where

$$\Delta G_a^{CVT,o}(T) = \max_s \Delta G_a^{GT,o}(T,s) \tag{35}$$

is the CVT standard free energy of activation, and $\max_s$ denotes that the maximum $\Delta G_a^{GT,o}(T,s)$ along the reaction path, s, has been obtained.

The difference between the conventional TST and CVT approaches is illustrated in Figure 1-9 for the direct abstraction channel of reaction (6c). Conventional TST places the transition state at the saddle point, which has the highest potential energy of all points along the MEP. (The potential energy along the MEP, $V_{MEP}(s)$, calculated with the B3LYP/6-31++G(d,p) model chemistry, is shown in Figure 1-9(a)). However, this may not be the optimal placement, because it neglects the partition function contribution to the standard free energy of activation.

The solid black curve in Figure 1-9(b) shows the plot of $\Delta G_a^{GT,o}(0\ K, s)$ (see equation 32), also known as the vibrationally adiabatic ground state potential, $V_{ag}(s)$,

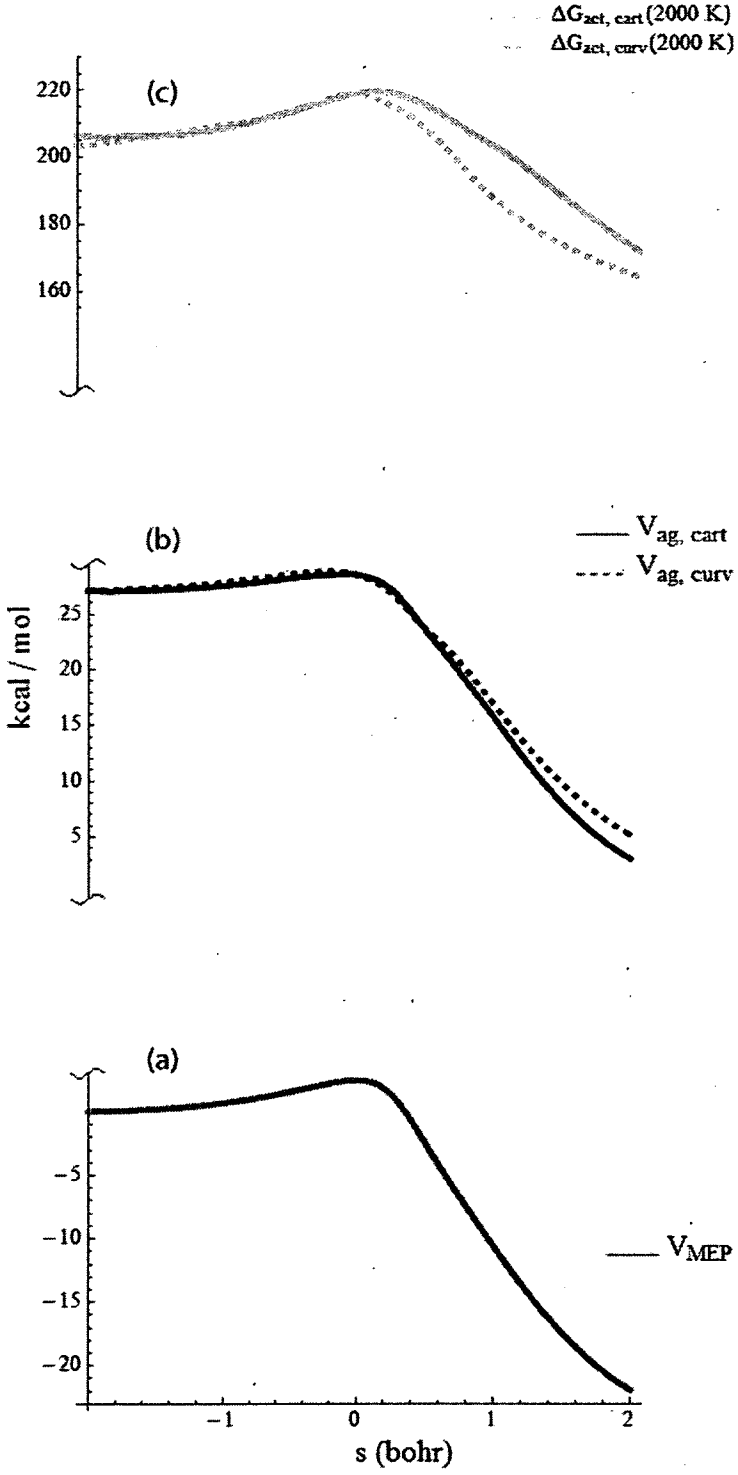

Figure 1-9.
Relevant energy barriers for the direct abstraction channel of reaction (6c), calculated using B3LYP/6-31++G(d,p)

(a) potential along MEP (V_{MEP}, red line)

(b) vibrationally adiabatic ground state potential (V_{ag}), i.e. the sum of V_{MEP} and the ZPEs of all normal modes transverse to the reaction coordinate:

(b-1) V_{ag} calculated using Cartesian coordinates, ($V_{ag,\ cart}$ solid black line)

(b-2) V_{ag} calculated using redundant curvilinear coordinates, ($V_{ag,\ curv,}$, dashed black line)

(c) standard activation free energy profile at 2000 K ($\Delta G_{act}(2000\ K)$)

(c-1) $\Delta G_{act}(2000\ K)$ calculated using Cartesian coordinates ($\Delta G_{act,\ cart}(2000\ K)$, solid green line)

(c-2) $\Delta G_{act}(2000\ K)$ calculated using redundant curvilinear coordinates ($\Delta G_{act,\ curv}(2000\ K)$, dashed green line)

calculated using the same DFT approximation. Note that the peak of $V_{ag}(s)$ is shifted from the peak of $V_{MEP}(s)$ t towards the reactant valley (i.e. at 0 K conventional TST overestimates the rate constant).

At high temperatures, the peak of $\Delta G_a^{GT,o}(T,s)$ moves back towards the saddle point. The peak of $\Delta G_a^{GT,o}(2000\ K,s)$ given by the solid green curve in Figure 1-9(c), coincides with the peak of $V_{MEP}(s)$ (i.e. at 2000 K the conventional TST and CVT rate constants are equal).

1.9.2 Interpolated VTST with Mapping (IVTST-M)

As stated in section 1.5.3, we found the MEP for CVT calculations using the Page-McIver integrator[116] with a gradient step size of 0.005 Å and a Hessian step size of 0.045 Å. It would be burdensome to calculate the full MEP with a large basis set like MG3S. Instead, the MEP was found only on the interval -1.0 Å $< s <$ 0.5 Å, where s is the reaction coordinate. The MEP was then extrapolated to -3 Å $< s <$ 3 Å using the Interpolated VTST with Mapping (IVTST-M)[126] algorithm. This calculation is denoted by IVTST-M-33/202, meaning that the gradient was calculated at 202 points and the Hessian at 33.

1.9.3 Canonical Variational Theory (CVT) Using Cartesian Coordinates

Recall from section 1.9.1 that the CVT rate constant depends on the frequencies of the generalized vibrational modes. Because the GTS is not, in general, a stationary point on the PES, these frequencies depend on the choice of coordinates used to represent the nuclear motion.[70, 127-128] This problem does not arise in conventional TST, because vibrational frequencies at stationary points do not depend on the coordinate system, and the conventional TS is a stationary point (a saddle point, to be exact).[70, 127-128]

Figure 1-10 gives the CVT rate constant for reaction (6c) calculated using the Cartesian coordinates **R** from section 1.3 for vibrational analysis along the MEP. The TST rate constant is also given for comparison. Note that below ~300 K (1000 K / T > 3.3), the CVT rate constant is lower than the conventional TST value and is thus a better approximation to the true rate constant by the discussion in section 1.9.1.

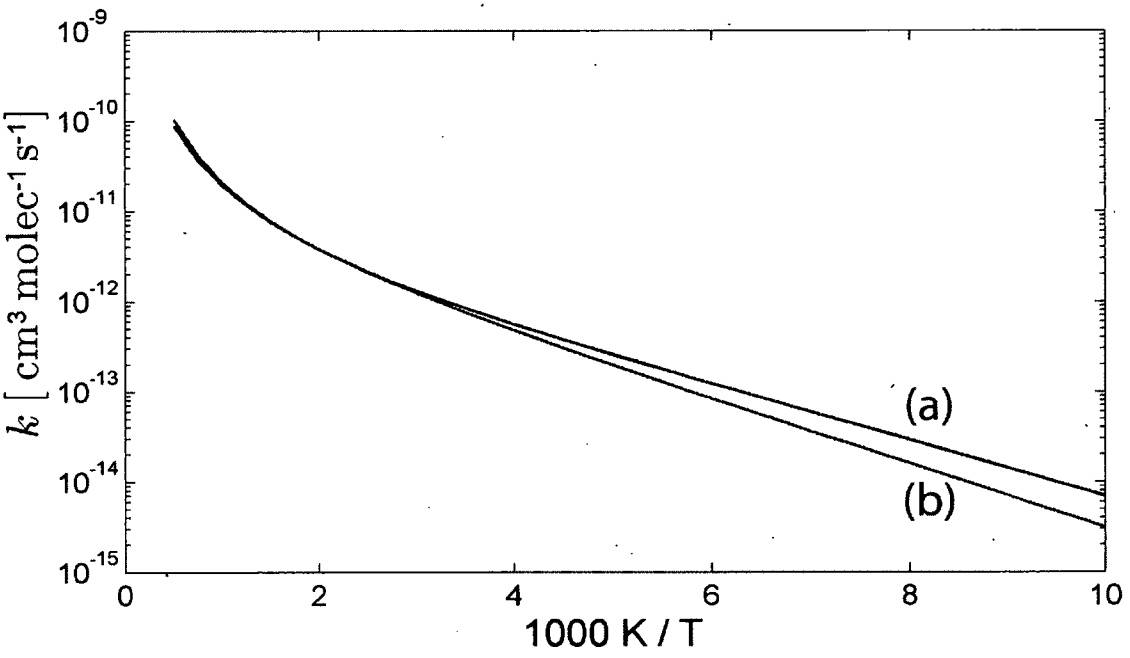

Figure 1-10. Rate constant for the direct abstraction channel of the reaction $CH_3O_2 + H \rightarrow {}^1CH_2O_2 + H_2$ calculated using **(a)** conventional TST **(b)** CVT using Cartesian coordinates for vibrational analysis at the generalized transition states. Both calculations were performed using the B3LYP/MG3S DFT approximation. The torsional modes of CH_3O_2 and the transition state were treated using the hindered rotor approximation. The harmonic oscillator model was used for all other vibrational modes.

1.9.4 Canonical Variational Theory (CVT) Using Redundant Curvilinear Coordinates

Generalized vibrational frequencies calculated using Cartesian coordinates are often unphysical, because atoms are constrained to move along straight lines in the vibrational modes. This will lead to admixture of a bond stretching component into a bending or torsion mode, resulting in spuriously imaginary frequencies for low frequency

modes.[70, 127-128] In an H abstraction reaction, it is typical for the lowest frequency to be imaginary over much of the reaction coordinate.[127-135]

The solution is to use more general curvilinear coordinates. Curvilinear coordinates are those that are non-linear functions of Cartesian coordinates.[70, 127, 129, 131, 136] POLYRATE allows for the use of so-called valence coordinates for the vibrational analysis at the generalized transition state. These consist of stretch, bend, and torsion coordinates, which provide a more physical picture of the generalized vibrational modes and yield more accurate frequencies.[127, 129, 131] We used redundant curvilinear coordinates, which allow for the use of more than 3N-6 coordinates.[136]

The CVT rate constants for the direct abstraction channel of reaction (6c)

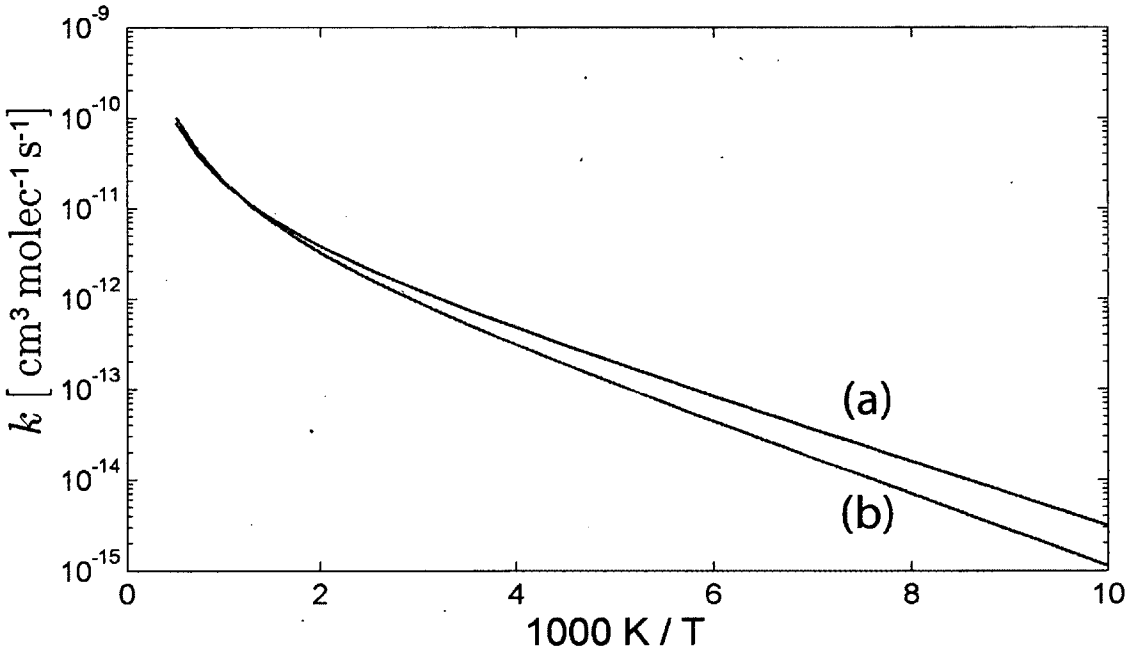

Figure 1-11. Rate constant for the direct abstraction channel of the reaction $CH_3O_2 + H \rightarrow {}^1CH_2O_2 + H_2$ calculated with the CVT method using **(a)** Cartesian coordinates and **(b)** redundant curvilinear coordinates for vibrational analysis at the generalized transition states. Both calculations were performed using the B3LYP/MG3S DFT approximation. The torsional modes of CH_3O_2 and the transition state were treated using the hindered rotor approximation. The harmonic oscillator model was used for all other vibrational modes.

calculated using CVT with both Cartesian and redundant curvilinear coordinates are shown in Figure 1-11. For $T < 500$ K (1000 K/ $T > 2$), CVT with redundant curvilinear coordinates gives lower rate constants.

The reason for this discrepancy is demonstrated in Figures 1-9(b)-(c). In those figures, the $V_{ag}(s)$ and $\Delta G_a^{GT,o}(2000\ K, s)$ calculated using Cartesian coordinates (solid lines) and curvilinear coordinates (dashed lines) are different. (See section 1.9.1 for the definitions of $V_{ag}(s)$ and $\Delta G_a^{GT,o}(2000\ K, s)$) and for the reason why this difference would affect the rate constant).

Rate constants calculated using curvilinear coordinates have been found to give better agreement with experiment than those calculated using Cartesian coordinates.[127-133, 135-136] For this reason, we recommend rate constants and isotope effects calculated using CVT with curvilinear coordinates.

1.10 CVT with Multidimensional Tunneling (CVT/MT)

1.10.1 Theoretical Background

Recall from section 1.7.1 that the transition state is missing one vibrational degree of freedom compared to the reactants. This degree of freedom corresponds to motion along the reaction coordinate (the imaginary frequency normal mode at the conventional TS and the MEP at a generalized TS).[70-71, 118] The $\frac{k_B T}{h}$ factor in the formulas for the conventional TST rate constant (equation (31)) and the CVT rate constant (equation (34)) is obtained by assuming that motion along this coordinate obeys classical mechanics.[70-71, 118] However, chemical reactions occur on the microscopic scale where the laws of quantum mechanics apply.

In quantum mechanics, a particle with insufficient energy to cross a potential energy barrier has a finite probability of being found on the other side, and a particle with enough energy to cross may be reflected. These phenomena are collectively known as "tunneling".[137]

Tunneling causes equations (31) and (34) to underestimate the rate constant.[70-71, 138] A multiplicative transmission coefficient, $\kappa^t(T)$, is added to the TST equation for the rate constant, where t denotes the approximation used to calculate the transmission coefficient.[70-71, 123, 139]

For accurate results, the approximation used to calculate $\kappa^t(T)$ should incorporate the effects of the vibrational degrees of freedom transverse to the reaction coordinate on the tunneling rate. This class of methods is referred to as Multidimensional Tunneling (MT). [70-71, 123, 139] When one of these is used in combination with VTST, the resulting theory is called Variational Transition State Theory with Multidimensional Tunneling (VTST/MT). [70-71, 123, 139] When one is used in conjunction with the CVT variant of VTST, the resulting approach is called Canonical Variational Theory with Multidimensional Tunneling (CVT/MT). [70-71, 123, 139] We used CVT/MT in this work.

The form of the CVT/MT equation that we used is

$$k^{CVT/t}(T) = \frac{k_B T}{h} \kappa^t(T) K^{\ddagger,o} \exp\left(-\frac{\Delta G^{CVT,o}_a(T)}{k_B T}\right) \tag{36}$$

where $k^{CVT/t}(T)$ is the tunneling corrected CVT rate constant (cf. equation 34).

In the context of CVT/MT, $\kappa^t(T)$ is given by[70-71, 123, 139]

$$\kappa^{CVT/t}(T) = \frac{1}{k_B T} \exp\left\{\frac{V_{ag}[(s_{CVT}(T)]}{k_B T}\right\} \int_0^\infty dE \exp\left(-\frac{E}{k_B T}\right) P'(E) \tag{37}$$

where $V_{ag}(s)$ and s were defined in section 1.9.1, $s_{CVT}(T)$ is the value of s at the CVT transition state, E is the tunneling energy, and $P'(E)$ is the microcanonical transmission probability calculated using approximation t.

The multidimensional $P'(E)$ can be calculated using one of three methods.[70-71, 123, 139] In the least sophisticated approximation, one assumes that tunneling occurs only along the MEP, and that the potential for tunneling is $V_{ag}(s)$.[70-71, 123, 139] This is referred to as the Zero Curvature Tunneling (ZCT) approximation.[70-71, 123, 139] The equation for $P^{ZCT}(E)$ can be found in several references listed at the end of this work.[70-71, 123, 139-140] We denote the ZCT transmission coefficient by $\kappa^{CVT/ZCT}(T)$ and the corresponding CVT/MT rate constant by $k^{CVT/ZCT}(T)$.

A drawback of ZCT is that it neglects coupling between the reaction coordinate and orthogonal vibrational modes, which is known as the corner-cutting effect. The name comes from the fact that tunneling paths that "cut the corner" on the concave side of the MEP (see Figure 1-4) contribute to the transmission coefficient.[70-71, 123, 139] Because ZCT neglects corner-cutting, it significantly underestimates tunneling.[70-71, 141]

In the limit of small MEP curvature, the microcanonical transmission probability is calculated using the Small Curvature Tunneling (SCT) approximation.[70-71, 123, 139] The formula for calculating $P^{SCT}(E)$ can be found elsewhere.[70-71, 142] We denote the SCT transmission coefficient by $\kappa^{CVT/SCT}(T)$ and the corresponding CVT/MT rate constant by $k^{CVT/SCT}(T)$.

For tightly-curved MEPs, the Large Curvature Tunneling (LCT)[70-71, 123, 139] approximation must be used. The reader is referred elsewhere for the details of calculating $P^{LCT}(E)$.[70-71, 143] We use the $\kappa^{CVT/LCT}(T)$ notation to refer to the LCT

transmission coefficient and $k^{CVT/LCT}(T)$ to refer to CVT rate constants corrected for tunneling using the LCT approximation.

In the case of intermediate curvature, the recommended approach is microcanonically optimized multidimensional tunneling (μOMT), in which the larger of $P^{SCT}(E)$ and $P^{LCT}(E)$ is used as $P_{\mu}^{OPT}(E)$ for each tunneling energy E.[70-71, 123, 139] The corresponding transmission coefficient and rate constant are written as $\kappa^{CVT/_{\mu}OPT}(T)$ and $k^{CVT/_{\mu}OPT}(T)$, respectively.

1.10.2 Choice of Multidimensional Tunneling (MT) Approximation and General Observations about Tunneling in This System

Low temperature rate constants for hydrogen transfer reactions, such as reaction (6c), are nearly always dominated by tunneling,[144] and the choice of tunneling approximation has a substantial effect on the rate constants[144] and isotope effects[145] for these systems.

Table 1-3 gives tunneling corrections for the direct H abstraction, calculated with the ZCT, SCT, LCT and μOMT approximations using the 6-31++G(d,p) basis set, based on the reaction path of -1.0 Å < s < 0.5 Å. The small basis set and limited reaction coordinate range were used because LCT calculations require much more computational time than SCT and cannot be used with the IVTST-M algorithm (see section 1.9.2).

Table 1-3 shows that:

1) The μOMT correction is exclusively attributable to SCT. All subsequent results are calculated using the SCT approximation.

Table 1-3. Multidimensional tunneling corrections, κ(T), of the direct H abstraction based on the reaction path of -1.0 Å < s < 0.5 Å at B3LYP/6-31++G(d,p) level of theory

T (K)	$\kappa^{CVT/ZCT}(T)$	$\kappa^{CVT/SCT}(T)$	$\kappa^{CVT/LCT}(T)$	$\kappa^{SCT,OMT}(T)$
100	18.70	36.83	22.54	36.83
200	2.06	2.54	2.19	2.55
300	1.36	1.50	1.40	1.50
400	1.16	1.23	1.18	1.23
500	1.07	1.11	1.08	1.11
600	1.02	1.05	1.03	1.05
700	0.99	1.01	0.99	1.01
800	0.97	0.98	0.97	0.98
900	0.95	0.97	0.96	0.97
1000	0.95	0.95	0.95	0.95

2) ZCT underestimates tunneling by up to 50% at low temperatures. For this reason, we recommend rate constants and isotope effects calculated using SCT and give the ZCT results for comparison only.

3) At 100 K SCT tunneling enhances the rate constant by a factor of ~37 compared to the CVT only rate constant, but the enhancement falls off quickly with temperature. At room temperature, tunneling raises $k(T)$ only by a factor of 1.5. Above 300 K, tunneling is relatively unimportant.

4) Above 700 K, non-classical reflection slightly slows down the reaction.

$\kappa^{CVT/SCT}$(T) can be sensitive to the gradient step size used to calculate the MEP. Convergence with respect to the step size was checked by re-computing $k^{CVT/SCT}(T)$ for the direct abstraction with a step size of 0.0025 Å using the 6-31++G(d,p) basis set. Compared to the 0.005 Å step size results, $k^{CVT}(T)$ was converged to within 0.8% and $\kappa^{CVT/SCT}$(T) was converged to within 17%, with the biggest discrepancy at low temperatures. The results were deemed sufficiently converged.

1.10.3 CVT/MT Rate Constants for the Direct Abstraction Channel

The Arrhenius plots for the direct abstraction channel of reaction (6c), calculated using the conventional TST (see section 1.7.1), CVT (see section 1.9.1), CVT/ZCT, and CVT/SCT approximations (see section 1.10.1) are given in Figure 1-12. These results were calculated using the hindered rotor approximation for the torsional modes of CH_3O_2 and the transition state (see section 1.8). Redundant curvilinear coordinates were used for the vibrational analysis in CVT calculations (see section 1.9.4).

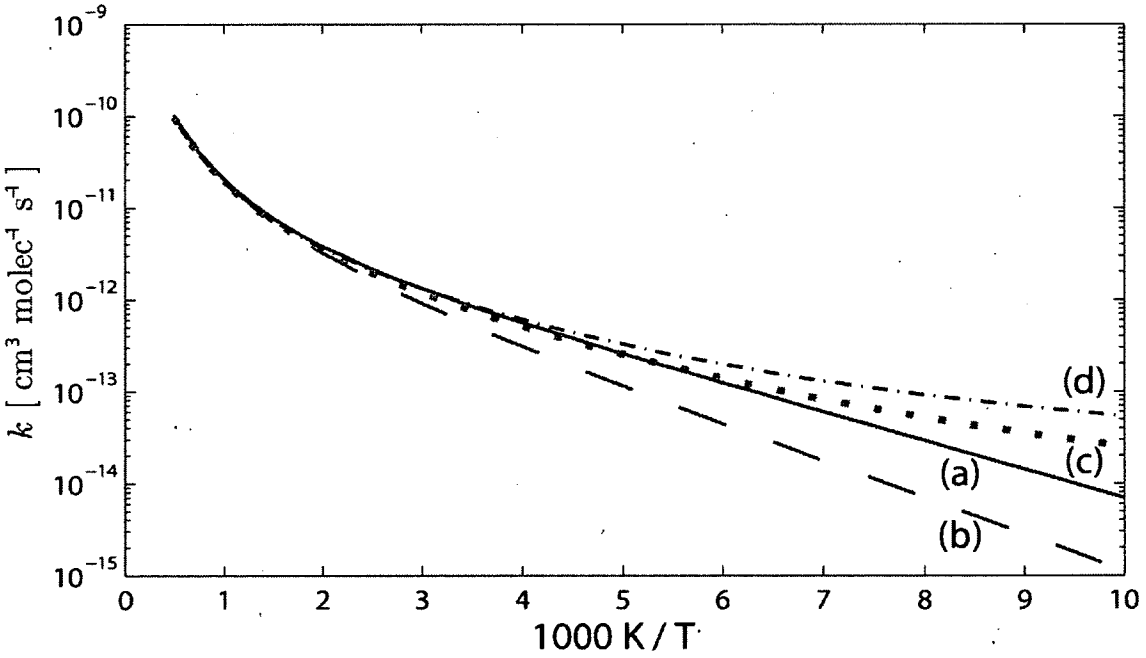

Figure 1-12. $k(T)$ for the direct abstraction channel of the reaction $CH_3O_2 + H \rightarrow {}^1CH_2O_2 + H_2$ calculated using the following TST approximations: **(a)** conventional TST with no tunneling correction, **(b)** CVT with no tunneling correction **(c)** CVT/ZCT, **(d)** CVT/SCT. All calculations were performed using the B3LYP/MG3S DFT approximation. The torsional modes of CH_3O_2 and the transition state were treated using the hindered rotor approximation. The harmonic oscillator model was used for all other vibrational modes. Redundant curvilinear coordinates were used for vibrational analysis in CVT calculations.

Figure 1-12 illustrates that, at temperatures above 650 K (1000 K / T < 1.5), conventional TST with no tunneling correction gives rate constants that coincide with

those calculated using the more sophisticated CVT/SCT approximation. For T < 650 K (1000 K / T > 1.5), however, CVT/SCT is the most appropriate TST approximation for calculating $k(T)$.

Although there are no literature rate constants for reaction (6c) with which to compare our results, they are generally in line with those found for the very similar reactions (17)[111-112] and (18)[114-115].

1.11 Temperature Dependence of the Direct Abstraction Rate Constant

Recall from section 1.2.1 that the Arrhenius relation (equation (13)) is frequently used to model the temperature dependence of rate constants and that it predicts a linear relationship between $\ln(k(T))$ and $1/T$. However, the Arrhenius model is only valid over small temperature ranges. This is demonstrated in Figure 1-12, where the plot of $k^{CVT/SCT}(T)$ is curved over the range 100 K < T < 2000 K.

For this reason, a modified version of the Arrhenius equation[146] is frequently used to model $k(T)$ over large temperature ranges. It is given by

$$k_M(T) = A^*(\frac{T}{300K})^n \exp\left[\frac{-E_M}{RT}\right] \tag{38}$$

Equation (38) is theoretically justified by examining the temperature dependence of the partition function ratios that enter into equations (31) and (32).[118]

We fit both equation (13) and equation (38) to the calculated $k^{CVT/SCT}(T)$ by minimizing the root-mean-square residual ($RMSR$) defined by

$$RMSR = \left\{\frac{1}{39}\sum_{i=1}^{39}\left[\ln\frac{k(T_i)}{k_M(p_1,\ldots,p_N,T_i)}\right]\right\}^{1/2} \tag{39}$$

where k_M is the rate constant predicted by the model, p_1 through p_N are the model parameters, and T_i are 39 temperatures between 100 K and 2000 K equally spaced in $1/T$.

The calculated $k^{CVTSCT}(T)$ rate constant and the fits of equations (13) and (38) are given in Figure 1-12. The best fit parameters and the *RMSR* values for each model are given in Table 1-4.

Table 1-4. The fit parameters using the Arrhenius model and the modified Arrhenius model (A is in cm^3 $molec^{-1}$ s^{-1}, E_M is in kcal/mol)

Model	A	E_M	n	*RMSR*
Arrhenius	1.49×10^{-11}	1.29	-	0.624
Modified Arrhenius	1.15×10^{-12}	0.104	2.39	0.039

Figure 1-13 demonstrates the inadequacy of the Arrhenius model over the full temperature range studied. This is confirmed by noting that, in Table 1-4, the *RMSR* of the Arrhenius model is 16 times that of the modified Arrhenius model. We recommend the modified Arrhenius model with the parameters given in Table 1-4 for the kind of systems used here.

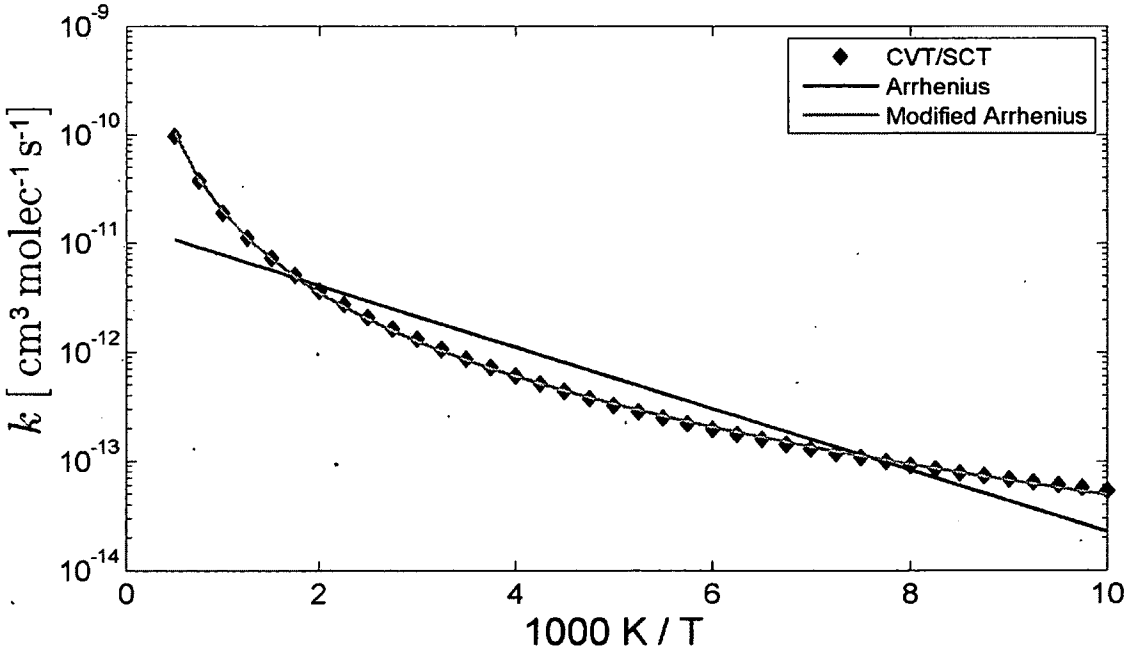

Figure 1-13. $k^{CVT/SCT}(T)$ for the direct abstraction channel of the reaction $CH_3O_2 + H \rightarrow {}^1CH_2O_2 + H_2$ (black diamonds) and best fits using the Arrhenius model (solid black line) and the modified Arrhenius model (solid red line)

The inadequacy of the Arrhenius model is also demonstrated in Table 1-5, which shows how well each model reproduces the activation energy (E_a from equation (14)) calculated using CVT/SCT at different temperatures. The CVT/SCT $E_a(T)$ was calculated using the finite difference method. For the Arrhenius model, $E_a = E_M$ for all T. $E_a(T)$ for the modified Arrhenius model was calculated by substituting equation (38) into equation (14). The Arrhenius model E_a is close to the CVT/SCT $E_a(T)$ only near 250 K. The modified Arrhenius model gives $E_a(T)$ much closer to the CVT/SCT values.

Table 1-5. Activation energy, (E_a, kcal mol^{-1}), at different temperatures calculated using the CVT/SCT approximations and two models fit to these results.

T (K)	CVT/SCT	Arrhenius	Modified Arrhenius
100	0.61	1.29	0.58
250	1.29	1.29	1.29
400	2.12	1.29	2.00
500	2.51	1.29	2.47
800	3.83	1.29	3.90
1000	4.77	1.29	4.85
2000	9.00	1.29	9.59

1.12 Kinetic Isotope Effects (KIEs)

1.12.1 Background

"Substituting one isotope for another at or near an atom at which bonds are being broken or formed typically leads to a change in the rate of the reaction. When the bonds being broken or formed involve those to hydrogen, the effect of replacing H with D is often relatively large and can be measured routinely."[147] Such experiments can provide valuable mechanistic information about complex reactions and provide validation of theoretical methodologies for calculating rate constants. For this reason, we calculated rate constants for three isotopically substituted variants of the direct abstraction channel of reaction (6c):

$$CH_3O_{2\,(g)} + D_{(g)} \rightarrow CH_2O_{2\,(g)} + HD_{(g)} \qquad (6c\text{-}2)$$

$$CH_2DO_{2\,(g)} + H_{(g)} \rightarrow CH_2O_{2\,(g)} + HD_{(g)} \qquad (6c\text{-}3)$$

$$CH_2DO_{2\,(g)} + H_{(g)} \rightarrow CHDO_{2\,(g)} + H_{2\,(g)} \qquad (6c\text{-}4)$$

The influence of isotopic substitution on the rate constant is referred to as the kinetic isotope effect (KIE).[147] KIEs are frequently measured as the ratio of the rate constants for the unsubstituted and substituted reactions (η).

$$\eta = \frac{k_H}{k_D} \qquad (40)$$

If $\eta > 1$, this is referred to as a normal KIE; if $\eta < 1$, it is an inverse KIE.

Extensive work has shown that tunneling must be included in calculations of KIEs for hydrogen transfer reactions and that the choice of tunneling approximation has a big effect on the KIE.[144-145] To test the effect of tunneling on the KIEs for reaction (6c), we calculated all KIEs using the conventional TST (see section 1.7.1), CVT (see section 1.9.1), CVT/ZCT, and CVT/SCT (see section 1.10.1) approximations. These results are referred to below as η^{TST}, η^{CVT}, $\eta^{CVT/ZCT}$, and $\eta^{CVT/SCT}$, respectively.

KIEs for reactions in which a bond to the isotopically substituted atom is partially broken in the transition state are referred to as primary KIEs. KIEs for reactions where the isotopically substituted atom is a spectator on the same carbon as the abstracted H atom are called secondary KIEs.[147] Thus, the KIE for reaction (6c-3) is a primary KIE and that for reaction (6c-4) is a secondary KIE. We will refer to the KIE for reaction (6c-2) as the "H-attack" KIE.

1.12.2 "H-attack" Kinetic Isotope Effect

The logarithms of η^{TST}, η^{CVT}, $\eta^{CVT/ZCT}$, and $\eta^{CVT/SCT}$ for reaction (6c-2) are given in Figure 1-14. (The log scale is used to make the plot easier to read.)

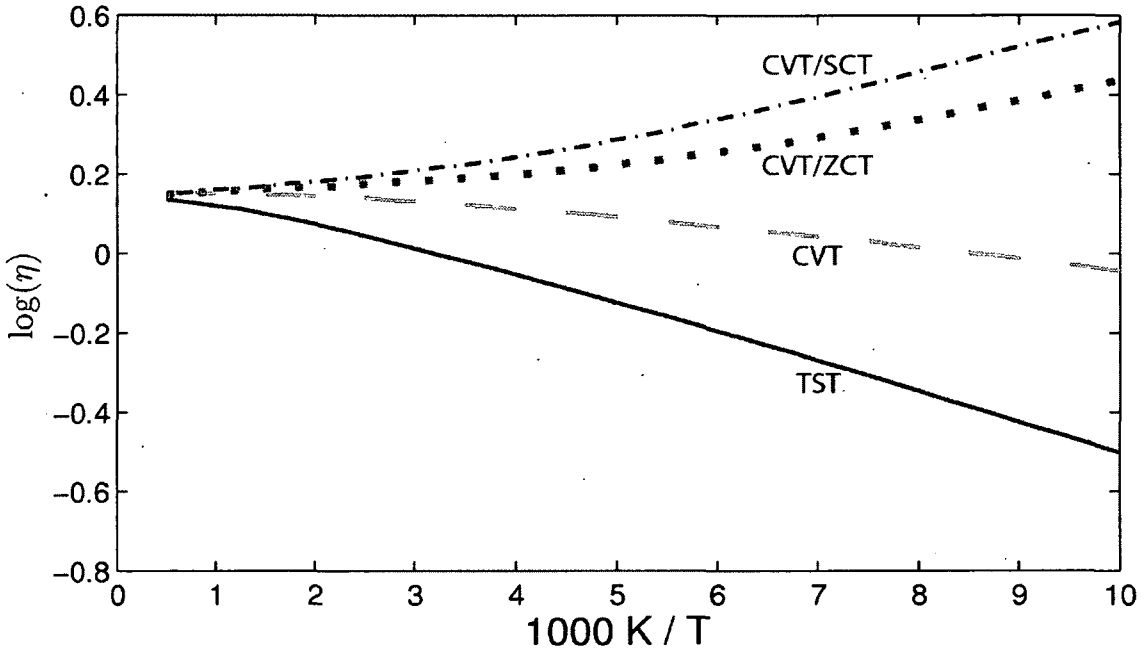

Figure 1-14. $\log(\eta)$ for $CH_3O_2 + X \rightarrow CH_2O_2 + HX$ where X = H, D, calculated with different TST approximations at the B3LYP/MG3S level of theory. ($\eta = k_H / k_D$)

η^{TST} is given by the solid blue line in Figure 1-14 and the last column in Table 1-6. It is inverse ($\eta < 1$) at low temperatures, with η^{TST} (100 K) = 0.31. (T = 100 K corresponds to 1000 K / T = 10). It first increases steeply with temperature, becoming normal ($\eta > 1$) at $T \approx 350$ K (1000 K / $T \approx 2.9$), and then more slowly, reaching η^{TST}(2000 K) = 1.37. (T = 2000 K corresponds to 1000 K / T = 0.5).

To determine the reason for this monotonic increase, we have decomposed η^{TST} into factors due to changes in the translational partition function (η_{trans}), the rotational partition function (η_{rot}), and the vibrational partition function (η_{vib}). (See section 1.7.1 for an explanation of partition functions and how they enter into the TST rate constant).

η_{vib} was further decomposed into terms due to changes in the high frequency vibrational modes ($\nu > 3000$ cm^{-1}), mid-frequency modes (3000 cm^{-1} $< \nu <$ 350

cm^{-1}), and low frequency modes ($\nu < 350\ cm^{-1}$). The details of this factorization are given by Chakraborty, *et al.* (2006).[148]

$$\eta^{TST} = \eta_{trans}\ \eta_{rot}\ \eta_{vib,high}\ \eta_{vib,mid}\ \eta_{vib,low} \tag{41}$$

The results of the factorization are given in Table 1-6. Clearly, the monotonic increase in η^{TST} is due to the mid-frequency vibrational modes. Upon further analysis of the contribution of each vibrational mode to $\eta_{vib,\ mid}$, we found that the main contribution is from the quasi-symmetric C-H(4)-H/D(7) stretching mode.

Table 1-6. TST KIEs and factors for $CH_3O_2 + X \rightarrow CH_2O_2 + HX$ where X = H, D

T (K)	η_{trans}	η_{rot}	$\eta_{vib,\ high}$	$\eta_{vib,\ mid}$	$\eta_{vib,\ low}$	η^{TST}
100	2.74	0.80	1.00	0.23	0.64	0.32
200	2.74	0.80	1.00	0.47	0.74	0.75
250	2.74	0.80	1.00	0.54	0.75	0.88
400	2.74	0.80	1.00	0.66	0.77	1.11
500	2.74	0.80	1.00	0.70	0.77	1.18
8000	2.74	0.80	1.00	0.76	0.78	1.29
1000	2.74	0.80	1.00	0.78	0.78	1.32
2000	2.74	0.80	1.00	0.80	0.78	1.36

The "H attack" CVT/SCT KIE ($\eta^{CVT/SCT}$) is given by the black dot-dash curve in Figure 1-13 and the last column in Table 1-7.

Table 1-7. CVT/SCT KIEs and factors for for $CH_3O_2 + X \rightarrow CH_2O_2 + HX$ where X = H, D

T (K)	η_{trans}	η_{rot}	$\eta_{vib,\ high}$	$\eta_{vib,mid}$	$\eta_{vib,low}$	η_{pot}	η_{tun}	$\eta^{CVT/SCT}$
100	2.74	0.79	1.00	0.88	0.65	0.74	4.21	3.83
200	2.74	0.79	1.00	0.90	0.73	0.88	1.56	1.92
250	2.74	0.79	1.00	0.90	0.73	0.91	1.34	1.72
400	2.74	0.79	1.00	0.91	0.75	0.94	1.12	1.54
500	2.74	0.79	1.00	0.91	0.75	0.95	1.08	1.51
800	2.74	0.79	1.00	0.90	0.75	0.97	1.03	1.46
1000	2.74	0.79	1.00	0.90	0.74	0.97	1.02	1.44
2000	2.74	0.79	1.00	0.92	0.73	0.99	1.00	1.43

Note that there are important differences between $\eta^{CVT/SCT}$ and η^{TST}. For one, unlike η^{TST}, $\eta^{CVT/SCT} > 1$ over the whole temperature range. Also, while η^{TST} increases

monotonically with temperature, $\eta^{CVT/SCT}$ decreases monotonically with temperature from $\eta^{CVT/SCT}(100\ K) = 3.83$ to $\eta^{CVT/SCT}(2000\ K) = 1.43$. ($T$ =100 K corresponds to 1000 K / T = 10 and T = 2000 K corresponds to 1000 K / T = 0.5).

We have performed a factorization similar to equation (41) for the CVT/SCT KIE.[148]

$$\eta^{CVT/SCT} = \eta_{trans}\ \eta_{rot}\ \eta_{vib,high}\ \eta_{vib,mid}\ \eta_{vib,low}\ \eta_{pot}\ \eta_{tun} \qquad (42)$$

η_{pot} is a potential energy contribution that arises because the potential energies of the CVT transition states for the substituted and unsubstituted reaction are different and η_{tun} is the tunneling contribution to the KIE.[148] As seen in Table 1-7, the monotonic decrease in $\eta^{CVT/SCT}$ is mostly due to the tunneling contribution.

We also calculated the isotope effect for reaction (6c-2) using the harmonic oscillator approximation instead of the hindered rotor approximation for the torsional vibrational mode in the transition state and CH_3O_2 (see section 1.8). The $\eta^{CVT/SCT}$ values calculated using the HO approximation are ~15% lower than those calculated using the HR approximation.

It should also be noted from Figure 1-14 that $\eta^{CVT/SCT}$ is somewhat higher than $\eta^{CVT/ZCT}$, confirming the previous findings that the more sophisticated tunneling methods are necessary for proper calculation of kinetic isotope effects.[145]

1.12.3 Primary Kinetic Isotope Effect

The logarithms of η^{TST}, η^{CVT}, $\eta^{CVT/ZCT}$, and $\eta^{CVT/SCT}$ for reaction (6c-3) are given in Figure 1-15. $\eta^{TST}(250\ K) = 4.38$, which is typical for a KIE of this type.[147] (T = 250 K corresponds to 1000 K / T = 4.) η^{TST} decreases monotonically from

η^{TST}(100 K) = 30.21 to η^{TST}(2000 K) = 1.21. (T =100 K corresponds to 1000·K /T = 10 and T = 2000 K corresponds to 1000 K / T = 0.5.)

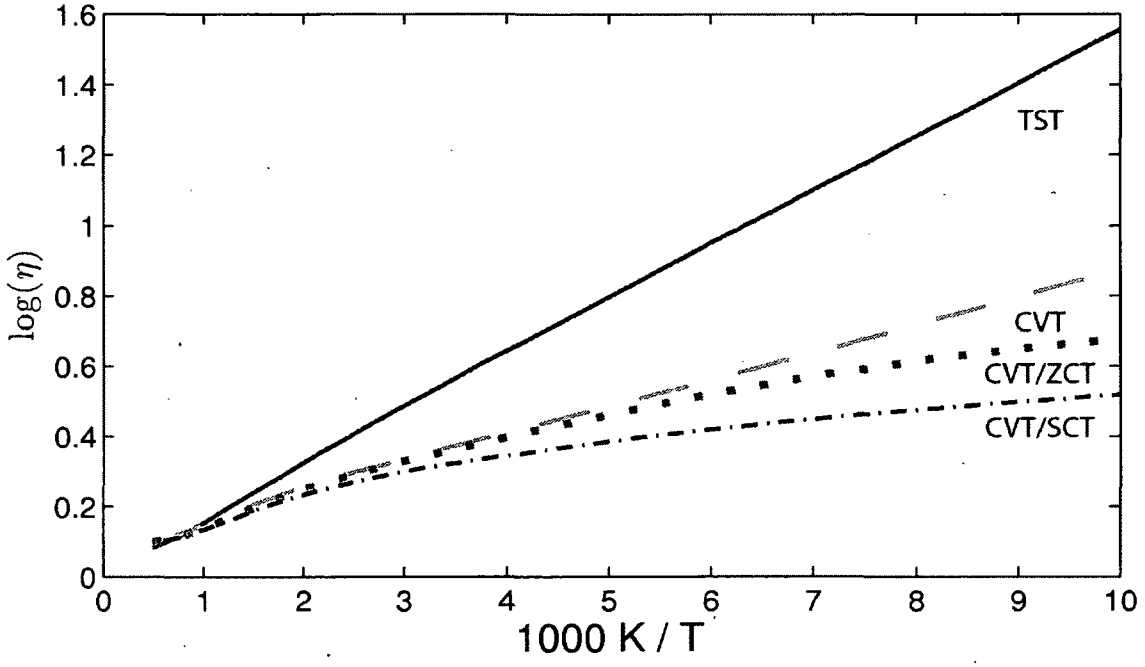

Figure 1-15. log (η) for CH_2XO_2 + H → CH_2O_2 + HX, where X = H, D calculated with different TST approximations at the B3LYP/MG3S level of theory. ($\eta = k_H/k_D$)

Variational placement of the TS combined with tunneling decreases η by a factor of 10 at low temperatures ($\eta^{CVT/SCT}$(100 K) = 3.29), but does not affect it much at high temperatures ($\eta^{CVT/SCT}$(2000 K)= 1.25). (T =100 K corresponds to 1000 K /T = 10 and T = 2000 K corresponds to 1000 K / T = 0.5.)

1.12.4 Secondary Kinetic Isotope Effect

In reaction (6c-4), the H(D) atom is a spectator on the same carbon as the abstracted H atom. η^{TST}, η^{CVT}, $\eta^{CVT/ZCT}$, and $\eta^{CVT/SCT}$ for reaction (6c-4) are given in Figure 1-16. (Note that, in contrast with Figures 1-14 and 1-15, the y-axis is not logarithmic in Figure 1-16). There is a slight normal KIE (see section 1.12.1) at

$T < 1000$ K (1000 K/ $T > 1$). This is the expected result for this type of KIE.[147] Tunneling seems to slightly enhance the KIE at low temperatures.

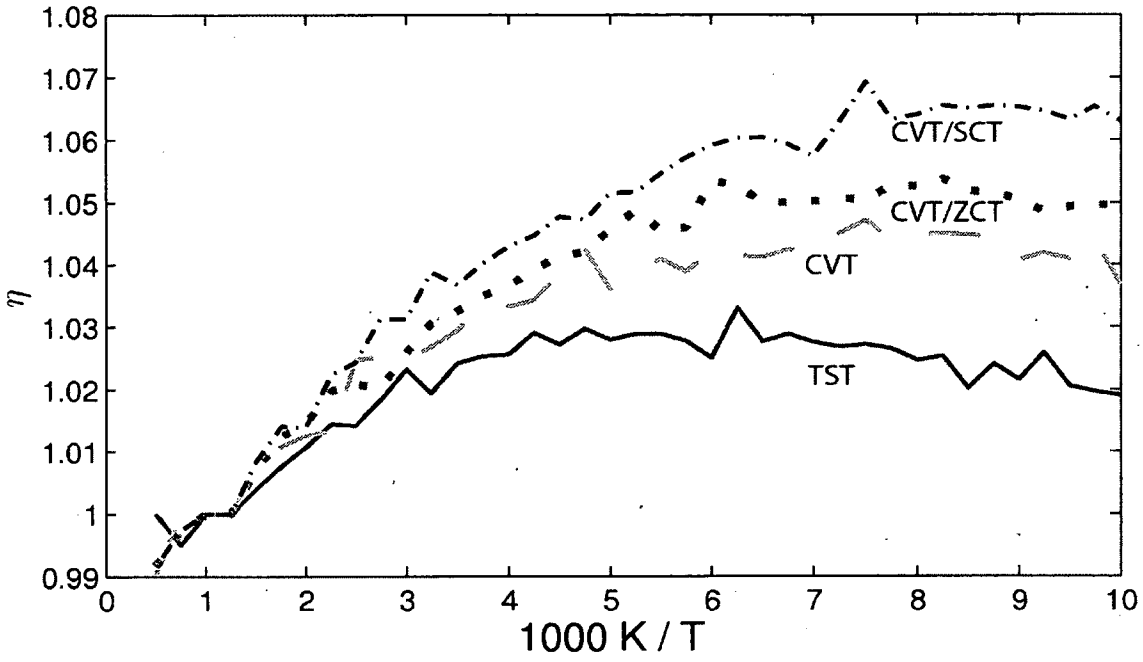

Figure 1-16. The KIE for $CH_2XO_2 + H \rightarrow CHXO_2 + H_2$ where X = H, D calculated with different TST approximations at the B3LYP/MG3S level of theory. ($\eta = k_H/k_D$)

1.13 Basis Set Effects

We also investigated the effect of basis set size on the rate constant and isotope effects for the direct abstraction channel of (6c) using CVT/SCT. To save time, the coarser "fine" DFT integration grid was used with basis sets smaller than MG3S.

Figure 1-16 shows the Arrhenius plot calculated using CVT/SCT and the B3LYP density functional with different basis sets. In general, larger basis sets lead to larger rate constants. The 6-31++G(d) rate constant is very different from the 6-31G(d) and 6-31++G(d,p) results, which suggests that using diffuse functions without H polarization functions leads to unconverged rate constants.

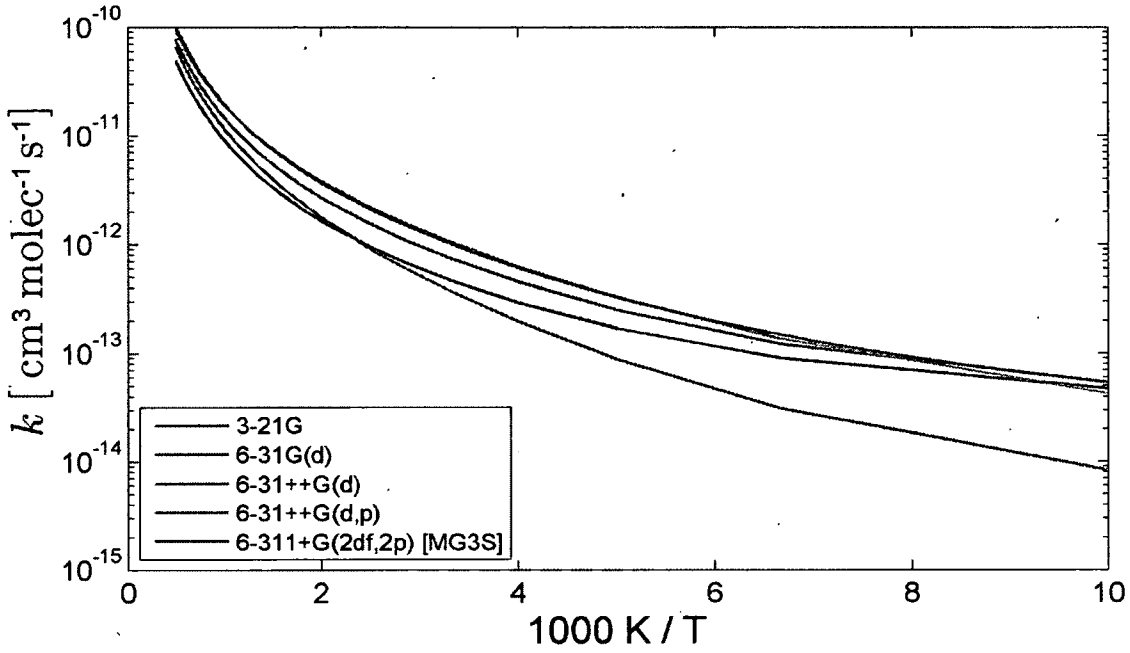

Figure 1-17. Arrhenius plot for the direct abstraction channel of (6c) calculated by the CVT/SCT TST approximation using B3LYP with different basis sets.

Figure 1-18 shows the logarithm of the isotope effect for reaction (6c-2) calculated using CVT/SCT and the B3LYP density functional with different basis sets. $\eta^{CVT/SCT}$ increases as the size of the basis set is increased from 3-21G to 6-31++G(d), then decreases on going from 6-31++G(d) to 6-31++G(d,p), and then increases slightly on going from 6-31++G(d,p) to MG3S. Surprisingly, $\eta^{CVT/SCT}$ calculated with the very small 3-21G basis is close to that calculated with the much larger MG3S basis set, especially on the range 140 K < T < 200 K.

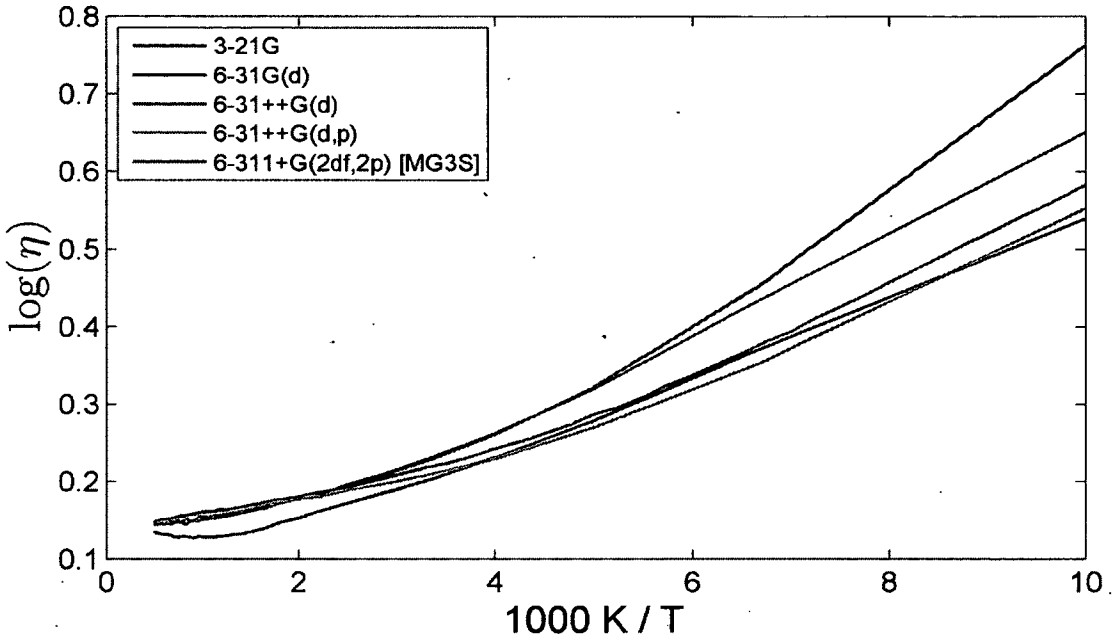

Figure 1-18. log(η) for $CH_3O_2 + X \rightarrow CH_2O_2 + HX$ where X = H, D, calculated by CVT/SCT using B3LYP with different basis sets. ($\eta = k_H/k_D$)

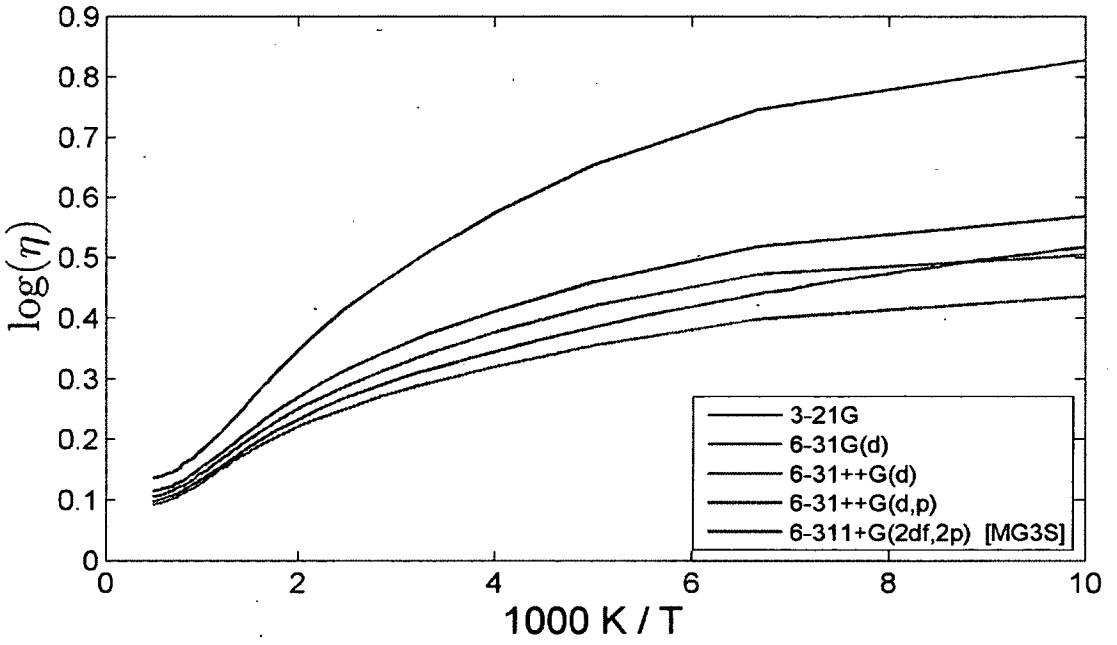

Figure 1-19. log(η) for $CH_2XO_2 + H \rightarrow CH_2O_2 + HX$, where X = H, D calculated by CVT/SCT using B3LYP with different basis sets. ($\eta = k_H/k_D$)

Figure 1-19 shows the logarithm of the isotope effect for reaction (6c-3) calculated using CVT/SCT and the B3LYP density functional with different basis sets. $\eta^{CVT/SCT}$ decreases as the size of the basis set is increased from 3-21G to 6-31++G(d,p) and then increases on going from 6-31++G(d,p) to MG3S.

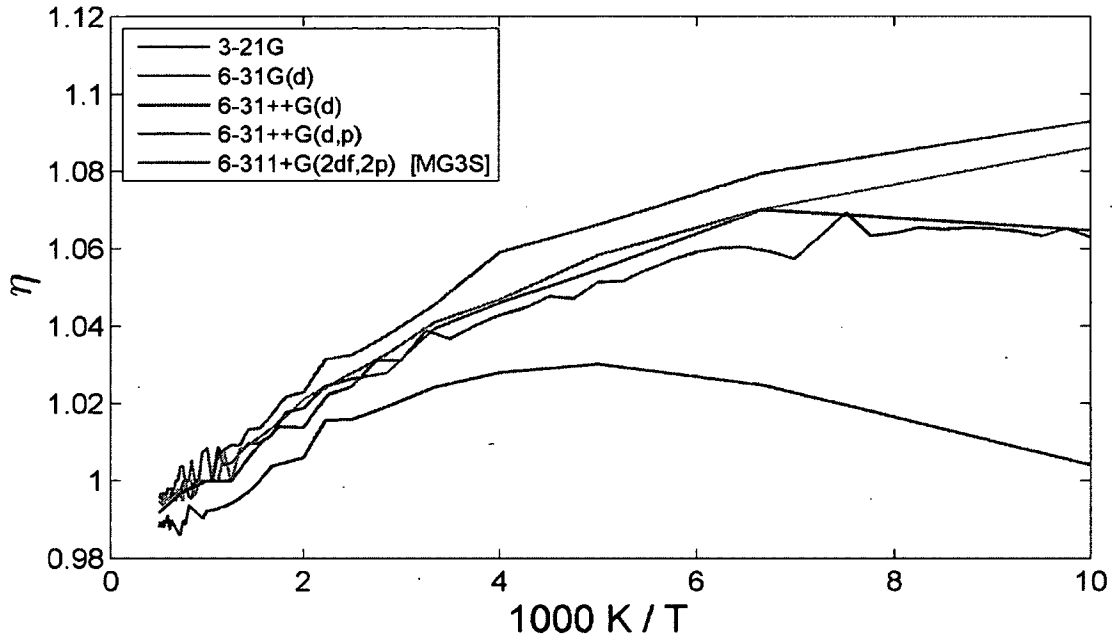

Figure 1-20. η for $CH_2XO_2 + H \rightarrow CHXO_2 + H_2$ where X = H, D, calculated by CVT/SCT using B3LYP with different basis sets. ($\eta = k_H/k_D$)

Figure 1-20 shows the isotope effect for reaction (6c-4) calculated using CVT/SCT and the B3LYP density functional with different basis sets.

For T < ~ 100K, $\eta^{CVT/SCT}$ increases as the size of the basis set is increased from 3-21G to 6-31++G(d), then decreases on going from 6-31++G(d) to 6-31++G(d,p), and then decreases again on going from 6-31++G(d,p) to MG3S. In this case, the smaller 6-31G(d) basis set gives results similar to the large MG3S basis.

1.14 Summary and Conclusions

We have carried out CCSD(T), DFT, and direct dynamics based VTST/MT calculations using the GAUSSIAN and POLYRATE software packages to find the rate constant and isotope effects for the direct abstraction channel of reaction (6c) on the temperature range 100 - 2000 K. To the best of our knowledge, this is the first study of this reaction. This reaction may be important in combustion chemistry and is the prototype system for several other interesting reactions.

We found that, on the B3LYP, M06-L, ωB97X-D, MPW1K, and BB1K PESs, reaction (6c) proceeds through both a direct abstraction and an addition-elimination pathway. On the M05, M05-2X, M06, M06-2X, and BMK PESs, only the addition-elimination pathway was found. Based on previous work with similar reactions, we concluded that both pathways are important. Our further analysis was focused on the direct abstraction channel.

We performed benchmark calculations using the CCSD(T)/maug-cc-pVTZ//B3LYP/MG3S method and used them to choose a DFT model chemistry for VTST/MT calculations. B3LYP/MG3S was found to be the best choice.

We tested both the hindered rotor and harmonic oscillator approximations for the lowest frequency vibrational mode in CH_3O_2 and the transition state and found that the harmonic oscillator approximation is not appropriate. We found that conventional TST gives incorrect results for the rate constant and isotope effects, and that VTST in combination with small curvature tunneling (CVT/SCT) is necessary for accuracy. We found that isotope effects are particularly sensitive to the choice of tunneling method. Our best estimate for the rate constant is 8.27×10^{-12} cm^3 molec^{-1} s^{-1} at 300 K. To obtain

a simple relation for the temperature dependence of the rate constant, a modified form of the Arrhenius model was fit to the CVT/SCT rate constant. Our recommended equation is

$$k(T) = 1.15 \times 10^{-12} \left(\frac{T}{300K}\right)^{2.39} \exp\left[\frac{-0.104 \text{ kcal mol}^{-1}}{RT}\right] \text{ cm}^3 \text{ molec}^{-1} \text{ s}^{-1} \qquad (43)$$

The recommended next step in this work is a similar characterization of the addition-elimination channel. This analysis is complicated by the presence of a barrierless association step, but a methodology of treating such reactions using TST has been developed within the last 10 years[149] and is available in POLYRATE. We also recommend that reactions (6a) and (6b) be treated using the methods presented here as soon as possible, due to their potential importance in tropospheric chemistry.

CHAPTER 2

DENSITY FUNCTIONAL STUDY OF THE DIBENZOFURAN + CHLORINE REACTION

2.1 Introduction

Polychlorinated dibenzo-p-dioxins (PCDDs) and dibenzofurans (PCDFs) are extremely toxic compounds,[150-152] formed during industrial production of other chemicals, waste incineration, iron and steel production, and paper manufacturing. They have been measured in the atmosphere worldwide.[153-155] A relatively recent incarnation of this problem is the discovery of very high PCDD/F levels near an electronics disposal site in China.[156]

The structures of an example of a PCDF, 2,3,7,8-tetrachlorinated dibenzofuran (TCDF), and the parent compound, dibenzofuran (DBF), are given in Figure 2-1.

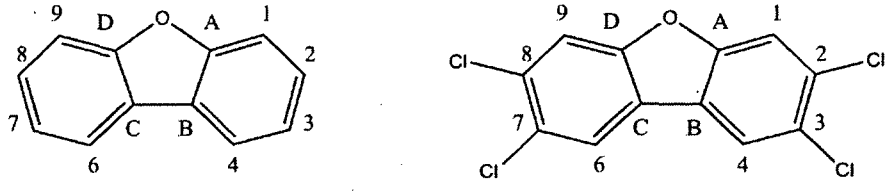

Figure 2-1. (a) dibenzofuran (DBF) (b) 2,3,7,8-tetrachlorinated dibenzofuran (TCDF)

Atkinson (1991) proposed that PCDD/PCDF degradation in the atmosphere proceeds mainly by reaction with the hydroxyl radical (OH), based on structure additivity relations (SARs).[157] Since then, OH oxidation has been assumed to be essentially the only chemical loss process when analyzing sources and sinks of PCDF.[155, 158-159] At the time of this analysis, chlorine was not thought to be a significant atmospheric oxidant.

This conventional wisdom is being rethought, but to our knowledge, there are no experimental or theoretical studies of PCDF reactions with Cl.

As a step in the direction of detailed analysis of PCDF reactions with Cl, we have performed a computational study of the reaction of dibenzofuran with chlorine using the MPW1K density functional.[107] DFT is the approach of choice, because high level wave function theory (WFT) methods are too time intensive for a system of this size.

There are few experimental gas phase rate constants for PCDD/PCDF reactions, because the low vapor pressure of these compounds makes them difficult to study in the gas phase. Kwok *et al.* (1994) measured the rate constant for the reaction of dibenzo-p-dioxin and dibenzofuran with OH.[160] Kwok *et al.* (1995) measured the rate constant for OH + 1-chlorodibenzo-p-dioxin.[161] Brubaker and Hites (1997) determined the rate constant for 1,2,3,4-tetrachloro-dibenzo-p-dioxin + OH.[162] Brubaker and Hites (1998) measured the OH + dibenzo-p-dioxin, 2,7-dichlorodibenzo-p-dioxin, dibenzofuran, and 2,8-dichlorodibenzofuran rate constants.[163] Taylor et al. (2005) measured the rate constants for OH reaction with several dibenzo-p-dioxins with 1, 2, 4, and 8 chlorine substituents.[164]

Looking at the problem as one of combustion, in her Ph. D. dissertation, Sebbar (2006) explored in detail the thermochemistry and decomposition mechanism of the dibenzofuranyl radical+ O_2 system using the B3LYP density functional and validated the accuracy of DFT for this system by comparison to a high accuracy WFT composite method applied to smaller systems.[165]

Altawaraneh *et al.* (2006) also used B3LYP in a study of the decomposition pathways of DBF in a combustion context.[166] In this paper, DBF is initially oxidized by

O_2. They find that hydrogen abstraction is slightly more likely to occur at C_4. The resulting DBF· radical reacts with O_2 to either form DBF-O_2· at low temperature, or DBF-O· at high temperature. The unimolecular decomposition of both is then followed. They found four pathways. The first goes through conversion of one of the benzene rings in DBF-O· to a five-membered ring and in the end produces CO, ethyne and 1-ethylphenyl. The second involves intermolecular O transfer in DBF-O_2·, followed by ring opening and intermolecular H transfer and ends in benzofuran and CO. The third pathway proceeds through a hydroxyquinone-dibenzofuran structure and also ends in benzofuran + CO. The most favorable of their four pathways has DBF-O_2· form a three-membered COO ring and then joins the first path.

Recognizing that dibenzofuran chemistry has important atmospheric implications, Altawaraneh *et al.* then repeated their B3LYP calculations for the DBF + OH system (2008).[167] They found a DBF lifetime of 0.44 days and that the reaction proceeds predominantly (~90%) by addition to form DBF-OH·, rather than by H abstraction. Addition occurs preferentially at C4. Ring opening after OH addition at C_A or C_B (see Figure 2-1) was deemed to be unfavorable in atmospheric conditions. Then the mechanism for O_2 mediated decomposition is discussed, using the example of the DBF-OH adduct with OH at C4. O_2 can add at both the ortho and the para positions and *cis* or *trans* to the OH, for a total of 6 isomers. O_2 addition at C_1 and C_3 is preferred to C_B. O_2 can also abstract H from the hydroxyl group, which results in an epoxide, or the H from C_4, which results in dibenzofuranol. Dibenzofuranol formation is preferred to DBF-OH-O_2 or epoxide formation.

Sun *et al.* (2012) characterized the TCDF + OH + O_2 PES using the MPWB1K functional and calculated the rate constants for TCDF + OH and TCDF-OH + O_2 using POLYRATE.[168] OH addition was found to be thermodynamically favorable and to occur with a barrier, which is smallest at C_4. They found that addition occurs predominantly at C_4, in agreement with the DBF results of Altawaraneh *et al.* (2008), with C_1 and C_A becoming more important at higher temperatures. H abstraction at C_1 and C_9 was found to have a higher barrier and to be endothermic or only slightly exothermic. It was decided to be negligible. With their calculated rate constants, the authors get an atmospheric lifetime of 12.2 days for TCDF, consistent with previous results based on Atkinson's SAR estimates. If OH addition occurs at C_A, the next step is either opening of the furan ring, or addition of O_2 at either one of the two ortho positions or the para position. O_2 can add *cis* or *trans* to OH. The authors conclude that ring opening is preferred. If OH adds to C_B, then the situation is reversed, and ring opening is more likely. If OH adds at C_1, the authors conclude that there is competition between O_2 addition and abstraction of the ipso H of TCDF-OH to yield dibenzofuranol. If OH adds at C_4, dibenzofuranol is formed exclusively. OH addition at C_2 and C_3 leads to dibenzofuranol through Cl abstraction at the ipso carbon. Lastly, the authors claim that the third and fourth steps in the atmospheric degradation of TCDF are reactions of the TCDF-OH-O_2· adduct with NO_2 and H_2O to form a dibenzofuran-di-ol.

The same group of authors (Zhang *et al.* 2012) elaborated on the mechanism of TCDF-OH-O_2 decomposition using the same DFT and VTST methodologies.[169] They chose to follow the fate of the TCDF-OH adduct with the OH at C_A. They found that OH can add with three different orientations. Then they chose a continuation in which O_2

adds to C_B. O_2 adds *cis* or *trans* to the OH. For the *cis* addition, they found that O_2 can add in three different orientations, leading to three degradation mechanisms. If O_2 adds facing away from the ring, there follows a rearrangement that puts C_1 into the furan ring instead of C_B, followed by C-O and C-C bond cleavage, yielding a hydroxy-phenyldioxy radical and a five-membered ring ketene. If O_2 hangs over the five-membered ring after addition, the second O atom will add to C_D, starting a pathway that leads to a cyclohexadiene-dione. If O_2 hangs over the six-membered ring, it will add across that ring to C_2. That pathway ends in a cyclohexadienone and an epoxide. The second route has the lowest barrier. If O_2 adds *trans* to OH, two conformers are possible: O_2 facing away from the rings or O_2 hanging over the five-membered ring. In the first case, there are two possible pathways. In the first pathway, the C-C and C-O bonds cleave, yielding hydroxy-phenyldioxy and cyclohexadienone. In the second pathway of the first case, O_2 turns toward the five-membered ring and adds to C_D. Going through a three-membered C_D-O-C_9 ring, this path ends in 2-3-dichloro-pentanedial and hydroxy-cyclohexadienone. If the O_2 adds hanging over the six-membered ring, the mechanism goes through addition of the second O atom to C_2 and proceeds through the formation of a dioxin, which is degraded by another OH addition. The authors state that just as in reference 168, they state that TCDF-OH-O_2 + NO is important, but in this paper, the suggested products of this scheme are a cyclohexadienone and a hydroxy-cyclohexadienone. Also, the authors find the transition states for reaction of the intermediates in their scheme with H_2O, yielding dibenzofuran-diols. The rate constants for all steps are computed using VTST and the lifetimes of the intermediates are compared. The lifetime of the TCDF-OH adduct against reaction with O_2 is calculated to be 6 minutes.

Although there are no studies of PCDF/DBF + Cl, the reaction of Cl with furan and some derivatives has been examined. Cabanas *et al.* (2005) measured rate constants for Cl + furan, 2-methylfuran, 3-methylfuran, 2- ethylfuran, and 2,5-dimethylfuran.[170]

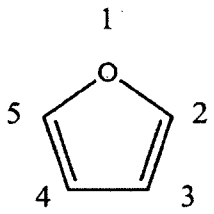

Figure 2.2 Furan

Based on the measured rate constants (which are ~10x greater than those for OH), they concluded that removal by Cl may be competitive with removal by OH (13.6 hour lifetime for Cl removal at dawn in the marine boundary layer, versus 6.8 hours for OH).

Villanueva *et al.* (2007) performed product studies for the furan reaction.[171] They concluded that reaction proceeds primarily by Cl addition, with H abstraction being a minor pathway. The proposed mechanism is: addition of Cl to an ortho carbon (C_2 or C_5), followed by O_2 addition at the other ortho carbon to yield the peroxy radical, reaction with another peroxy radical to give the alkoxy, then H abstraction by O_2 to give the chlorofuranone. The alternative is ring opening, yielding a straight chain radical, then O_2 addition *gem* to Cl, then reaction with another peroxy radical and Cl elimination to give butenedial. Villanueva *et al.* (2009)[172] did product studies for the other compounds from Cabanas *et al.* and suggested that these reactions might be viewed as models for PCDF + Cl, which is also difficult to study experimentally. They conclude the reaction proceeds via essentially the same mechanisms, though complicated by the presence of the substituents.

The furan + Cl reaction in the presence of O_2 and CH_3O_2 was studied computationally by Zhang and Du (2011).[173]

Just as in the case of OH, the reaction of PCDF and DBF with Cl is likely to have addition and abstraction pathways. However, the addition of Cl to aromatics is more complex than OH addition. OH only adds to make a σ complex (Figure 2-3a), but since the classic work of Russell and Brown[174] on the reactivity of Cl atoms in a benzene solvent, it has been suspected that Cl can also add in a π fashion. The exact nature of the bonding (η_1-σ, η_1–π or η_6–π (see Figure (2-3b)-(2-3d)) has been a matter of debate.

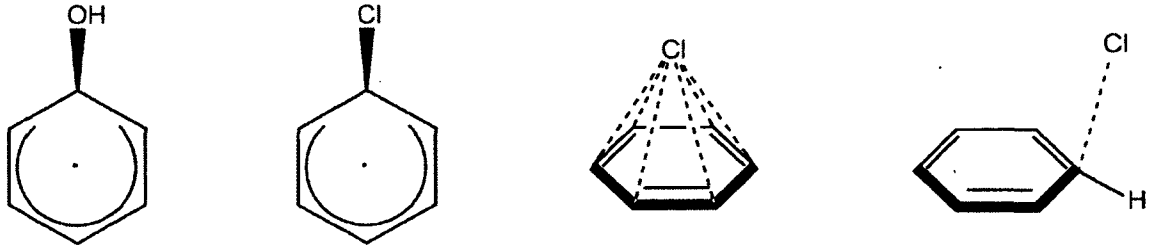

Figure 2-3. (a) hydroxycyclohexadienyl (η_1-σ) (b) chlorocyclohexadienyl (η_1-σ) (c) Cl-benzene η_6-π complex (d) Cl-benzene η_1-π complex

A computational study by Tsao *et al.* (2004)[175] examined the PES of the Cl + benzene system using DFT (B3LYP and BH&HLYP) geometries, with energies computed using DFT and correlated WFT methods. Using the BH&HLYP functional, they found minima corresponding to the η_1-σ (Figure 2-3b) and η_1-π (Figure 2-3d) structures and concluded that the η_1-π complex is the global minimum. The η_6-π (Figure 2-3c) structure was found to be a second order saddle point. The authors found that, because the wavefunctions for these complexes have multi-reference character, spin contamination affects the single-reference correlated WFT methods. DFT is better than traditional wavefunction techniques at handling systems with multi-reference character, making it particularly applicable to this problem.[73] When single point energies were computed using a multi-reference wavefunction method (CASPT2), η_1-π also had the lowest energy, confirming the DFT results. A very important result from this paper is

that the η_1-σ-complex (Figure 2-3b) is not a stationary point on the B3LYP PES, but is a stationary point on the CASPT2 PES. It seems that B3LYP does not capture an essential feature of this PES and that B3LYP is not appropriate for treating the complexation of Cl with aromatics.

This was confirmed by Croft and Howard-Jones (2007).[176] They pointed out that standard density functionals, such as B3LYP, do not include long range electron correlation and frequently give unreliable results for weakly-bound systems, such as (2-3 b) and (2-3 d).[73, 90] They assessed the applicability to this problem of additional functionals with better treatment of non-covalent interactions by testing them against high accuracy composite WFT methods (corrected for the spin contamination problem). They also compared the theoretical predictions to experimental estimates of the stability of the benzene-Cl complex, whatever its bonding may actually be. The functionals they tested are B3LYP, BH&HLYP, B3PW91, PBEPBE, PBE1PBE, MPWB1K, MPW1K. They found an η_1-π complex for all functionals, with a C-Cl bond distance of 2.3 – 2.6 Å. In addition η_1-σ complexes with C-Cl bond lengths between 1.85 and 1.93 Å were identified with the BH&HLYP, PBE1PBE and the MPW functionals. BH&HLYP was found to underestimate the stability of the complex; PBEPBE and PBE1PBE were found to overstabilize it. B3PW91 was also deemed unsatisfactory.

The MPW1K and MPWB1K functionals were specifically parameterized by Truhlar's group to reproduce non-covalent interactions. MPW1K has also been shown to be particularly useful for radical thermochemistry. In the end, Croft and Howard-Jones (2007)[176] chose MPW1K as the density functional of choice for the benzene-Cl system, because it captures both the η_1-σ and η_1-π stationary points and gives them stabilities in

line with expensive WFT results. The stability of the benzene-Cl complexes predicted using MPW1K also matches experimental estimates. In a subsequent study Croft *et al.* (2011)[177] compared MPW1K against several functionals with special corrections for non-covalent interactions, using the example of Cl complexes of benzene and other aromatic compounds. MPW1K again gave the best energies.

One particularly important point is that for MPW1K, the σ complex is lower in energy than the π complex. These energetics are opposite to the conclusion of Tsao *et al.* (2004),[175] but match the relative stabilities predicted by Croft and co-workers' benchmark methods. Croft and coworkers concluded that in a correct treatment, the σ complex should come out more stable. Since DBF and TCDF contain aromatic ring systems, we also chose to use MPW1K for treating the DBF + Cl and TCDF + Cl reactions.

2.2 Computational Methodology

All calculations were performed using the Gaussian 03 suite of programs.[92] Optimized geometries were calculated at the MPW1K/6-31+G(d,p) level of theory.[107] Stationary points were confirmed by vibrational analysis. Structures with no negative Hessian eigenvalues are minima; structures with one negative Hessian eigenvalue are saddle points. Single point energies at the MPW1K/6-31+G(d,p) geometries were computed using MPW1K/6-311++G(3df,3pd). All calculations were performed using the "ultrafine" integration grid. The connection of representative saddle points on the PES to the proper reactants and products was checked using intrinsic reaction coordinate calculations.

2.3 Results and Discussion

Two pathways were explored for the initial reaction between DBF and Cl: Cl addition to the aromatic rings (Scheme 1) and H abstraction (Scheme 2). The energies of the stationary points for reaction at each carbon are given in Figures (2-4)-(2-9). The geometries of the stationary points are given in Figure 2-10.

In line with the benzene-Cl results of Tsao *et al.*[175] and Croft *et al.*,[176-177] both σ and π complexes were found for the addition reaction. At C_A and C_1-C_3, both π complexes (PIC A, PIC 1 – PIC 3) and σ complexes (SIC A, SIC1-SIC3) were identified, as well as saddle points connecting the two (TS A, TS 1-1, TS 2-1, TS 3-1). At C_4, only a σ complex (SIC 4) was identified. At CB, only a π complex (PIC B) was found. All complexes are energetically favored over the separated reactants. The C-Cl bond lengths of the σ complexes, the π complexes, and the saddle points are given in Table 2-1. They, and other geometrical parameters, match those found by Croft *et al.* for the corresponding benzene-Cl structures.[176]

At C_A, the π complex is 1 kcal/mol more stable than the σ complex. At C_1 and C_2, the σ complex is ~3 kcal/mol lower than the π complex. At C_3, the σ complex is more stable by 0.4 kcal/mol. These results mostly match Croft *et al.*'s conclusion that σ-complexes are energetically preferred to π complexes. TS 2-1 is lower in energy than PIC 2, because the single point energies are evaluated using the large basis set at equilibrium geometries calculated with the smaller basis set.

Table 2-1. C-Cl Bond lengths (Å) in the σ and π complexes, and the interconnecting saddle points

Carbon	π complex	saddle point	σ complex
A	2.62	2.09	1.94
1	2.42	2.23	1.87
2	2.40	2.26	1.88
3	2.46	2.08	1.93
4	not found	not found	1.86
B	2.66	not found	not found

The most stable DBF+Cl addition product is the σ complex formed at C_4 (SIC 4), which is 14.0 kcal/mol below the reactants. This matches the results of Altawaraneh *et al.* (2008)[167] for DBF + OH and Sun *et al.* (2012)[168] for TCDF + OH, who found that the hydroxyl radical adds preferentially to C_4. It is also in line with the results of Croft et al. (2007), who found that the benzene-Cl σ complex is stabilized by 10.3 kcal/mol when the MPW1K functional is used.[176] Addition to C_1 and C_2 is slightly less favorable, as the σ complexes at those carbons (SIC 1 and SIC 2) are 12.3 kcal/mol and 11.5 kcal/mol below the reactants, respectively. Then comes addition at C_3, with its σ complex (SIC 3) 9.6 kcal/mol below the reactants. The π complexes at C_A and C_B, both stabilized by about 6 kcal/mol, are the least favorable for addition.

The transition states for H abstraction from C_1-C_4 (TS 1-2, TS 2-2, TS 3-2, and TS 4) were also located, as well the corresponding dibenzofuranyl radicals (IM 1 – IM 4) and the van der Waals complexes between IM 1 – IM 4 and HCl. In another analogy with the DBF + OH[167] and TCDF + OH[168], these abstractions were found to be exothermic and to proceed with a barrier of 10-13 kcal/mol and are likely negligible at atmospheric conditions.

The future directions to be taken in this work are:

1) Calculate the enthalpies and free energies for all reactions described above

2) Repeat these calculations for DBF and various PCDFs

3) Calculate the barriers for addition of O_2 to the DBF-Cl and PCDF-Cl complexes

4) Explore the further fate of DBF-Cl-O_2 and PCDF-Cl-O_2

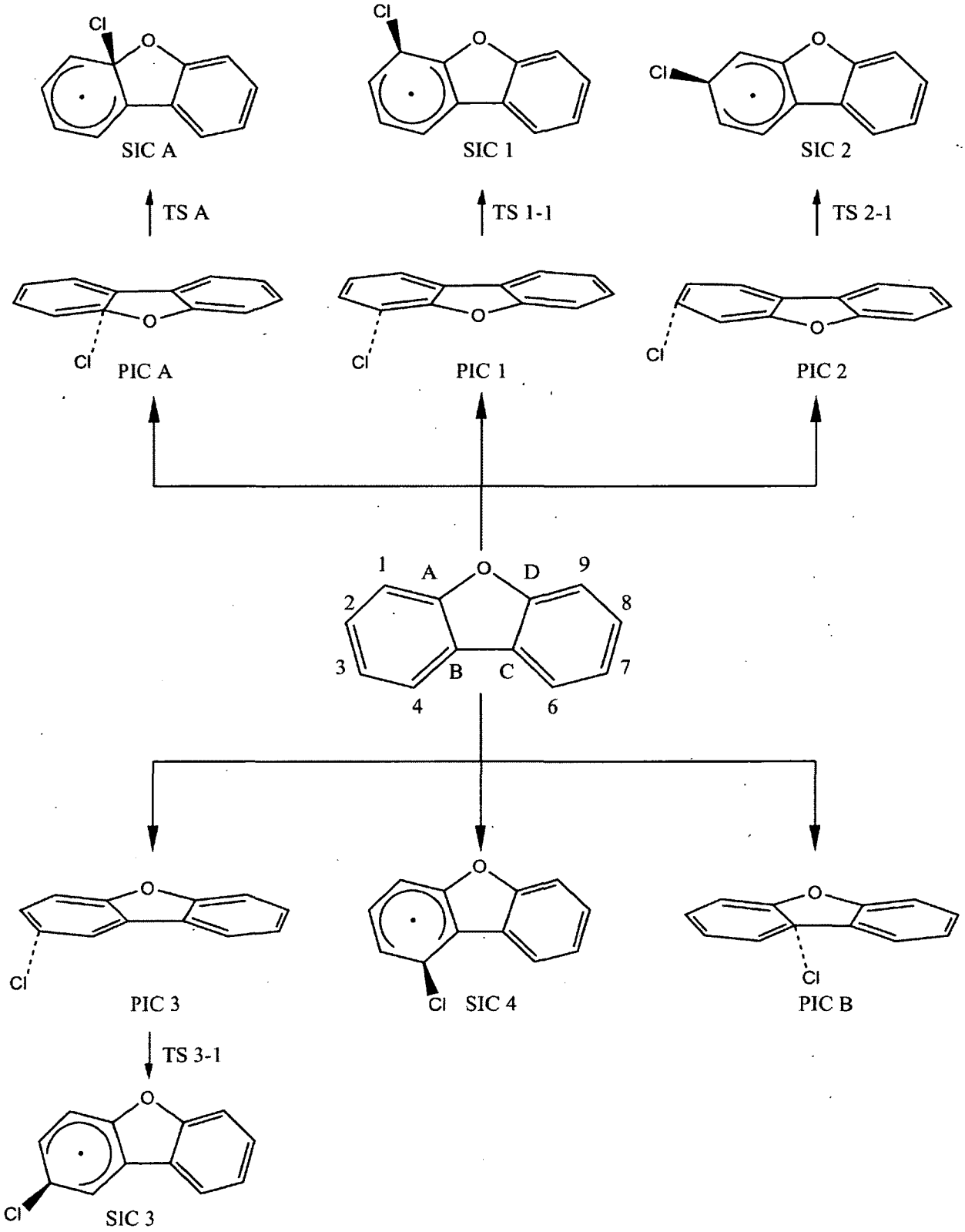

Scheme 1. The reaction scheme for Cl addition to dibenzofuran (DBF).

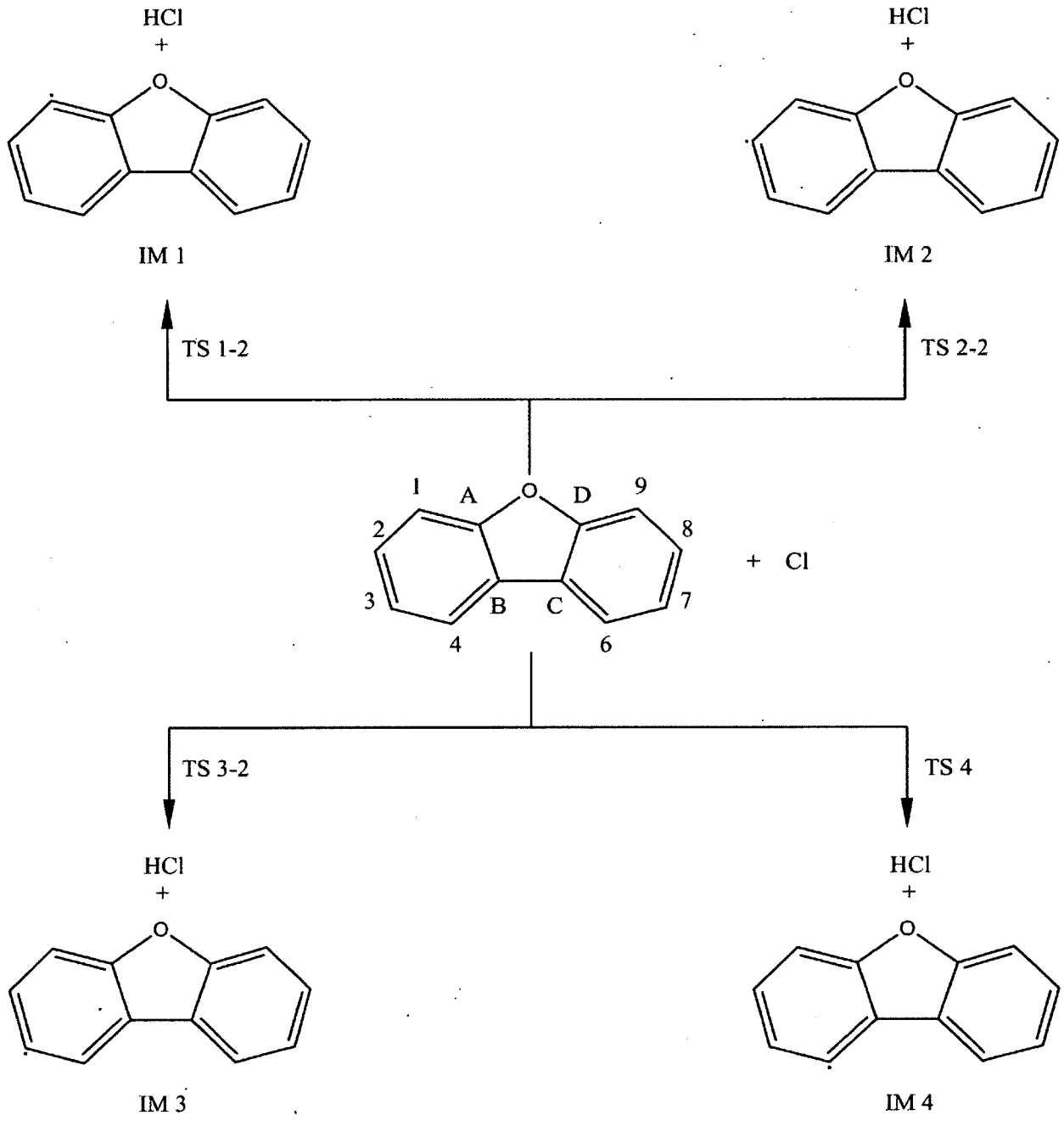

Scheme 2. Reaction scheme for H atom abstraction by Cl from DBF`

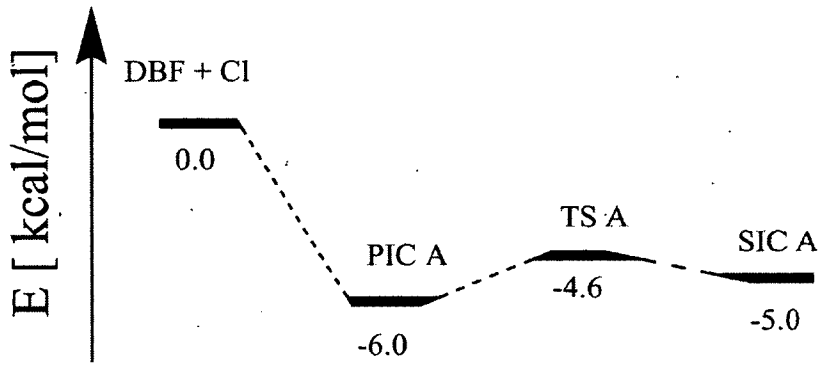

Figure 2-4. PES for Cl attack on DBF at carbon A

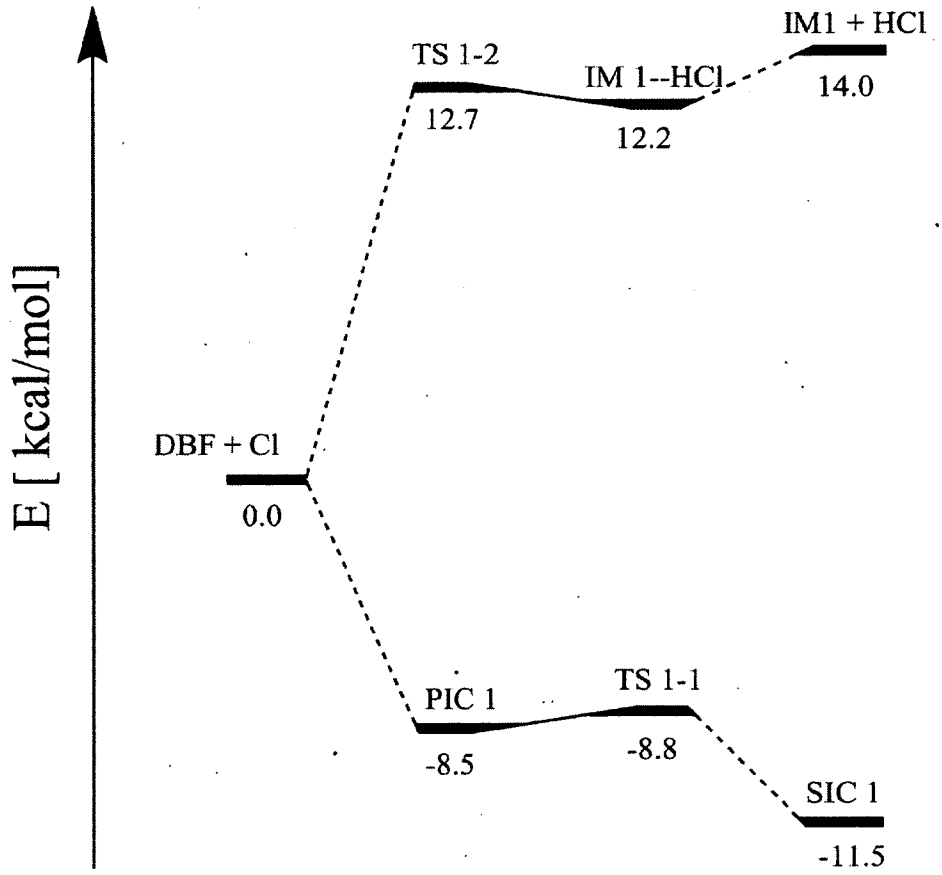

Figure 2-5. PES for Cl attack on DBF at carbon 1

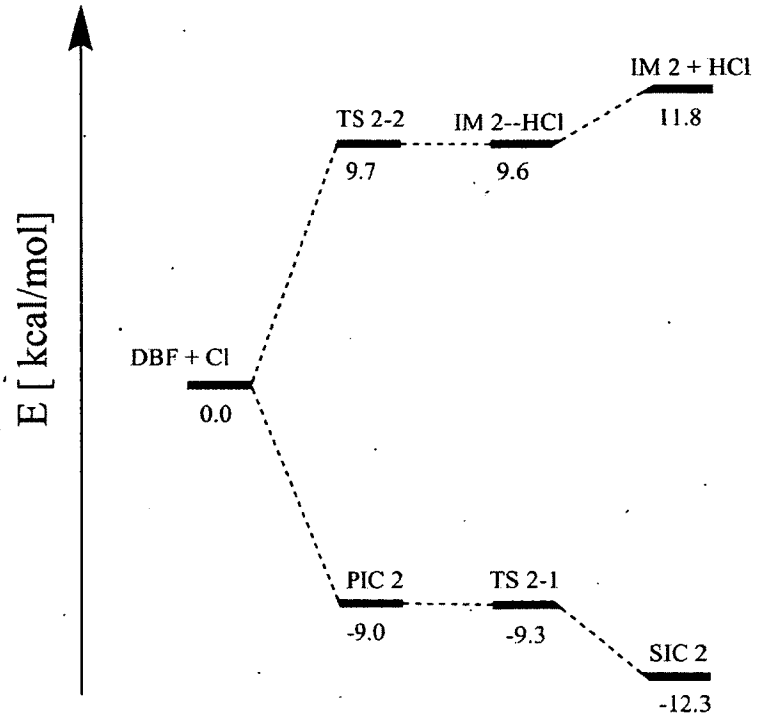

Figure 2-6. PES for Cl attack on DBF at carbon 2

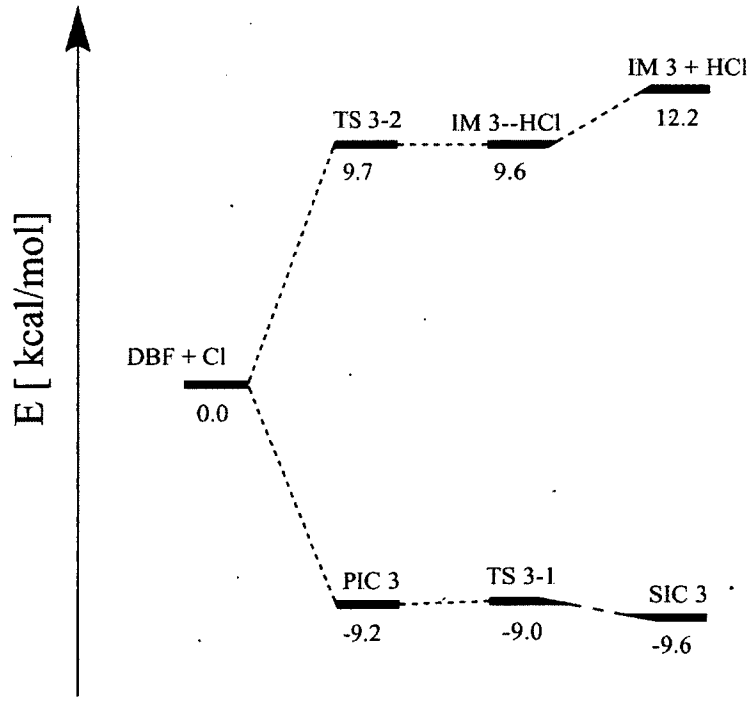

Figure 2-7. PES for Cl attack on DBF at carbon 3

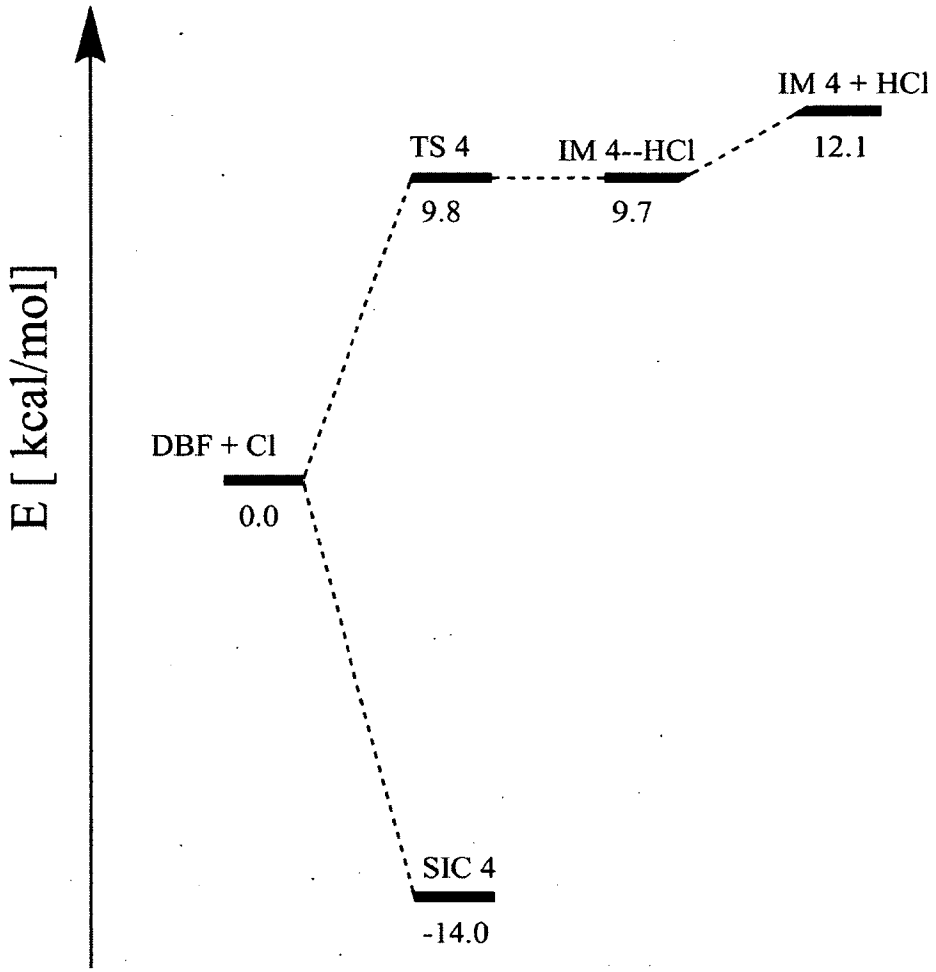

Figure 2-8. PES for Cl attack on DBF at carbon 4

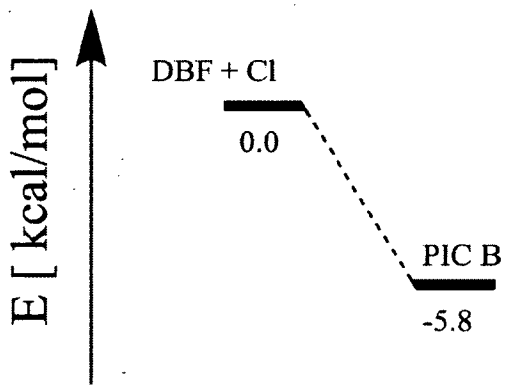

Figure 2-9. PES for Cl attack on DBF at carbon B

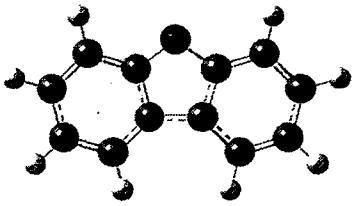

DBF

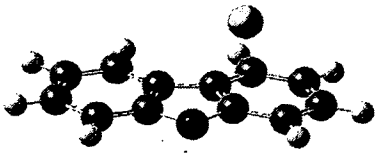

PIC A

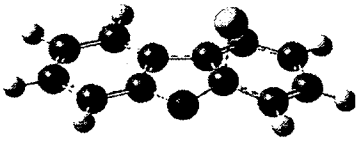

TS A

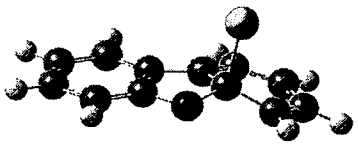

SIC A

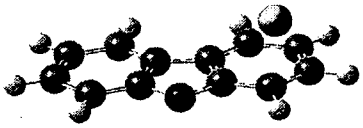

PIC 1

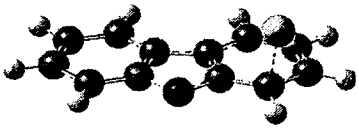

TS 1-1

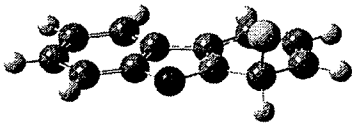

SIC 1

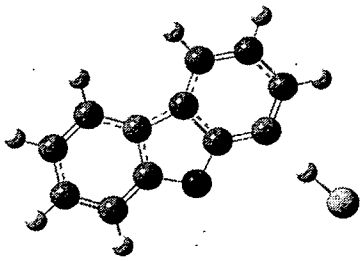

TS 1-2

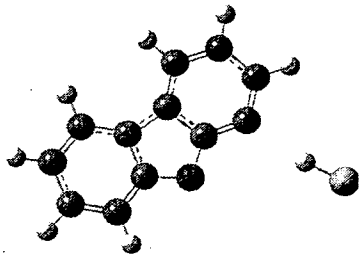

IM 1--HCl

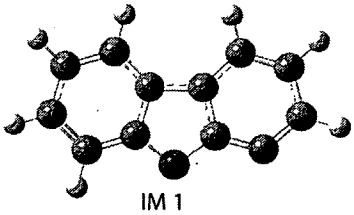

IM 1

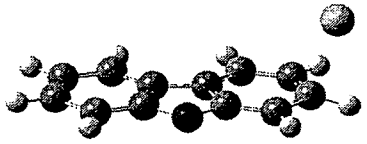

PIC 2

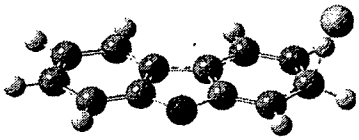

TS 2-1

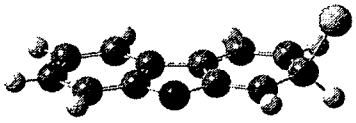

SIC 2

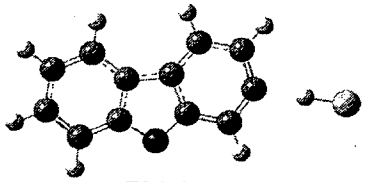

TS 2-2

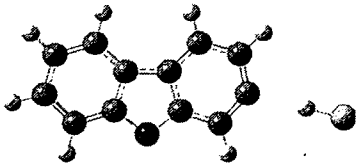

IM2--HCl

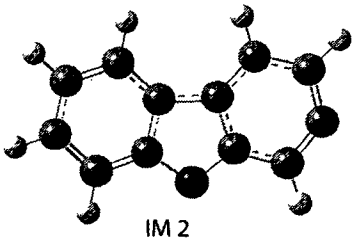

IM 2

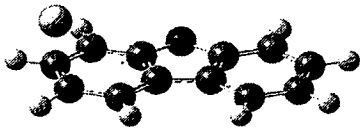

PIC 3

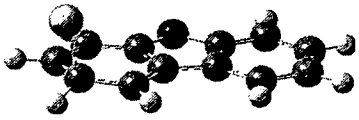

TS 3-1

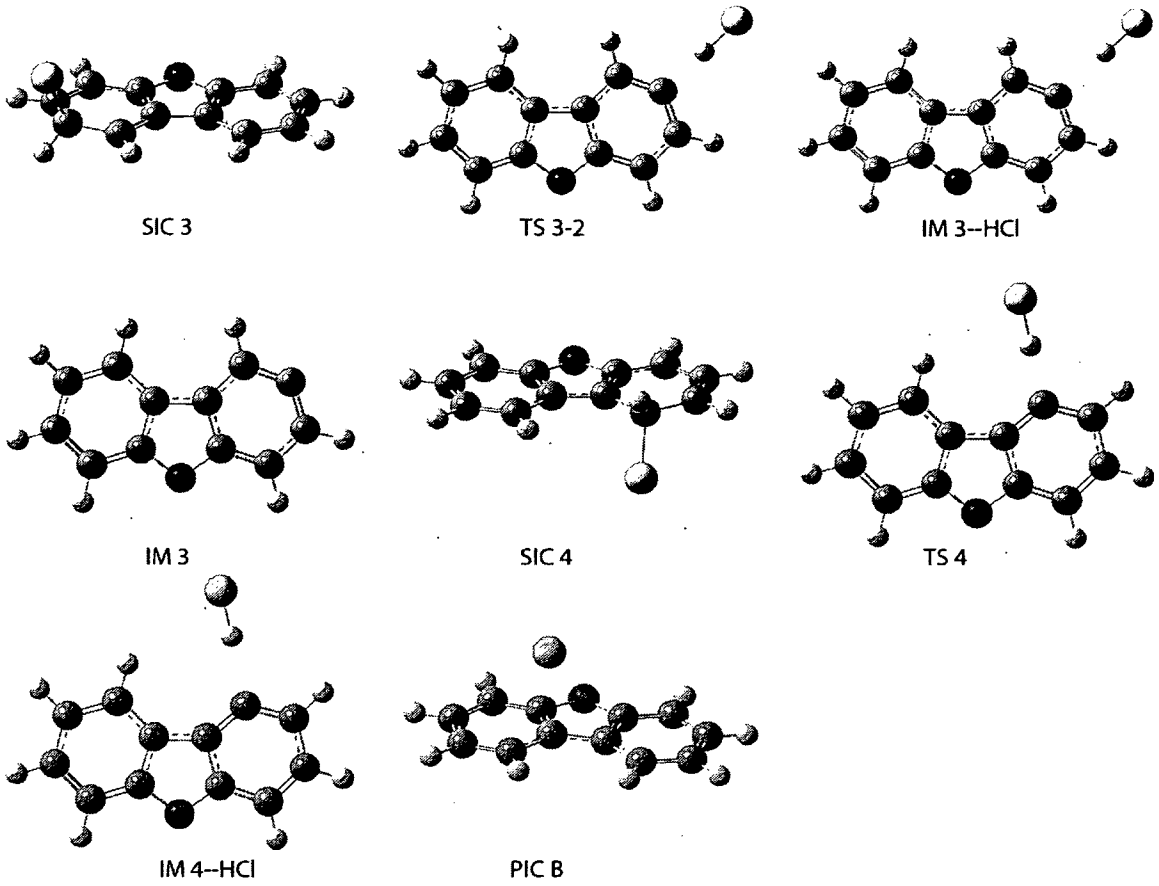

Figure 2-10. Geometries of the stationary points on the PES of Cl attack on DBF

LIST OF REFERENCES

1. Atkinson, R., Atmospheric chemistry of VOCs and NO_x. *Atmos. Environ.* **2000,** *34* (12–14), 2063-2101.

2. Atkinson, R.; Arey, J., Atmospheric degradation of volatile organic compounds. *Chem. Rev.* **2003,** *103* (12), 4605-38.

3. Brasseur, G. P.; Orlando, J. J.; Tyndall, G. S., *Atmospheric Chemistry and Global Change*. 1st ed.; Oxford University Press: New York, 1999.

4. Finlayson-Pitts, B. J.; Pitts, J. N., *Chemistry of the Upper and Lower Atmosphere: Theory, Experiments, and Applications*. 1st ed.; Academic Press: 1999.

5. Wayne, R. P., *Chemistry of Atmospheres: An Introduction to the Chemistry of the Atmospheres of Earth, the Planets, and their Satellites*. 3rd ed.; Oxford University Press, USA: 2000.

6. Seinfeld, J. H.; Pandis, S. N., *Atmospheric Chemistry and Physics: from Air Pollution to Climate Change*. Wiley: 2006.

7. Kroll, J. H.; Seinfeld, J. H., Chemistry of secondary organic aerosol: Formation and evolution of low-volatility organics in the atmosphere. *Atmos. Environ.* **2008,** *42* (16), 3593-3624.

8. Pope, C. A., Epidemiology of fine particulate air pollution and human health: biologic mechanisms and who's at risk? *Environ. Health Perspect.* **2000,** *108* (Suppl 4), 713-723.

9. Anenberg, S. C.; Horowitz, L. W.; Tong, D. Q.; West, J. J., An estimate of the global burden of anthropogenic ozone and fine particulate matter on premature human mortality using atmospheric modeling. *Environ. Health Perspect.* **2010,** *118* (9), 1189-1195.

10. Kanakidou, M.; Seinfeld, J. H.; Pandis, S. N.; Barnes, I.; Dentener, F. J.; Facchini, M. C.; Van Dingenen, R.; Ervens, B.; Nenes, A.; Nielsen, C. J.; Swietlicki, E.; Putaud, J. P.; Balkanski, Y.; Fuzzi, S.; Horth, J.; Moortgat, G. K.; Winterhalter, R.; Myhre, C. E. L.; Tsigaridis, K.; Vignati, E.; Stephanou, E. G.; Wilson, J., Organic aerosol and global climate modelling: a review. *Atmos. Chem. Phys.* **2005,** *5* (4), 1053-1123.

11. Shindell, D.; Faluvegi, G.; Lacis, A.; Hansen, J.; Ruedy, R.; Aguilar, E., Role of tropospheric ozone increases in 20th-century climate change. *J. Geophys. Res.* **2006,** *111* (D8), D08302.

12. Ainsworth, E. A.; Yendrek, C. R.; Sitch, S.; Collins, W. J.; Emberson, L. D., The Effects of Tropospheric Ozone on Net Primary Productivity and Implications for Climate Change. *Annu. Rev. Plant Biol.* **2012,** *63* (1), 637-661.

13. Bunnelle, W. H., Preparation, properties, and reactions of carbonyl oxides. *Chem. Rev.* **1991,** *91* (3), 335-362.

14. Hatakeyama, S.; Akimoto, H., Reactions of Criegee intermediates in the gas phase. *Res. Chem. Intermed.* **1994,** *20* (3), 503-524.

15. Calvert, J. G.; Atkinson, R.; Kerr, J. A.; S., M.; Moortgat, G. K.; Wallington, T. J.; Yarwood, G., *The Mechanisms of Atmospheric Oxidation of the Alkenes*. Oxford University Press: New York, 2000.

16. Johnson, D.; Marston, G., The gas-phase ozonolysis of unsaturated volatile organic compounds in the troposphere. *Chem. Soc. Rev.* **2008,** *37* (4), 699-716.

17. Donahue, N. M.; Drozd, G. T.; Epstein, S. A.; Presto, A. A.; Kroll, J. H., Adventures in ozoneland: down the rabbit-hole. *Phys. Chem. Chem. Phys.* **2011,** *13* (23), 10848-10857.

18. Vereecken, L.; Francisco, J. S., Theoretical studies of atmospheric reaction mechanisms in the troposphere. *Chem. Soc. Rev.* **2012,** *41* (19), 6259-6293.

19. Alam, M. S.; Camredon, M.; Rickard, A. R.; Carr, T.; Wyche, K. P.; Hornsby, K. E.; Monks, P. S.; Bloss, W. J., Total radical yields from tropospheric ethene ozonolysis. *Phys. Chem. Chem. Phys.* **2011,** *13* (23), 11002-11015.

20. Berndt, T.; Jokinen, T.; Mauldin, R. L.; Petäjä, T.; Herrmann, H.; Junninen, H.; Paasonen, P.; Worsnop, D. R.; Sipilä, M., Gas-Phase Ozonolysis of Selected Olefins: The Yield of Stabilized Criegee Intermediate and the Reactivity toward SO_2. *J. Phys. Chem. Lett.* **2012,** *3* (19), 2892-2896.

21. Pinelo, L.; Ault, B. S., Infrared matrix isolation and theoretical study of the initial intermediates in the reaction of ozone with cycloheptene. *J. Mol. Struct.* **2012,** *1026*, 23-29.

22. Vereecken, L.; Harder, H.; Novelli, A., The reaction of Criegee intermediates with NO, RO_2, and SO_2, and their fate in the atmosphere. *Phys. Chem. Chem. Phys.* **2012,** *14* (42), 14682-14695.

23. Bloss, W. J.; Alam, M. S.; Rickard, A. R.; Camredon, M.; Wyche, K. P.; Carr, T.; Monks, P. S., Production of the Atmospheric Oxidant Radicals OH and HO_2 from the Ozonolysis of Alkenes. In *Disposal of Dangerous Chemicals in Urban Areas and Mega Cities*, Barnes, I.; Rudziński, K. J., Eds. Springer Netherlands: 2013; pp 151-162.

24. Beames, J. M.; Liu, F.; Lu, L.; Lester, M. I., Ultraviolet Spectrum and Photochemistry of the Simplest Criegee Intermediate CH_2OO. *J. Am. Chem. Soc.* **2012,** *134* (49), 20045-20048.

25. Hu, J.; Stedman, D. H., Atmospheric RO_x Radicals at an Urban Site: Comparison to a Simple Theoretical Model. *Environ. Sci. Technol.* **1995,** *29* (6), 1655-1659.

26. Paulson, S. E.; Orlando, J. J., The reactions of ozone with alkenes: An important source of HO_x in the boundary layer. *Geophys. Res. Lett.* **1996,** *23* (25), 3727-3730.

27. Heard, D. E.; Carpenter, L. J.; Creasey, D. J.; Hopkins, J. R.; Lee, J. D.; Lewis, A. C.; Pilling, M. J.; Seakins, P. W.; Carslaw, N.; Emmerson, K. M., High levels of the hydroxyl radical in the winter urban troposphere. *Geophys. Res. Lett.* **2004,** *31* (18), L18112.

28. Elshorbany, Y. F.; Kurtenbach, R.; Wiesen, P.; Lissi, E.; Rubio, M.; Villena, G.; Gramsch, E.; Rickard, A. R.; Pilling, M. J.; Kleffmann, J., Oxidation capacity of the city air of Santiago, Chile. *Atmos. Chem. Phys.* **2009,** *9* (6), 2257-2273.

29. Volkamer, R.; Sheehy, P.; Molina, L. T.; Molina, M. J., Oxidative capacity of the Mexico City atmosphere – Part 1: A radical source perspective. *Atmos. Chem. Phys.* **2010,** *10* (14), 6969-6991.

30. Zador, J.; Taatjes, C. A.; Fernandes, R. X., Kinetics of elementary reactions in low-temperature autoignition chemistry. *Progr. Energy Combust. Sci.* **2011,** *37*, 371-421.

31. Criegee, R., Mechanism of Ozonolysis. *Angew. Chem. Int. Ed. Engl.* **1975,** *14* (11), 745-752.

32. Niki, H.; Maker, P. D.; Savage, C. M.; Breitenbach, L. P., Fourier transform IR spectroscopic observation of propylene ozonide in the gas phase reaction of ozone—cis-2-butene—formaldehyde. *Chem. Phys. Lett.* **1977,** *46* (2), 327-330.

33. Taatjes, C. A.; Meloni, G.; Selby, T. M.; Trevitt, A. J.; Osborn, D. L.; Percival, C. J.; Shallcross, D. E., Direct Observation of the Gas-Phase Criegee Intermediate (CH_2OO). *J. Am. Chem. Soc.* **2008,** *130* (36), 11883-11885.

34. Welz, O.; Savee, J. D.; Osborn, D. L.; Vasu, S. S.; Percival, C. J.; Shallcross, D. E.; Taatjes, C. A., Direct Kinetic Measurements of Criegee Intermediate (CH_2OO) Formed by Reaction of CH_2I with O_2. *Science* **2012,** *335* (6065), 204-207.

35. Taatjes, C. A.; Welz, O.; Eskola, A. J.; Savee, J. D.; Osborn, D. L.; Lee, E. P. F.; Dyke, J. M.; Mok, D. W. K.; Shallcross, D. E.; Percival, C. J., Direct measurement of Criegee intermediate (CH_2OO) reactions with acetone, acetaldehyde, and hexafluoroacetone. *Phys. Chem. Chem. Phys.* **2012,** *14* (30), 10391-10400.

36. Mauldin, R. L.; Berndt, T.; Sipilae, M.; Paasonen, P.; Petaja, T.; Kim, S.; Kurten, T.; Stratmann, F.; Kerminen, V. M.; Kulmala, M., A new atmospherically relevant oxidant of sulphur dioxide. *Nature* **2012,** *488* (7410), 193-196.

37. Boy, M.; Mogensen, D.; Smolander, S.; Zhou, L.; Nieminen, T.; Paasonen, P.; Plass-Dülmer, C.; Sipilä, M.; Petäjä, T.; Mauldin, L.; Berresheim, H.; Kulmala, M., Oxidation of SO_2 by stabilized Criegee Intermediate (sCI) radicals as a crucial source for atmospheric sulphuric acid concentrations. *Atmos. Chem. Phys. Discuss.* **2012,** *12* (10), 27693-27736.

38. Wallington, T. J.; Dagaut, P.; Kurylo, M. J., UV absorption cross sections and reaction kinetics and mechanisms for peroxy radicals in the gas phase. *Chem. Rev.* **1992,** *92* (4), 667-710.

39. Wallington, T. J.; Nielsen, O. J., Peroxy Radicals and the Atmosphere. In *Peroxyl Radicals*, Alfassi, Z. B., Ed. Wiley: 1997; pp 113-172.

40. Wallington, T. J.; Nielsen, O. J.; Sehested, J., Reactions of organic peroxy radicals in the gas phase. In *Peroxyl Radicals*, Alfassi, Z. B., Ed. Chichester: 1997; pp 113-172.

41. Tyndall, G. S.; Cox, R. A.; Granier, C.; Lesclaux, R.; Moortgat, G. K.; Pilling, M. J.; Ravishankara, A. R.; Wallington, T. J., Atmospheric chemistry of small organic peroxy radicals. *J. Geophys. Res.* **2001,** *106* (D11), 12157-12182.

42. Orlando, J. J.; Tyndall, G. S., Laboratory studies of organic peroxy radical chemistry: an overview with emphasis on recent issues of atmospheric significance. *Chem. Soc. Rev.* **2012,** *41* (19), 6294-6317.

43. Lightfoot, P. D.; Cox, R. A.; Crowley, J. N.; Destriau, M.; Hayman, G. D.; Jenkin, M. E.; Moortgat, G. K.; Zabel, F., Organic peroxy radicals: Kinetics, spectroscopy and tropospheric chemistry. *Atmos. Environ. Part A. General Topics* **1992,** *26* (10), 1805-1961.

44. Archibald, A. T.; Petit, A. S.; Percival, C. J.; Harvey, J. N.; Shallcross, D. E., On the importance of the reaction between OH and RO_2 radicals. *Atmos. Sci. Lett.* **2009,** *10* (2), 102-108.

45. Ravishankara, A. R., Are chlorine atoms significant tropospheric free radicals? *PNAS* **2009,** *106* (33), 13639-13640.

46. Atkinson, R.; Baulch, D. L.; Cox, R. A.; Hampson, R. F.; Kerr, J. A.; Rossi, M. J.; Troe, J., Evaluated Kinetic and Photochemical Data for Atmospheric Chemistry: Supplement VI. IUPAC Subcommittee on Gas Kinetic Data Evaluation for Atmospheric Chemistry. *J. Phys. Chem. Ref. Data* **1997,** *26* (6), 1329-1499.

47. Sander, S. P.; Abbatt, J.; Barker, J. R.; Burkholder, J. B.; Friedl, R. R.; Golden, D. M.; Huie, R. E. K.; Kurylo, C. E.; Moortgat, M. J.; K., G.; Orkin, V. L.; Wine, P. H. *Chemical Kinetics and Photochemical Data for Use in Atmospheric Studies, Evaluation No. 17*; JPL Publication 10-6: 2011.

48. Rossi, M. J., Heterogeneous Reactions on Salts. *Chem. Rev.* **2003,** *103* (12), 4823-4882.

49. Finlayson-Pitts, B. J., The Tropospheric Chemistry of Sea Salt: A Molecular-Level View of the Chemistry of NaCl and NaBr. *Chem. Rev.* **2003,** *103* (12), 4801-4822.

50. Finlayson-Pitts, B. J., Chlorine Atoms as a Potential Tropospheric Oxidant in the Marine Boundary Layer. *Res. Chem. Intermed.* **1993,** *19* (3), 235-249.

51. Spicer, C. W.; Chapman, E. G.; Finlayson-Pitts, B. J.; Plastridge, R. A.; Hubbe, J. M.; Fast, J. D.; Berkowitz, C. M., Unexpectedly high concentrations of molecular chlorine in coastal air. *Nature* **1998,** *394* (6691), 353-356.

52. Riedel, T. P.; Bertram, T. H.; Crisp, T. A.; Williams, E. J.; Lerner, B. M.; Vlasenko, A.; Li, S.-M.; Gilman, J.; de Gouw, J.; Bon, D. M.; Wagner, N. L.; Brown, S. S.; Thornton, J. A., Nitryl Chloride and Molecular Chlorine in the Coastal Marine Boundary Layer. *Environ. Sci. Technol.* **2012,** *46* (19), 10463-10470.

53. Thornton, J. A.; Kercher, J. P.; Riedel, T. P.; Wagner, N. L.; Cozic, J.; Holloway, J. S.; Dubé, W. P.; Wolfe, G. M.; Quinn, P. K.; Middlebrook, A. M.; Alexander, B.; Brown, S. S., A large atomic chlorine source inferred from mid-continental reactive nitrogen chemistry. *Nature* **2010,** *464* (7286), 271-274.

54. Jungkamp, T.; Kukui, A.; Schindler, R., Determination of Rate Constants and Product Branching Ratios for the Reactions of CH_3O_2 and CH_3O with Cl Atoms at Room-Temperature. *Ber. Bunsen. Phys. Chem.* **1995,** *99* (8), 1057-1066.

55. Maricq, M. M.; Szente, J. J.; Kaiser, E. W.; Shi, J., Reaction of Chlorine Atoms with Methylperoxy and Ethylperoxy Radicals. *J. Phys. Chem.* **1994,** *98* (8), 2083-2089.

56. Daele, V.; Poulet, G., Kinetics and products of the reactions of CH_3O_2 with Cl and ClO. *J. Chim. Phys.* **1996**, 1081-1099.

57. Drougas, E.; Kosmas, A. M., Quantum mechanical studies on the potential energy surface of the reactions CH_3+OClO, CH_3O+ClO and CH_3O_2+Cl. *Chem. Phys. Lett.* **2003,** *369* (3–4), 269-274.

58. Schnell, M.; Muhlhauser, M.; Peyerimhoff, S. D., Can the methoxyradical CH_3O act as sink for Cl and ClO in the atmosphere? *J. Phys. Chem. A* **2004,** *108* (7), 1298-1304.

59. Mayne, H. R.; Johnson, R. P.; Sive, B. C., Density Functional Quantum Mechanical Studies on the Potential Energy Surface for the Cl + CH_3O_2 Reaction: Implications for the Reaction Mechanism. University of New Hampshire. Unpublished.

60. Glassman, I.; Yetter, R. A., *Combustion*. 4th ed.; Academic Press: Amsterdam; Boston, 2008.

61. Šslemr, F.; Warneck, P., Kinetics of the reaction of atomic hydrogen with methyl hydroperoxide. *Int. J. Chem. Kinet.* **1977,** *9* (2), 267-282.

62. Bogdanchikov, G. A.; Baklanov, A. V.; Parker, D. H., The substitution reactions RH + O_2 → RO_2 + H: transition state theory calculations based on the ab initio and DFT potential energy surface. *Chem. Phys. Lett.* **2004,** *385* (5–6), 486-490.

63. Vaughan, S.; Canosa-Mas, C. E.; Pfrang, C.; Shallcross, D. E.; Watson, L.; Wayne, R. P., Kinetic studies of reactions of the nitrate radical (NO_3) with peroxy radicals (RO_2): an indirect source of OH at night? *Phys. Chem. Chem. Phys.* **2006,** *8* (32), 3749-3760.

64. Francisco, J. S.; Crowley, J. N., Theoretical Investigation of Product Channels in the CH_3O_2 + Br Reaction. *J. Phys. Chem. A* **2006,** *110* (10), 3778-3784.

65. Kondo, O.; Benson, S. W., Kinetics and equilibria in the system Br + CH_3OOH → HBr + CH3OO. An upper limit for the heat of formation of the methylperoxy radical. *J. Phys. Chem.* **1984,** *er* (26), 6675-6680.

66. Aranda, A.; Laverdet, G.; Le Bras, G.; Poulet, G., Kinetic study of the CH_3O_2+Br reaction at 298 K. *J. Chim. Phys. Phys.-Chim. Biol.* **1998,** *95* (5), 963-972.

67. Papayannis, D. K.; Melissas, V. S.; Kosmas, A. M., Quantum mechanical studies of methyl bromoperoxide isomers and the CH_3O+BrO reaction. *Phys. Chem. Chem. Phys.* **2003,** *5* (14), 2976-2980.

68. Kwok, E. S. C.; Atkinson, R., Estimation of hydroxyl radical reaction rate constants for gas-phase organic compounds using a structure-reactivity relationship: An update. *Atmos. Environ.* **1995,** *29* (14), 1685-1695.

69. Gross, A.; JØrgensen, S., Theoretical Determinations Of Reaction Parameters For Atmospheric Chemical Reactions. In *Simulation and Assessment of Chemical Processes in a Multiphase Environment*, Barnes, I.; Kharytonov, M. M., Eds. Springer Netherlands: 2008; pp 31-45.

70. Fernandez-Ramos, A.; Ellingson, B. A.; Garrett, B. C.; Truhlar, D. G., Variational Transition State Theory with Multidimensional Tunneling. In *Rev. Comput. Chem.*, Lipkowitz, K. B.; Cundari, T. R., Eds. John Wiley & Sons, Inc.: 2007; Vol. 23, pp 125-232.

71. Fernandez-Ramos, A.; Miller, J. A.; Klippenstein, S. J.; Truhlar, D. G., Modeling the kinetics of bimolecular reactions. *Chem. Rev.* **2006,** *106* (11), 4518-4584.

72. Pu, J.; Truhlar, D. G., Validation of variational transition state theory with multidimensional tunneling contributions against accurate quantum mechanical dynamics for $H+CH_4 \rightarrow H_2+CH_3$ in an extended temperature interval. *J. Chem. Phys.* **2002,** *117* (4), 1479-1481.

73. Cramer, C., *Essentials of Computational Chemistry*. John Wiley & Sons: Chichester, 2004.

74. Corchado, J. C. C., Y.-Y.; Fast, P. L.; Hu, W-P.; Liu, Y.-P.; Lynch, G. C.; Nguyen, K. A.; Jackels, C. F.; Fernandez- Ramos, A.; Ellingson, B. A.; Lynch, B. J.; Zheng, J.; Melissas, V. S.; Villà, J.; Rossi, I.; Coitino, E. L.; Pu, J.; Albu, T. V.; Steckler, R.; Garrett, B. C.; Isaacson, A. D.; Truhlar, D. G. POLYRATE 9.7; University of Minnesota: Minneapolis, 2007.

75. Zheng, J.; Zhang, S.; Lynch, B. J.; Corchado, J. C.; Chuang, Y.-Y.; Fast, P. L.; Hu, W.-P.; Liu, Y.-P.; Lynch, G. C.; Nguyen, K. A.; Jackels, C. F.; Fernandez Ramos, A.; Ellingson, B. A.; Melissas, V. S.; Villà, J.; Rossi, I.; Coitiño, E. L.; Pu, J.; Albu, T. V.; Steckler, R.; Garrett, B. C.; Isaacson, A. D.; Truhlar, D. G. *POLYRATE*, 2008; University of Minnesota: Minneapolis, 2008.

76. Zheng, J.; Zhang, S.; Lynch, B. J.; Corchado, J. C.; Chuang, Y.-Y.; Fast, P. L.; Hu, W.-P.; Liu, Y.-P.; Lynch, G. C.; Nguyen, K. A.; Jackels, C. F.; Fernandez Ramos, A.; Ellingson, B. A.; Melissas, V. S.; Villà, J.; Rossi, I.; Coitiño, E. L.; Pu, J.; Albu, T. V.; Steckler, R.; Garrett, B. C.; Isaacson, A. D.; Truhlar, D. G. *POLYRATE*, 2010-A; University of Minnesota: Minneapolis, 2010.

77. Corchado, J. C.; Y.-Y. Chuang; Fast, P. L.; Hu, W.-P.; Liu, Y.-P.; Lynch, G. C.; Nguyen, K. A.; Jackels, C. F.; Ramos, A. F.; Ellingson, B. A.; Lynch, B. J.; Zheng, J.; Melissas, V. S.; Villa, J.; Rossi, I.; Coitiño, E. L.; Pu, J.; Albu, T. V.; Steckler, R.; Garrett, B. C.; Isaacson, A. D.; Truhlar, D. G. *GAUSSRATE*, 9.7; University of Minnesota: Minneapolis, 2007.

78. Zheng, J.; Zhang, S.; Corchado, J. C.; Chuang, Y.-Y.; Coitiño, E. L.; Ellingson, B. A.; Truhlar, D. G. *GAUSSRATE*, 2009; University of Minnesota: Minneapolis, 2010.

79. Becke, A. D., Density functional thermochemistry. III. The role of exact exchange. *J. Chem. Phys.* **1993,** *98* (7), 5648-5652.

80. Stephens, P. J.; Devlin, F. J.; Chabalowski, C. F.; Frisch, M. J., Ab Initio Calculation of Vibrational Absorption and Circular Dichroism Spectra Using Density Functional Force Fields. *J. Phys. Chem.* **1994,** *98* (45), 11623-11627.

81. Sousa, S. F.; Fernandes, P. A.; Ramos, M. J., General Performance of Density Functionals. *J. Phys. Chem. A* **2007,** *111* (42), 10439-10452.

82. Boese, A. D.; Martin, J. M. L.; Handy, N. C., The role of the basis set: Assessing density functional theory. *J. Chem. Phys.* **2003,** *119* (6), 3005-3014.

83. Check, C. E.; Gilbert, T. M., Progressive systematic underestimation of reaction energies by the B3LYP model as the number of C-C bonds increases: why organic chemists should use multiple DFT models for calculations involving polycarbon hydrocarbons. *J. Org. Chem.* **2005,** *70* (24), 9828-9834.

84. Kruse, H.; Goerigk, L.; Grimme, S., Why the Standard B3LYP/6-31G* Model Chemistry Should Not Be Used in DFT Calculations of Molecular Thermochemistry: Understanding and Correcting the Problem. *J. Org. Chem.* **2012,** 10824−10834.

85. Wodrich, M. D.; Corminboeuf, C.; Schleyer, P. v. R., Systematic Errors in Computed Alkane Energies Using B3LYP and Other Popular DFT Functionals. *Org. Lett.* **2006,** *8* (17), 3631-3634.

86. Zhao, Y.; Truhlar, D. G., Design of Density Functionals That Are Broadly Accurate for Thermochemistry, Thermochemical Kinetics, and Nonbonded Interactions. *J. Phys. Chem. A* **2005,** *109* (25), 5656-5667.

87. Zhao, Y.; González-García, N.; Truhlar, D. G., Benchmark Database of Barrier Heights for Heavy Atom Transfer, Nucleophilic Substitution, Association, and Unimolecular Reactions and Its Use to Test Theoretical Methods. *J. Phys. Chem. A* **2005,** *109* (9), 2012-2018.

88. Zhao, Y.; Pu, J.; Lynch, B. J.; Truhlar, D. G., Tests of second-generation and third-generation density functionals for thermochemical kinetics. *Phys. Chem. Chem. Phys.* **2004,** *6* (4), 673-676.

89. Cohen, A. J.; Mori-Sánchez, P.; Yang, W., Challenges for Density Functional Theory. *Chem. Rev.* **2012,** *112* (1), 289-320.

90. Goerigk, L.; Grimme, S., A thorough benchmark of density functional methods for general main group thermochemistry, kinetics, and noncovalent interactions. *Phys. Chem. Chem. Phys.* **2011,** *13* (14), 6670-6688.

91. Gaussian 09, R. A., M. J. Frisch, G. W. Trucks, H. B. Schlegel, G. E. Scuseria, M. A. Robb, J. R. Cheeseman, G. Scalmani, V. Barone, B. Mennucci, G. A. Petersson, H. Nakatsuji, M. Caricato, X. Li, H. P. Hratchian, A. F. Izmaylov, J. Bloino, G. Zheng, J. L. Sonnenberg, M. Hada, M. Ehara, K. Toyota, R. Fukuda, J. Hasegawa, M. Ishida, T. Nakajima, Y. Honda, O. Kitao, H. Nakai, T. Vreven, J. A. Montgomery, Jr., J. E. Peralta, F. Ogliaro, M. Bearpark, J. J. Heyd, E. Brothers, K. N. Kudin, V. N. Staroverov, R. Kobayashi, J. Normand, K. Raghavachari, A. Rendell, J. C. Burant, S. S. Iyengar, J.

Tomasi, M. Cossi, N. Rega, J. M. Millam, M. Klene, J. E. Knox, J. B. Cross, V. Bakken, C. Adamo, J. Jaramillo, R. Gomperts, R. E. Stratmann, O. Yazyev, A. J. Austin, R. Cammi, C. Pomelli, J. W. Ochterski, R. L. Martin, K. Morokuma, V. G. Zakrzewski, G. A. Voth, P. Salvador, J. J. Dannenberg, S. Dapprich, A. D. Daniels, Ö. Farkas, J. B. Foresman, J. V. Ortiz, J. Cioslowski, and D. J. Fox, Gaussian, Inc., Wallingford CT, 2009.

92. Gaussian 03, R. C., M. J. Frisch, G. W. Trucks, H. B. Schlegel, G. E. Scuseria, M. A. Robb, J. R. Cheeseman, J. A. Montgomery, Jr., T. Vreven, K. N. Kudin, J. C. Burant, J. M. Millam, S. S. Iyengar, J. Tomasi, V. Barone, B. Mennucci, M. Cossi, G. Scalmani, N. Rega, G. A. Petersson, H. Nakatsuji, M. Hada, M. Ehara, K. Toyota, R. Fukuda, J. Hasegawa, M. Ishida, T. Nakajima, Y. Honda, O. Kitao, H. Nakai, M. Klene, X. Li, J. E. Knox, H. P. Hratchian, J. B. Cross, V. Bakken, C. Adamo, J. Jaramillo, R. Gomperts, R. E. Stratmann, O. Yazyev, A. J. Austin, R. Cammi, C. Pomelli, J. W. Ochterski, P. Y. Ayala, K. Morokuma, G. A. Voth, P. Salvador, J. J. Dannenberg, V. G. Zakrzewski, S. Dapprich, A. D. Daniels, M. C. Strain, O. Farkas, D. K. Malick, A. D. Rabuck, K. Raghavachari, J. B. Foresman, J. V. Ortiz, Q. Cui, A. G. Baboul, S. Clifford, J. Cioslowski, B. B. Stefanov, G. Liu, A. Liashenko, P. Piskorz, I. Komaromi, R. L. Martin, D. J. Fox, T. Keith, M. A. Al-Laham, C. Y. Peng, A. Nanayakkara, M. Challacombe, P. M. W. Gill, B. Johnson, W. Chen, M. W. Wong, C. Gonzalez, and J. A. Pople, Gaussian, Inc., Wallingford CT, 2004.

93. Simón, L.; Goodman, J. M., How reliable are DFT transition structures? Comparison of GGA, hybrid-meta-GGA and meta-GGA functionals. *Org. Biomol. Chem.* **2011,** *9* (3), 689-700.

94. Alecu, I. M.; Zheng, J.; Zhao, Y.; Truhlar, D. G., Computational Thermochemistry: Scale Factor Databases and Scale Factors for Vibrational Frequencies Obtained from Electronic Model Chemistries. *J. Chem. Theory Comput.* **2010,** *6* (9), 2872-2887.

95. Merrick, J. P.; Moran, D.; Radom, L., An Evaluation of Harmonic Vibrational Frequency Scale Factors. *J. Phys. Chem. A* **2007,** *111* (45), 11683-11700.

96. Gräfenstein, J.; Kraka, E.; Filatov, M.; Cremer, D., Can Unrestricted Density-Functional Theory Describe Open Shell Singlet Biradicals? *Int. J. Mol. Sci.* **2002,** *3* (4), 360-394.

97. Labanowski, J. Simplified introduction to ab initio basis sets. Terms and Notation. http://www.ccl.net/cca/documents/basis-sets/basis.html.

98. Basis sets - General introduction. http://www.chem.utas.edu.au/staff/yatesb/honours/modules/mod5/basis1.html.

99. Krishnan, R.; Binkley, J. S.; Seeger, R.; Pople, J. A., Self-consistent molecular orbital methods. XX. A basis set for correlated wave functions. *J. Chem. Phys.* **1980,** *72* (1), 650-654.

100. Lynch, B. J.; Zhao, Y.; Truhlar, D. G., Effectiveness of Diffuse Basis Functions for Calculating Relative Energies by Density Functional Theory. *J. Phys. Chem. A* **2003,** *107* (9), 1384-1388.

101. Papajak, E.; Leverentz, H. R.; Zheng, J.; Truhlar, D. G., Efficient Diffuse Basis Sets: cc-pVxZ+ and maug-cc-pVxZ. *J. Chem. Theory Comput.* **2009,** *5* (5), 1197-1202.

102. Dunning, T. H., Gaussian basis sets for use in correlated molecular calculations. I. The atoms boron through neon and hydrogen. *J. Chem. Phys.* **1989,** *90* (2), 1007-1023.

103. Zhao, Y.; Schultz, N. E.; Truhlar, D. G., Design of Density Functionals by Combining the Method of Constraint Satisfaction with Parametrization for Thermochemistry, Thermochemical Kinetics, and Noncovalent Interactions. *J. Chem. Theory Comput.* **2006,** *2* (2), 364-382.

104. Zhao, Y.; Truhlar, D. G., Density Functionals with Broad Applicability in Chemistry. *Acc. Chem. Res.* **2008,** *41* (2), 157-167.

105. Zhao, Y.; Truhlar, D. G., A new local density functional for main-group thermochemistry, transition metal bonding, thermochemical kinetics, and noncovalent interactions. *J. Chem. Phys.* **2006,** *125* (19), 194101-194101-18.

106. Chai, J.-D.; Head-Gordon, M., Long-range corrected hybrid density functionals with damped atom–atom dispersion corrections. *Phys. Chem. Chem. Phys.* **2008,** *10* (44), 6615-6620.

107. Lynch, B. J.; Fast, P. L.; Harris, M.; Truhlar, D. G., Adiabatic Connection for Kinetics. *J. Phys. Chem. A* **2000,** *104* (21), 4811-4815.

108. Boese, A. D.; Martin, J. M. L., Development of density functionals for thermochemical kinetics. *J. Chem. Phys.* **2004,** *121* (8), 3405-3416.

109. Zhao, Y.; Lynch, B. J.; Truhlar, D. G., Development and Assessment of a New Hybrid Density Functional Model for Thermochemical Kinetics. *J. Phys. Chem. A* **2004,** *108* (14), 2715-2719.

110. Zhukovskiy, M.; Mayne, H. R., Unpublished results. University of New Hampshire.

111. Xu, K.; Xu, Z. F.; Lin, M. C., Ab initio kinetic prediction of branching rate constants for reactions of H atoms with CH_3O and CH_2OH. *Mol. Phys.* **2007,** *105* (19-22), 2763-2776.

112. Li, Q. S.; Zhang, Y.; Zhang, S., Direct ab initio dynamics study on the rate constants and kinetics isotope effects of $CH_3O+H \rightarrow CH_2O+H_2$ reaction. *J. Chem. Phys.* **2004,** *121* (19), 9474-9480.

113. Raghavachari, K.; Trucks, G. W.; Pople, J. A.; Head-Gordon, M., A fifth-order perturbation comparison of electron correlation theories. *Chem. Phys. Lett.* **1989,** *157* (6), 479-483.

114. Chuang, Y.-Y.; Radhakrishnan, M. L.; Fast, P. L.; Cramer, C. J.; Truhlar, D. G., Direct Dynamics for Free Radical Kinetics in Solution: Solvent Effect on the Rate Constant for the Reaction of Methanol with Atomic Hydrogen. *J. Phys. Chem. A* **1999,** *103* (25), 4893-4909.

115. Meana-Pañeda, R.; Truhlar, D. G.; Fernández-Ramos, A., High-level direct-dynamics variational transition state theory calculations including multidimensional tunneling of the thermal rate constants, branching ratios, and kinetic isotope effects of the hydrogen abstraction reactions from methanol by atomic hydrogen. *J. Chem. Phys.* **2011,** *134* (9), 094302-094302-14.

116. Page, M.; McIver, J. W., On evaluating the reaction path Hamiltonian. *J. Chem. Phys.* **1988,** *88* (2), 922-935.

117. Eyring, H., The Activated Complex in Chemical Reactions. *J. Chem. Phys.* **1935,** *3* (2), 107-115.

118. Houston, P., *Chemical Kinetics and Reaction Dynamics*. McGraw-Hill: Dubuque, Iowa, 2001.

119. Ginovska, B. Computational study of chemical reactions. M.S. Thesis. Washington State University, 2007.

120. McQuarrie, D. A.; Simon, J. D., *Physical Chemistry: a Molecular Approach*. University Science Books: Sausalito, Calif., 1997.

121. Fernández-Ramos, A.; Ellingson, B. A.; Meana-Pañeda, R.; Marques, J. M. C.; Truhlar, D. G., Symmetry numbers and chemical reaction rates. *Theor. Chem. Account.* **2007,** *118*, 813–826.

122. Seal, P.; Oyedepo, G.; Truhlar, D. G., Kinetics of the Hydrogen Atom Abstraction Reactions from 1-Butanol by Hydroxyl Radical: Theory Matches Experiment and More. *J. Phys. Chem. A* **2013,** *117* (2), 275-282.

123. Zhang, F.; Dibble, T. S., Impact of tunneling on hydrogen-migration of the n-propylperoxy radical. *Phys. Chem. Chem. Phys.* **2011,** *13* (40).

124. Ellingson, B. A.; Lynch, V. A.; Mielke, S. L.; Truhlar, D. G., Statistical thermodynamics of bond torsional modes: Tests of separable, almost-separable, and improved Pitzer–Gwinn approximations. *J. Chem. Phys.* **2006,** *125* (8), 084305-084305-17.

125. Truhlar, D. G.; Isaacson, A. D.; Garrett, B. C., Generalized Transition State Theory. In *Theory of Chemical Reaction Dynamics*, Baer, M., Ed. CRC Press: Boca Raton, 1985; Vol. 4, pp 65-137.

126. Corchado, J. C.; Coitiño, E. L.; Chuang, Y.-Y.; Fast, P. L.; Truhlar, D. G., Interpolated Variational Transition-State Theory by Mapping. *J. Phys. Chem. A* **1998,** *102* (14), 2424-2438.

127. Jackels, C. F.; Gu, Z.; Truhlar, D. G., Reaction path potential and vibrational frequencies in terms of curvilinear internal coordinates. *J. Chem. Phys.* **1995,** *102* (8), 3188-3201.

128. Natanson, G. A.; Garrett, B. C.; Truong, T. N.; Joseph, T.; Truhlar, D. G., The definition of reaction coordinates for reaction path dynamics. *J. Chem. Phys.* **1991,** *94* (12), 7875-7892.

129. Nguyen, K. A.; Jackels, C. F.; Truhlar, D. G., Reaction path dynamics in curvilinear internal coordinates including torsions. *J. Chem. Phys.* **1996,** *104* (17), 6491-6496.

130. Espinosa-García, J.; Corchado, J. C., Recalibration of Two Earlier Potential Energy Surfaces for the $CH_4 + H \rightarrow CH_3 + H_2$ Reaction. Application of Variational Transition-State Theory and Analysis of the Kinetic Isotope Effects Using Rectilinear and Curvilinear Coordinates. *J. Phys. Chem.* **1996,** *100* (41), 16561-16567.

131. Chuang, Y.-Y.; Truhlar, D. G., Reaction-path dynamics with harmonic vibration frequencies in curvilinear internal coordinates: H+trans-$N_2H_2 \rightarrow N_2H+H_2$. *J. Chem. Phys.* **1997,** *107* (1), 83-89.

132. Corchado, J. C.; Espinosa-García, J., Analytical potential energy surface for the $NH_3+H \leftrightarrow NH_2+H_2$ reaction: Application of variational transition-state theory and analysis of the equilibrium constants and kinetic isotope effects using curvilinear and rectilinear coordinates. *J. Chem. Phys.* **1997,** *106* (10), 4013-4021.

133. Corchado, J. C.; Espinosa-García, J.; Roberto-Neto, O.; Chuang, Y.-Y.; Truhlar, D. G., Dual-Level Direct Dynamics Calculations of the Reaction Rates for a Jahn–Teller Reaction: Hydrogen Abstraction from CH_4 or CD_4 by $O(^3P)$. *J. Phys. Chem. A* **1998,** *102* (25), 4899-4910.

134. Espinosa-García, J.; García-Bernáldez, J. C., Analytical potential energy surface for the CH_4+ $O(^3P)$→CH_3+ OH reaction. Thermal rate constants and kinetic isotope effects. *Phys. Chem. Chem. Phys.* **2000,** *2* (10), 2345-2351.

135. Ellingson, B. A.; Pu, J.; Lin, H.; Zhao, Y.; Truhlar, D. G., Multicoefficient Gaussian-3 Calculation of the Rate Constant for the OH + CH_4 Reaction and Its 12C/13C Kinetic Isotope Effect with Emphasis on the Effects of Coordinate System and Torsional Treatment. *J. Phys. Chem. A* **2007,** *111* (45), 11706-11717.

136. Chuang, Y.-Y.; Truhlar, D. G., Reaction-Path Dynamics in Redundant Internal Coordinates. *J. Phys. Chem. A* **1998,** *102* (1), 242-247.

137. Griffiths, D. J., *Introduction to Quantum Mechanics*. Prentice Hall: Englewood Cliffs, NJ, 1995.

138. Garrett, B. C.; Truhlar, D. G., Generalized transition state theory calculations for the reactions D+H_2 and H+D_2 using an accurate potential energy surface: Explanation of the kinetic isotope effect. *J. Chem. Phys.* **1980,** *72* (6), 3460-3471.

139. Liu, Y. P.; Lu, D. H.; Gonzalez-Lafont, A.; Truhlar, D. G.; Garrett, B. C., Direct dynamics calculation of the kinetic isotope effect for an organic hydrogen-transfer reaction, including corner-cutting tunneling in 21 dimensions. *J. Am. Chem. Soc.* **1993,** *115* (17), 7806-7817.

140. Garrett, B. C.; Truhlar, D. G.; Grev, R. S.; Magnuson, A. W., Improved treatment of threshold contributions in variational transition-state theory. *J. Phys. Chem.* **1980,** *84* (13), 1730-1748.

141. Kuppermann, A.; Truhlar, D. G., Exact tunneling calculations. *J. Am. Chem. Soc.* **1971,** *93* (8), 1840-1851.

142. Liu, Y. P.; Lynch, G. C.; Truong, T. N.; Lu, D. H.; Truhlar, D. G.; Garrett, B. C., Molecular modeling of the kinetic isotope effect for the [1,5]-sigmatropic rearrangement of cis-1,3-pentadiene. *J. Am. Chem. Soc.* **1993,** *115* (6), 2408-2415.

143. Fernandez-Ramos, A.; Truhlar, D. G., Improved algorithm for corner-cutting tunneling calculations. *J. Chem. Phys.* **2001,** *114* (4), 1491-1496.

144. Truhlar, D. G.; Garrett, B. C., Variational Transition State Theory in the Treatment of Hydrogen Transfer Reactions. In *Hydrogen-Transfer Reactions*, Hynes, J. T.; Klinman, J. P.; Limbach, H.-H.; Schowen, R. L., Eds. Wiley-VCH Verlag GmbH & Co. KGaA: 2007; pp 833-874.

145. Truhlar, D. G., Variational Transition-State Theory and Multidimensional Tunneling for Simple and Complex Reactions in the Gas Phase, Solids, Liquids, and

Enzymes. In *Isotope Effects in Chemistry and Biology*, Kohen, A.; Limbach, H.-H., Eds. Marcel Dekker: New York, 2006; pp 579-620.

146. Zheng, J.; Truhlar, D. G., Kinetics of hydrogen-transfer isomerizations of butoxyl radicals. *Phys. Chem. Chem. Phys.* **2010,** *12* (28), 7782-7793.

147. Anslyn, E. V.; Dougherty, D. A., *Modern Physical Organic Chemistry*. University Science: Sausalito, CA, 2006.

148. Chakraborty, A.; Zhao, Y.; Lin, H.; Truhlar, D. G., Combined valence bond-molecular mechanics potential-energy surface and direct dynamics study of rate constants and kinetic isotope effects for the $H+C_2H_6$ reaction. *J. Chem. Phys.* **2006,** *124* (4), 044315-044315-14.

149. Georgievskii, Y.; Klippenstein, S. J., Variable reaction coordinate transition state theory: Analytic results and application to the $C_2H_3+H \rightarrow C_2H_4$ reaction. *J. Chem. Phys.* **2003,** *118* (12), 5442-5455.

150. Van den Berg, M.; De Jongh, J.; Poiger, H.; Olson, J. R., The toxicokinetics and metabolism of polychlorinated dibenzo-p-dioxins (PCDDs) and dibenzofurans (PCDFs) and their relevance for toxicity. *Crit. Rev. Toxicol.* **1994,** *24* (1), 1-74.

151. Van den Berg, M.; Birnbaum, L.; Bosveld, A. T.; Brunström, B.; Cook, P.; Feeley, M.; Giesy, J. P.; Hanberg, A.; Hasegawa, R.; Kennedy, S. W.; Kubiak, T.; Larsen, J. C.; van Leeuwen, F. X.; Liem, A. K.; Nolt, C.; Peterson, R. E.; Poellinger, L.; Safe, S.; Schrenk, D.; Tillitt, D.; Tysklind, M.; Younes, M.; Waern, F.; Zacharewski, T., Toxic equivalency factors (TEFs) for PCBs, PCDDs, PCDFs for humans and wildlife. *Environ. Health Perspect.* **1998,** *106* (12), 775-792.

152. Carrier, G.; Brunet, R. C.; Brodeur, J., Modeling of the toxicokinetics of polychlorinated dibenzo-p-dioxins and dibenzofurans in mammalians, including humans. II. Kinetics of absorption and disposition of PCDDs/PCDFs. *Toxicol. Appl. Pharmacol.* **1995,** *131* (2), 267-276.

153. *Air Quality Guidelines for Europe - Second Edition*; WHO: 2000.

154. Atkinson, R., Atmospheric Chemistry of PCBs, PCDDs and PCDFs. In *Chlorinated Organic Micropollutants*, Hester, R. E.; Harrison, R. M., Eds. Royal Society of Chemistry: Cambridge, U.K., 1996; pp 53-72.

155. Baker, J. I.; Hites, R. A., Is Combustion the Major Source of Polychlorinated Dibenzo-p-dioxins and Dibenzofurans to the Environment? A Mass Balance Investigation. *Environ. Sci. Technol.* **2000,** *34* (14), 2879-2886.

156. Li, H.; Yu, L.; Sheng, G.; Fu, J.; Peng, P., Severe PCDD/F and PBDD/F Pollution in Air around an Electronic Waste Dismantling Area in China. *Environ. Sci. Technol.* **2007,** *41* (16), 5641-5646.

157. Atkinson, R., Atmospheric lifetimes of dibenzo-p-dioxins and dibenzofurans. *Sci. Total Environ.* **1991,** *104* (1–2), 17-33.

158. Sinkkonen, S.; Paasivirta, J., Degradation half-life times of PCDDs, PCDFs and PCBs for environmental fate modeling. *Chemosphere* **2000,** *40* (9–11), 943-949.

159. Ogura, I.; Masunaga, S.; Nakanishi, J., Analysis of atmospheric behavior of PCDDs/PCDFs by a one-compartment box model. *Chemosphere* **2003,** *53* (4), 399-412.

160. Kwok, E. S. C.; Arey, J.; Atkinson, R., Gas-phase atmospheric chemistry of dibenzo-p-dioxin and dibenzofuran. *Environ. Sci. Technol.* **1994,** *28* (3), 528-533.

161. Kwok, E. S. C.; Atkinson, R.; Arey, J., Rate Constants for the Gas-Phase Reactions of the OH Radical with Dichlorobiphenyls, 1-Chlorodibenzo-p-dioxin, 1,2-Dimethoxybenzene, and Diphenyl Ether: Estimation of OH Radical Reaction Rate Constants for PCBs, PCDDs, and PCDFs. *Environ. Sci. Technol.* **1995,** *29* (6), 1591-1598.

162. Brubaker, W. W.; Hites, R. A., Polychlorinated Dibenzo-p-dioxins and Dibenzofurans: Gas-Phase Hydroxyl Radical Reactions and Related Atmospheric Removal. *Environ. Sci. Technol.* **1997,** *31* (6), 1805-1810.

163. Brubaker, W. W.; Hites, R. A., OH Reaction Kinetics of Polycyclic Aromatic Hydrocarbons and Polychlorinated Dibenzo-p-dioxins and Dibenzofurans. *J. Phys. Chem. A* **1998,** *102* (6), 915-921.

164. Taylor, P. H.; Yamada, T.; Neuforth, A., Kinetics of OH radical reactions with dibenzo-p-dioxin and selected chlorinated dibenzo-p-dioxins. *Chemosphere* **2005,** *58* (3), 243-252.

165. Sebbar, N. Thermochemistry and Kinetics for the Oxidative Degradation of Dibenzofuran and Precursors (available online). Ph.D. Thesis. Universitat Karlsruhe, 2006.

166. Altarawneh, M.; Dlugogorski, B. Z.; Kennedy, E. M.; Mackie, J. C., Quantum Chemical Study of Low Temperature Oxidation Mechanism of Dibenzofuran. *J. Phys. Chem. A* **2006,** *110* (50), 13560-13567.

167. Altarawneh, M.; Kennedy, E. M.; Dlugogorski, B. Z.; Mackie, J. C., Computational Study of the Oxidation and Decomposition of Dibenzofuran under Atmospheric Conditions. *J. Phys. Chem. A* **2008,** *112* (30), 6960-6967.

168. Sun, X.; Zhang, C.; Zhao, Y.; Bai, J.; Zhang, Q.; Wang, W., Atmospheric Chemical Reactions of 2,3,7,8-Tetrachlorinated Dibenzofuran Initiated by an OH Radical: Mechanism and Kinetics Study. *Environ. Sci. Technol.* **2012,** *46* (15), 8148-8155.

169. Zhang, C.; Zhao, Y.; Bai, J.; Gong, C.; Sun, X., Mechanism and kinetic study on the OH-initiated degradation of 2,3,7,8-tetrachlorinated dibenzofuran in atmosphere. *Sci. Total Environ.* **2012,** *435–436,* 53-60.

170. Cabañas, B.; Villanueva, F.; Martín, P.; Baeza, M. T.; Salgado, S.; Jiménez, E., Study of reaction processes of furan and some furan derivatives initiated by Cl atoms. *Atmos. Environ.* **2005,** *39* (10), 1935-1944.

171. Villanueva, F.; Barnes, I.; Monedero, E.; Salgado, S.; Gómez, M. V.; Martin, P., Primary product distribution from the Cl-atom initiated atmospheric degradation of furan: Environmental implications. *Atmos. Environ.* **2007,** *41* (38), 8796-8810.

172. Villanueva, F.; Cabañas, B.; Monedero, E.; Salgado, S.; Bejan, I.; Martin, P., Atmospheric degradation of alkylfurans with chlorine atoms: Product and mechanistic study. *Atmos. Environ.* **2009,** *43* (17), 2804-2813.

173. Zhang, W.; Du, B., Products and mechanism of the Cl-initiated atmospheric oxidation of furan: A theoretical study. *Comp. Theor. Chem.* **2011,** *963* (2-3), 348-356.

174. Russell, G. A.; Brown, H. C., The Liquid Phase Photochlorination and Sulfuryl Chloride Chlorination of Branchedchain Hydrocarbons; the Effect of Structure on the Relative Reactivities of Tertiary Hydrogen in Free Radical Chlorinations1,2. *J. Am. Chem. Soc.* **1955,** *77* (15), 4031-4035.

175. Tsao, M.-L.; Hadad, C. M.; Platz, M. S., Computational Study of the Halogen Atom−Benzene Complexes. *J. Am. Chem. Soc.* **2003,** *125* (27), 8390-8399.

176. Croft, A. K.; Howard-Jones, H. M., Chlorine--benzene complexes--the reliability of density functionals for non-covalent radical complexes. *Phys. Chem. Chem. Phys.* **2007,** *9* (42), 5649-5655.

177. Croft, A. K.; Howard-Jones, H. M.; Skates, C. E.; Wood, C. C., Controlling the action of chlorine radical: from lab to environment. *Org. Biomol. Chem.* **2011,** *9* (21), 7439-7447.